Bipolar Thermoelectric Devices

by

Kevin Patrick Pipe

B.S. Electrical Engineering and Computer Science
Massachusetts Institute of Technology (1999)
M.Eng. Electrical Engineering and Computer Science
Massachusetts Institute of Technology (1999)

Submitted to the Department of Electrical Engineering and Computer Science
in partial fulfillment of the requirements for the degree of

Doctor of Philosophy in Electrical Engineering

at the

MASSACHUSETTS INSTITUTE OF TECHNOLOGY

February 2004

Author . . . .
Department of Electrical Engineering and Computer Science
December 4, 2003

Certified by . . . .
Rajeev J. Ram
Associate Professor
Thesis Supervisor

Accepted by . . . .
Arthur C. Smith
Chairman, Department Committee on Graduate Students

Bipolar Thermoelectric Devices

by

Kevin Patrick Pipe

Submitted to the Department of Electrical Engineering and Computer Science
on December 4, 2003, in partial fulfillment of the
requirements for the degree of
Doctor of Philosophy in Electrical Engineering

Abstract

The work presented here is a theoretical and experimental study of heat production and transport in bipolar electrical devices, with detailed treatment of thermoelectric effects. Both homojunction and heterojunction devices are considered, and particular attention is given to semiconductor laser diodes. The mechanisms that govern both internal heat exchange and heat transfer between a device and its environment are examined, leading to structures which are optimized for thermal management.

Thesis Supervisor: Rajeev J. Ram
Title: Associate Professor

Acknowledgements

This work represents a cumulation of the time and effort of a number of people. Here I would like to highlight those whom I feel deserve special recognition.

Rajeev Ram has been incredibly supportive as this work evolved from a whiteboard sketch of a staircase laser with thermionic emission cooling and an acronym to the present form. His knowledge base, creativity, and positive attitude have made my stay in his group an enjoyable one and have made a lasting impact on my future endeavors. Likewise, Ali Shakouri has been a source of guidance and inspiration from the beginning, offering support and ideas that nicely complemented those of Rajeev. I count Rajeev and Ali among my very good friends and look forward to future collaboration.

I am indebted also to my collaborators at Lincoln Laboratory: George Turner, Hong Choi, Anish Goyal, Robin Huang, and Paul Juodawlkis. Their technical expertise and willingness to provide devices and material growths facilitated a large portion of this work. Likewise, I would like to thank Ho-Ki Lyeo and Li Shi at UT Austin, who were very helpful in providing experimental evidence in support of my research. Shaomin Wu and John Bowers at UC Santa Barbara were similarly helpful in providing material growths.

I would like to thank other members of my thesis committee, Gang Chen and Dimitri Antoniadis, for their technical guidance and time, and Terry Orlando for his assistance as my academic advisor. Lincoln Laboratory and the National Science Foundation (and U.S. taxpayers) also deserve acknowledgement for funding my research.

As I believe this thesis reflects the final stimulated emission of the MIT Semiconductor Laser Group during its transition to the Physical Optics and Electronics Group, I feel it is important to acknowledge both past and present members of this illustrious team. I would like to thank Steve Patterson, who sets an example of integrity; Farhan Rana, who sets an example of discipline; Fatih Yanik for his attitude; Margaret Wang for her warmth; Erwin Lau for his honesty; Brian Goldberg for his

Contents

List of Figures

7

9

List of Tables

Chapter 1

BACKGROUND

Active devices such as transistors, light-emitting diodes, amplifiers, switches, and transmitters represent a fundamental class of electrical components due to their ability to perform transformations on an input signal. These operations rely on the transport of internal systems of charge carriers that, due to the bipolar nature of most such devices, usually consist of both electrons and holes. Since these charge carrier energy transitions are coupled to lattice vibrational modes, device performance is often closely tied to device heating. For semiconductor laser diodes in particular, such critical parameters as wavelength, threshold current, quantum efficiency, and device lifetime are all strongly dependent on temperature [7, 8, 9]. The subject of heat generation and transport is thus significant in the design of active devices; a thorough understanding of device heating requires the examination both of internal heat exchange and of external heat flow between a device and its environment.

1.1 Thermal Management of Devices

Tremendous progress in the areas of electronic and optoelectronic devices during the last several decades has yielded devices which are increasingly faster, smaller, and more sophisticated. Components for communication systems and microprocessors are now fabricated in dense arrays with submicron technology. While this has been advantageous from a performance perspective, devices must deposit waste heat into
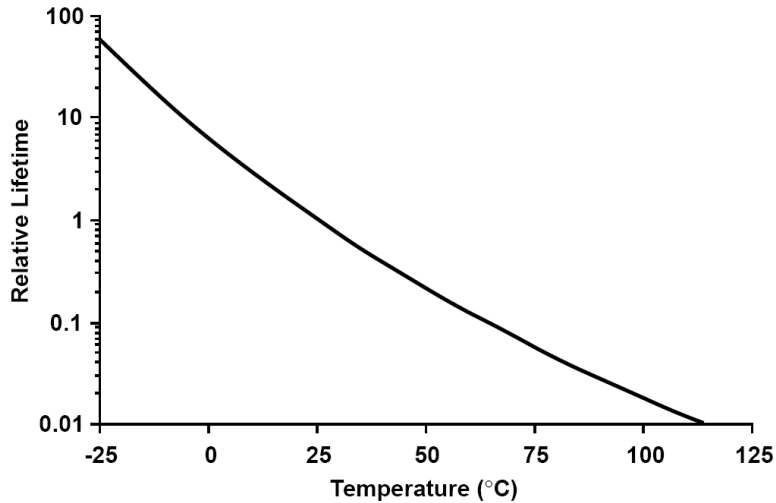
Figure 1-1: Relative microprocessor lifetime at different operating temperatures [1].

an ever-smaller surrounding space, making thermal management an increasingly high priority in device design. The occurrence of thermal rollover in the performance of most devices is indicative of this problem, as is the decrease of device lifetime with increased operating temperature (see Figure 1-1).

Current-generation Intel microprocessors generate heat at a rate of approximately 50 W/cm^2 (see Figure 1-2), and heating is expected to rise to 125 W/cm^2 by 2005 [10, 11]. In contrast, conventional methods for thermal management such as traditional thermoelectric coolers are only able to remove heat at approximately 10 W/cm^2 [12]. In order to close this gap, novel cooling systems such as advanced heat spreading (see Figure 1-3), vapor compression refrigeration, and liquid/air hybrid schemes have been developed that are able to sustain heat loads well above 100 W/cm^2. The implementation of these systems, however, has often been hampered by inherent complexity, high cost, and diminished reliability [13]. Perhaps of greater importance is the inability of these solutions to manage micron-scale "hot spots" that occur with increasing regularity in modern devices. Common power electronics and optoelectronics, for example, can already generate heat spots with fluxes of 300-1000 W/cm^2 or greater [14].

Attempts to manage heat sources at this size scale have, until recently, met with limited success due to a lack of processing technology for integration with devices.

17
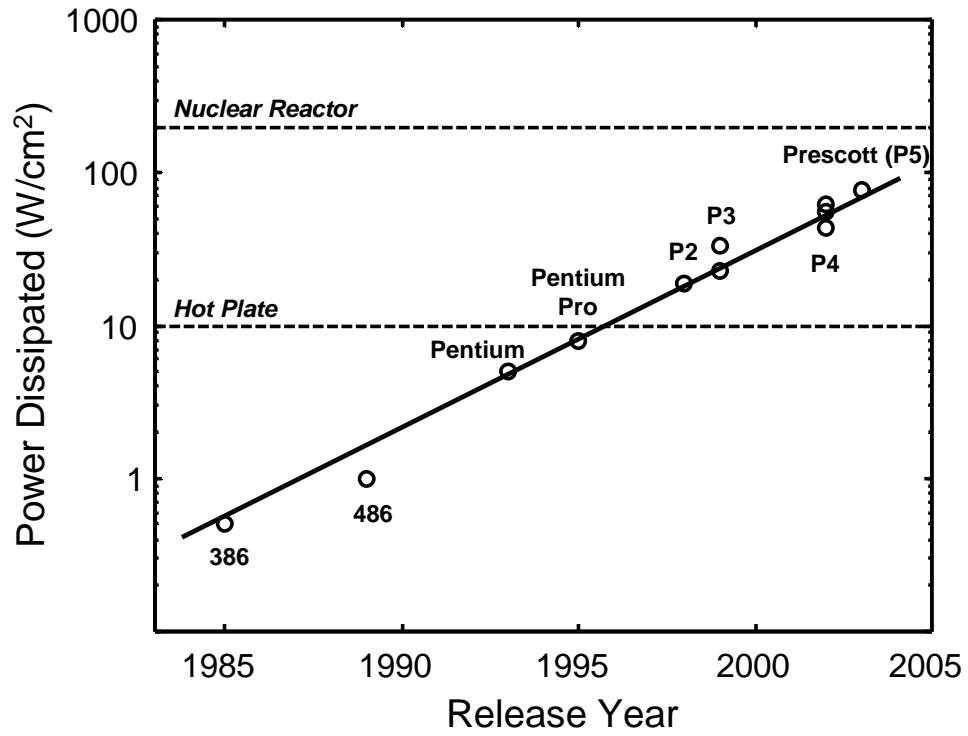
Figure 1-2: Intel microprocessor heat dissipation.
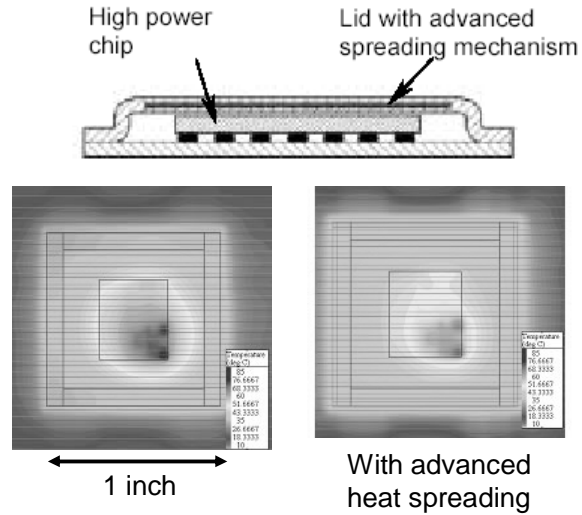
Figure 1-3: Thermacore miniature pulsating heat pipe for advanced heat spreading [2].
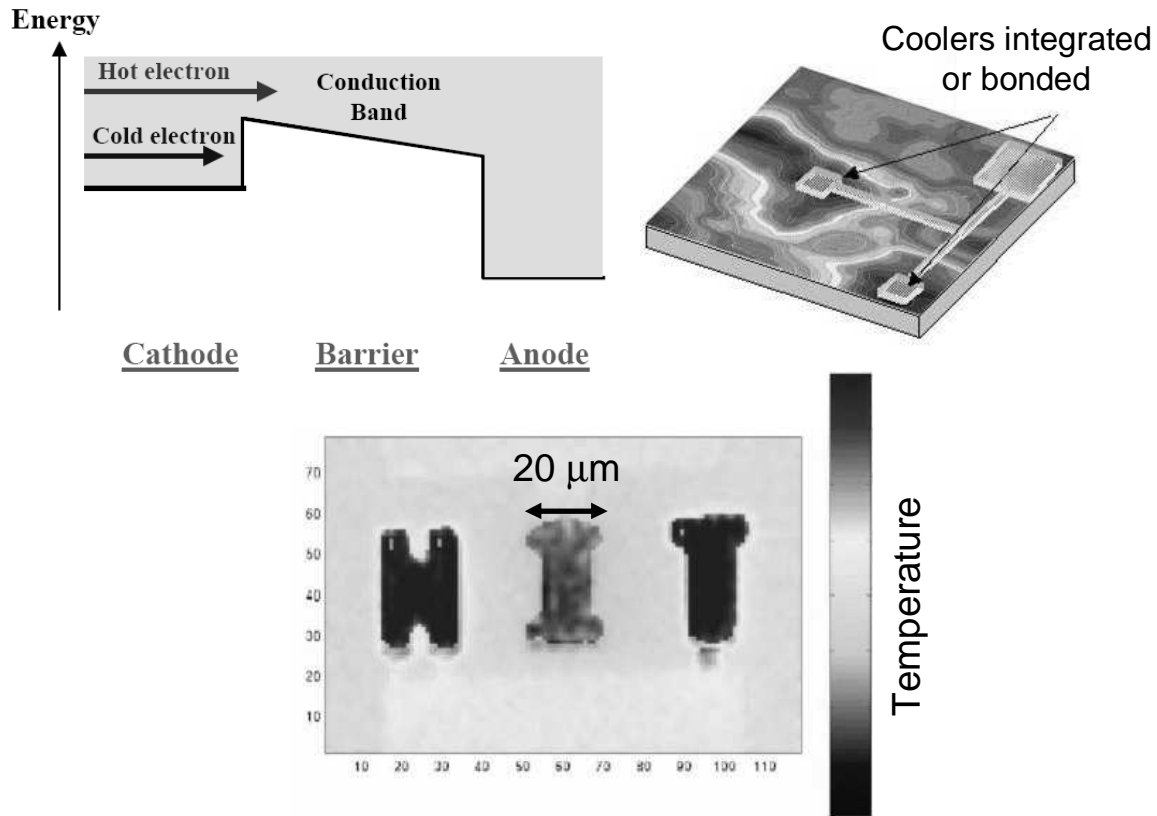
Figure 1-4: Heterostructure Integrated Thermionic cooler (based on thermoelectric and thermionic effects) [3].

Over the last decade, however, progress in the areas of microfluidics, crystal growth, and lithography has led to new cooling solutions based on microchannel technology [15] and solid-state electronics. Current research in solid-state micro-coolers is especially attractive due to their lack of moving parts and ability to scale with device size. For these reasons, attention has returned to the field of thermoelectrics, and advanced devices have been created that offer unprecedented cooling power densities [16]. Many of these devices rely on both thermoelectric and thermionic effects, thermionic emission being an analogue of evaporative cooling in which hot carriers are selectively emitted over a barrier (see Figure 1-4).

Interestingly, the materials used to construct solid-state micro-coolers for electronic and optoelectronic devices are often similar to the materials used to make the devices themselves. Integrated heterostructure coolers utilizing SiGe/Si super-

19

$$\frac{\mu(m^*)^{3/2}}{\lambda}$$

(bulk thermoelectric figure-of-merit)

Thermoelectric Coolers

12x larger figure-of-merit
GaAs/AlAs Superlattice
T. Koga et al., *J. Comp.-Aid. Mat. Des.* **4** (1997)

4x larger figure-of-merit
HgCdTe Superlattice
R. Radtke et al., *J. Appl. Phys.* **86** (1999)

300 W/cm² at 300K
InGaAs/InGaAsP SL
C. LaBounty et al., *J. Appl. Phys.* **89** (2002)
InGaAs/InGaAsP Barrier
A. Shakouri et al., *Appl. Phys. Lett* **74** (1999)

680 W/cm² at 345K
SiGe/Si SL
A. Shakouri et al., IPRM (2002)

750 W/cm² at 300K
BiTe/SbTe SL
R. Venkatasubramanian et al., *Nature* **413** (2001)

Devices

Transistors, lasers

Detectors, Mid-IR lasers

High-speed transistors, lasers

High-speed transistors, recent work in SiGe lasers

A. Shakouri and C. LaBounty, ICT, Baltimore, 1999.

Figure 1-5: Convergence of materials for high-performance electric and thermoelectric devices.

lattices have been created that have cooling power densities of 680 W/cm² at 345K; this material system is also used for high-speed transistors [17, 18, 19]. Likewise, superlattice and single-barrier structures in the InGaAs/InGaAsP material system have demonstrated heat removal of 300 W/cm² at 300K; again, this material system has shown promise for high-speed transistors as well as formed the substance of most telecommunication lasers [20, 21, 22]. Further research in GaAs/AlGaAs and HgCdTe material systems for cooling technology has highlighted materials commonly used for electronic and optoelectronic devices such as transistors, lasers, and detectors [23, 24, 25, 26]. As shown in Figure 1-5, there is a wide range of materials for which cooling technology and device technology overlap.

Given the common material basis of solid-state coolers and devices, it seems natural to investigate the cooling properties of devices themselves. This strategy departs
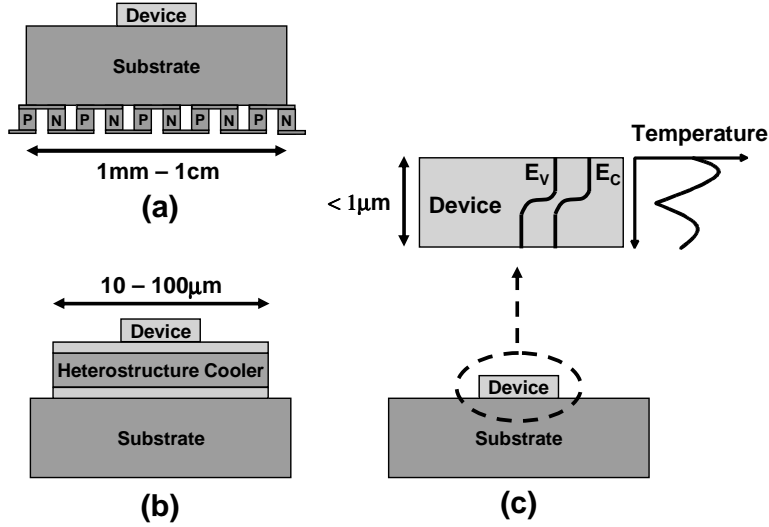
Figure 1-6: Device cooling by (a) Conventional thermoelectric cooler, (b) Integrated heterostructure cooler, (c) Device-internal heat exchange.

from efforts to date in the thermal management of micron-scale hot spots in that it does not involve the placement of an external cooler in the vicinity of the spot (commonly realized through either the mounting of a heat sink or the fabrication of a surface cooler [27]). We move from a paradigm of optimizing the external cooling of a device (as shown in Figures 1-6a and 1-6b) to one of optimizing the device's internal thermal performance. In addition to uncovering ways for a device to dissipate less heat, this can have the benefit of moving the cooling effect directly to the heat source rather than trying to externally cool device-internal hot spots through layers of device material with low thermal conductivity. As illustrated in Figure 1-6c, we must now examine temperature gradients and thermoelectric effects that occur on the same spatial scale as internal device structure, and we must determine how these effects manifest during device operation. Applying thermoelectric concepts to active devices is complicated by the fact that such devices are typically bipolar (operating through the transport of both electrons and holes) whereas traditional external coolers and the thermoelectric theory used to describe them are based on unipolar operation. A thermoelectric description of internal device heat exchange thus requires an extension of traditional thermoelectric theory to include the effects of minority carriers;

this can then be applied to bipolar homostructure and heterostructure devices which are under bias.

1.2   Conventional Thermoelectric Theory

The thermoelectric effect is based on the Zeroth Law of Thermodynamics as applied to phonon and electrical carrier systems within a material; namely, that thermal contact between these systems causes them to tend toward thermal equilibrium. Highly energetic carriers scatter off of low-energy lattice atoms and deposit energy in vibrational modes, while lattice heat contributes likewise to increased carrier energy. The average energy level at which electrical carriers are in equilibrium with the surrounding lattice varies according to both the material composition and the equilibrium temperature. For example, if the ends of a piece of wire are maintained at two different (lattice) temperatures T and $T + \Delta T$, carriers at the warmer end will come into equilibrium at a greater energy than carriers at the cooler end. This energy difference will cause a net diffusion of carriers from one end of the wire to the other, and, according to the Boltzmann transport equation under the equilibrium condition of zero net current flow in the wire, an electric potential ΔV proportional to the temperature difference will develop to oppose the diffusion current [28]. This material-dependent proportionality constant is known as the Seebeck coefficient and is given by $S = \frac{\Delta V}{\Delta T}$ where ΔV is measured by convention as the potential of the cold side with respect to the hot side.

The Seebeck coefficient can be either positive or negative in both metals and semiconductors, but for very different reasons. In metals, free electron theory predicts that both the mean velocity and the mean free path of electrons increase with electron energy. In metals for which this approximation holds, electrons diffuse from the hot region to the cold region, and the Seebeck coefficient is negative ($S \approx -1.8\mu\text{V/K}$ for aluminum at 300K). For some metals (and some semiconductors with complicated band structure), however, the electron-phonon scattering rate increases more quickly with increasing temperature than does the mean velocity, and hence the mean free
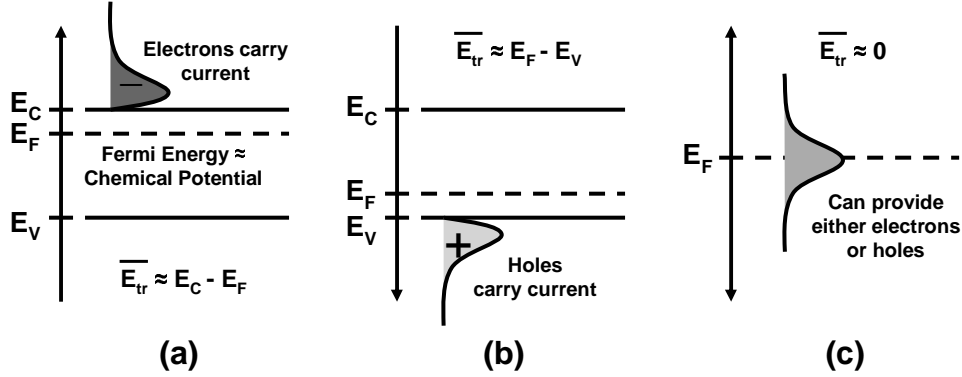
Figure 1-7: Band structure and average transport energy for (a) n-type semiconductor, (b) p-type semiconductor, and (c) metal

path $l = \overline{v}\tau$ decreases. In this case, electrons migrate more easily from the cold region to the hot one, and the Seebeck coefficient is negative ($S \approx 1.84\mu V/K$ for copper at 300K). The Seebeck coefficients of metals in general are small in magnitude due to the fact that all electrical transport occurs at energies near the Fermi level; carriers added or removed at this energy level exchange neither heat nor work with the system.

The analysis is more complicated for semiconductors due to the presence of filled energy bands and the transport of both electrons and holes. The temperature dependence of the mean free path is dominated by an exponential increase of the carrier concentration with increasing temperature. Diffusion in semiconductors thus occurs from hot regions to cold regions, making the Seebeck coefficient negative if the majority carriers are (negatively charged) electrons and positive if the majority carriers are (positively charged) holes. Because these thermally generated carriers are constrained to be above a band edge, they are usually at a distance from the Fermi level and therefore transport more heat energy than in a metal, making the Seebeck coefficient of a semiconductor typically larger than that of a metal ($S \approx -200\mu V/K$ for n-Bi_2Te_3 at 300K). Figure 1-7 illustrates the relationship between band structure and average transport energy $\overline{E_{tr}}$ in doped semiconductors and metals.

The exchange of heat energy between electrical carriers and atoms leads to a related phenomenon that occurs during carrier transport through an interface between two regions of identical temperature and differing Seebeck coefficient. This phe-
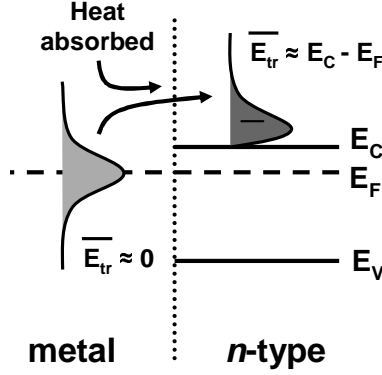
Figure 1-8: Illustration of Peltier heat exchange at an interface between a metal and an n-type semiconductor.

nomenon, known as the Peltier effect, is quantified in terms of the Peltier coefficient $\Pi = TS$ and related to the average transport energy through the elementary charge q by $\overline{E_{tr}} = q|\Pi|$ [29]. As a given carrier current I passes through the interface, the constituent carriers exchange heat energy $\Delta\Pi * I$ with the surrounding atoms to make up the energy difference [30]. This process, illustrated in Figure 1-8 for an n-type/metal interface, is thermodynamically reversible; depending on the sign (direction) of I, the interface can be either heated or cooled.

In the case of a semiconductor layer between two metal contacts, current flow causes carriers to rise to a higher average energy at one metal/semiconductor junction and fall back to their initial average energy at the other junction; heat is thus extracted at one contact and deposited at the other. The current is carried by majority carriers that are either electrons or holes depending on whether the semiconductor is doped with donors (n-type doping) or acceptors (p-type doping) respectively. Since electrons and holes have opposite charge, carriers in n-type and p-type regions flow in opposite directions for a given direction of current flux, and heat will be extracted/deposited at opposite junctions. If a series of alternating n-type and p-type layers are connected to each other by metal contacts, the heat exchange at the junctions will also alternate between cooling and heating, as shown in Figure 1-9. By fabricating a structure such that the cooling and heating junctions are on opposite sides of a flat array, an overall heat flux can be achieved from one side of the array to the other. This
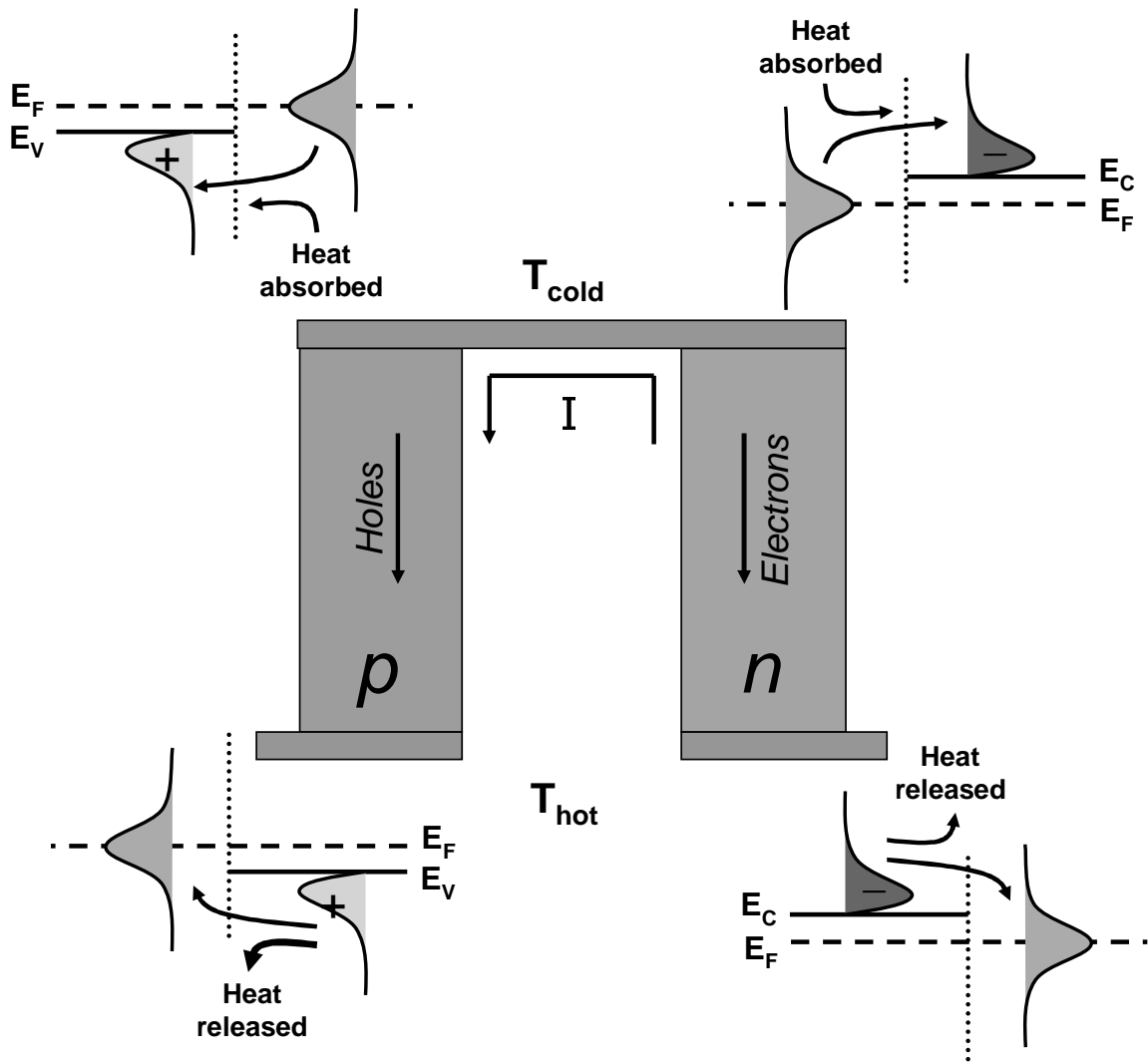
Figure 1-9: Heat exchange in a traditional thermoelectric cooler.

method of connecting an array of n-type and p-type materials with metal junctions such that they are electrically in series and thermally in parallel is the traditional scheme for commercial Peltier coolers. A maximum value of $T_{\text{hot}} - T_{\text{cold}}$ is achieved by optimizing the dimensions and doping of the semiconductor regions to maximize thermal resistivity, electrical conductivity, and Seebeck coefficient. The operation of a traditional Peltier cooler is intrinsically unipolar since the electrical current that contributes to the thermoelectric effect is carried only by majority carriers, and the average energy transported by carriers is constant through each semiconductor region and does not vary with applied voltage bias.

1.3   The Peltier Coefficient and Heterostructures

The traditional Peltier cooler described above relies upon heat exchange that occurs as carriers move between different average energy levels on either side of a semiconductor/metal interface. An energy level difference also occurs across a semiconductor/semiconductor interface at which the material composition changes (heterojunction) or the doping changes (homojunction). Here we will introduce heterojunction transport and leave a more detailed treatment of heterojunction and homojunction thermoelectrics for a later chapter.

Because transport properties such as carrier effective mass change at a heterojunction, it is useful to more precisely define the Peltier coefficient on either side through the Boltzmann transport equation [28, 31]. Here we consider a semiconductor that has parabolic conduction (and valence) band structure in energy E and wave vector $\mathbf{k}$ around the band edge defined by E_c and $\mathbf{k_c}$:

$$E - E_c = \frac{\hbar^2}{2m_e^*}(k - k_c)^2 \tag{1.1}$$

where m_e^* is the electron effective mass. We begin by writing the electron distribution function under non-equilibrium conditions as

$$f_e(\mathbf{k}) = f_{oe} + f_e'(\mathbf{k}) \tag{1.2}$$

where f_{oe} is the equilibrium (symmetric) distribution and $f'_e(\mathbf{k})$ is a small antisymmetric component that results from the action of external forces. The steady-state Boltzmann transport equation can now be written in the relaxation time approximation as

$$\mathbf{v_e} \cdot \nabla_r f_e(\mathbf{k}) + \frac{1}{\hbar}\mathbf{F} \cdot \nabla_k f_e(\mathbf{k}) = -\frac{f_e(\mathbf{k}) - f_{oe}}{\tau_e(k)} = -\frac{f'_e(\mathbf{k})}{\tau_e(k)} \tag{1.3}$$

where $\mathbf{v_e}$ is the Bloch electron velocity, $\mathbf{F}$ is the force of an applied electric field, and $\tau_e(k)$ is the relaxation time [28, 32].

Assuming that the perturbation that brings the system out of equilibrium is small, the non-equilibrium distribution function $f_e(\mathbf{k})$ on the lefthand side of Equation 1.3 can be replaced by the Fermi-Dirac electron equilibrium distribution f_{oe} [28], which is given in terms of the Fermi energy E_F by

$$f_{oe}(E) = \frac{1}{\exp(\frac{E - E_F}{k_{\mathrm{B}}T}) + 1} \tag{1.4}$$

The gradients of Equation 1.3 can now be written through the chain rule as

$$\nabla_r f_e \approx \nabla_r f_{oe} = \frac{\partial f_{oe}}{\partial E}\left(\frac{E_F - E}{T}\nabla_r T - \nabla_r E_F\right) \tag{1.5}$$

and

$$\nabla_k f_e \approx \nabla_k f_{oe} = \frac{\partial f_{oe}}{\partial E}\nabla_k E = \hbar\frac{\partial f_{oe}}{\partial E}\mathbf{v_e} \tag{1.6}$$

Writing the force $\mathbf{F}$ in terms of a potential φ as $\mathbf{F} = q\nabla_r\varphi$, we can rewrite Equation 1.3 as

$$\tau_e(k)\frac{\partial f_{oe}}{\partial E}\mathbf{v_e}\left[\frac{E_F - E}{T}\nabla_r T - \nabla_r(E_F - q\varphi)\right] = -f'_e(\mathbf{k}) \tag{1.7}$$

Because we are interested in transport across a junction, we can now restrict our analysis to a single dimension and make the assumption that the force vector $\mathbf{F}$ only has a component F_x that is in the x direction. We similarly consider only current flow in the x direction, writing the expression for electron current density J_e as

$$J_e = -\frac{q}{4\pi^3}\int_{\mathbb{B}} v_x f'_e(\mathbf{k})\,\mathrm{d}^3\mathbf{k} \tag{1.8}$$

where v_x is the electron velocity in the x direction and $\mathbb{B}$ indicates that the integration over wave vector $\mathbf{k}$ is performed within the first Brillouin zone. Writing the electron mean free path $l_r = \tau_e v_e$ in terms of the scattering parameter r as $l_r = l_o (E - E_C)^r$ [31], and assuming isotropy such that $v_x^2 = v_e^2/3$, we can substitute Equation 1.7 into Equation 1.8 to arrive at:

$$J_e = \frac{q\hbar l_o}{3\pi^2 m_e^*} \left\{ \left[\frac{E_F - E_C}{T} \nabla_r T - \nabla_r (E_F - q\varphi) \right] \mathbb{I}_{1e} - \frac{\nabla_r T}{T} \mathbb{I}_{2e} \right\} \tag{1.9}$$

where

$$\mathbb{I}_{se} = \frac{2m_e^{*2}}{\hbar^4} \int_{EC}^{\infty} \frac{\partial f_{oe}}{\partial E} (E - E_C)^{r+s} \, \mathrm{d}E \tag{1.10}$$

For III-V semiconductors such as GaAs, the dominant scattering mechanism is through optical phonons; for temperatures less than the Debye temperature ($T_D = 344$ K for GaAs), $r_e = r_h = r = \frac{1}{2}$. In some texts on thermoelectrics, the scattering parameter is defined in terms of mean free time: $\tau(E) = \tau_0 (E - E_C)^{r'}$. Since electron velocity is proportional to $\sqrt{E}$, $r' = r - \frac{1}{2}$.

Analogous expressions can be derived for holes:

$$J_h = \frac{q\hbar l_o}{3\pi^2 m_h^*} \left\{ \left[\frac{E_V - E_F}{T} \nabla_r T - \nabla_r (E_F - q\varphi) \right] \mathbb{I}_{1h} - \frac{\nabla_r T}{T} \mathbb{I}_{2h} \right\} \tag{1.11}$$

$$\mathbb{I}_{sh} = \frac{2m_h^{*2}}{\hbar^4} \int_{-\infty}^{E_V} \frac{\partial f_{oh}}{\partial E} (E_V - E)^{r+s} \, \mathrm{d}E \tag{1.12}$$

where

$$f_{oh}(E) = \frac{1}{\exp(\frac{E_F - E}{k_{\mathrm{B}} T}) + 1} \tag{1.13}$$

Recognizing that the electrical conductivity σ and Peltier coefficient Π are defined according to

$$J = J_e + J_h = \sigma \nabla_r \left(\frac{\phi}{q} - \varphi \right) - \frac{\sigma \Pi}{T} \nabla_r T \tag{1.14}$$

and making the approximation that the chemical potential ϕ is approximately equal

to E_F, we arrive at [31]:

$$\sigma = \sigma_e + \sigma_h = -\frac{q^2 \hbar l_o}{3\pi^2} \left(\frac{\mathbb{I}_{1e}\mu_e}{\tau_e} + \frac{\mathbb{I}_{1h}\mu_h}{\tau_h} \right) \tag{1.15}$$

and

$$\Pi = \frac{\frac{\mu_e}{q\tau_e}[(E_F - E_C)\mathbb{I}_{1e} - \mathbb{I}_{2e}] - \frac{\mu_h}{q\tau_h}[(E_V - E_F)\mathbb{I}_{1h} - \mathbb{I}_{2h}]}{\frac{\mathbb{I}_{1e}\mu_e}{\tau_e} + \frac{\mathbb{I}_{1h}\mu_h}{\tau_h}} \tag{1.16}$$

where μ_e and μ_h are the electron and hole mobilities.

In the case for which E_F is much closer to E_C than E_V (i.e. the semiconductor is more n-type and transport is mostly by electrons), $\mathbb{I}_{1e}$ and $\mathbb{I}_{2e}$ are both much greater than $\mathbb{I}_{1h}$ and $\mathbb{I}_{2h}$ since $\frac{\partial f_{oe}}{\partial E}$ in the conduction band is exponentially larger than $\frac{\partial f_{oh}}{\partial E}$ in the valence band. The total Peltier coefficient given in Equation 1.16 can be reduced in this case to the electron component

$$\begin{aligned} \Pi_e \quad &= -\frac{1}{q} \frac{(E_C - E_F)\mathbb{I}_{1e} + \mathbb{I}_{2e}}{\mathbb{I}_{1e}} \\ &= -\frac{1}{q} \frac{\int_{E_C}^{\infty} (E - E_C)^{r+1}(E - E_F)\left(-\frac{\partial f_{oe}}{\partial E}\right) \mathrm{d}E}{\int_{E_C}^{\infty} (E - E_C)^{r+1}\left(-\frac{\partial f_{oe}}{\partial E}\right) \mathrm{d}E} \end{aligned} \tag{1.17}$$

Similarly, if the semiconductor is more p-type and transport is mostly by holes,

$$\Pi_h = \frac{1}{q} \frac{(E_F - E_V)\mathbb{I}_{1h} + \mathbb{I}_{2h}}{\mathbb{I}_{1h}} \tag{1.18}$$

The Peltier coefficient is negative if transport is by electrons ($\Pi_e < 0$) and positive if transport is by holes ($\Pi_h > 0$).

In order to examine an alternate description for Π_e, note that by substituting Equation 1.7 into Equation 1.8 and remaining in **k**-space, σ_e can be written through Equation 1.14 as

$$\sigma_e = \frac{q^2}{4\pi^3} \int_{\mathbb{B}} v_x^2 \tau_e(k) \left(-\frac{\partial f_{oe}}{\partial E}\right) \mathrm{d}k_x = \int_{E_C}^{\infty} \sigma'(E) \left(-\frac{\partial f_{oe}}{\partial E}\right) \mathrm{d}E \tag{1.19}$$

where the "differential" conductivity $\sigma'(E)$, in integrating over an energy shell to change variables from **k**-space to E-space, gives the contribution of a carrier at energy

E to the overall conductivity [29, 33]

$$\begin{aligned} \sigma'(E) \quad &\equiv q^2 \tau_e(E) \iint v_x^2(E, k_y, k_z) \mathrm{d}k_y \mathrm{d}k_z \\ &\approx q^2 \tau_e(E) \overline{v_x}^2(E) \overline{n}(E) \end{aligned} \qquad (1.20)$$

in terms of the average carrier velocity $\overline{v_x}(E)$ and average carrier density $\overline{n}(E)$. Comparing Equation 1.19 with Equation 1.15, it is apparent that the differential conductivity can be substituted in Equation 1.17 (and, analogously, in Equation 1.18) to yield

$$\Pi_e = -\frac{1}{q} \frac{\int_{E_C}^{\infty} \sigma'(E)(E - E_F)\left(-\frac{\partial f_{oe}}{\partial E}\right) \mathrm{d}E}{\int_{E_C}^{\infty} \sigma'(E)\left(-\frac{\partial f_{oe}}{\partial E}\right) \mathrm{d}E} \qquad (1.21)$$

From these expressions of the Peltier coefficient, it is apparent that $|\Pi_e|$ increases as the carrier distribution becomes more asymmetric with respect to the Fermi energy, since $\frac{\partial f_{oe}}{\partial E}$ is sharply peaked near E_F. The magnitude of the Peltier coefficient thus has an inverse relationship with doping (as shown in Figure 1-10), since decreasing doping moves the Fermi energy further into the bandgap while the carriers are constrained to stay in the band.

After the Peltier coefficient is calculated on either side of a heterojunction, the junction current along with the Peltier coefficient difference can be used to calculate the thermoelectric junction heat transfer as before. It is important to bear in mind, however, that heterostructures are usually made up of layers that are very thin and that can be on the order of the carrier energy relaxation length. Since the thermoelectric quantities derived above assume transport between near-equilibrium carrier distributions on either side of the junction, they are not valid within an energy relaxation length of the junction. In the discussion which follows, we will neglect non-equilibrium and junction processes such as thermionic emission and thermal boundary impedances that arise at heterojunctions [34].

In order to apply thermoelectric theory to active devices, we will first examine thermoelectric effects in simple bipolar devices such as homojunction and heterojunction diodes. In Chapter 2, we will also perform modeling to optimize heat exchange
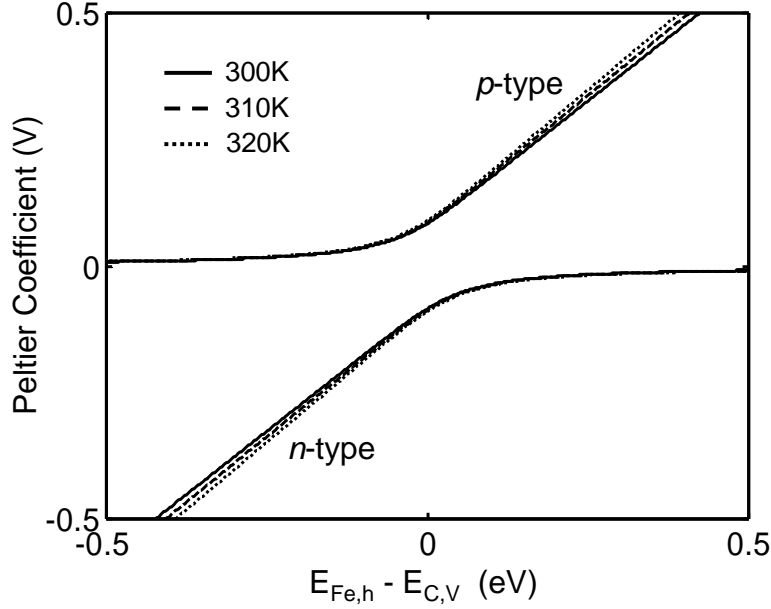
Figure 1-10: Variation of the Peltier coefficient components in GaAs (Π_e for n-type and Π_h for p-type) with Fermi energy and hence with doping. The slight temperature dependence of the Peltier coefficient will be neglected here.

in these devices; having developed these models for simple devices, we will extend our application to a more complicated device, namely the semiconductor laser diode (shown in Figure 1-11). We will begin our treatment of the laser in Chapter 3, formulating models for heat transport both within the device and between the device and its environment that are supplemented experimentally. With this understanding of heat sources and their effect on the laser's temperature, we will be able to judge the effects of thermoelectric heat exchange. In Chapter 4, we will examine the thermoelectric optimization of a laser diode and will propose a new device structure that has enhanced internal Peltier cooling.

To motivate our discussion of thermoelectric effects in bipolar devices, we revisit the conventional Peltier cooler, shown in Figure 1-12a. It is apparent from the position of the Fermi level with respect to the band edge in Figure 1-12c that the Peltier coefficients of minority carriers in the semiconductor regions are much larger in magnitude than the respective majority coefficients; however, the current in this structure is composed exclusively of majority carriers. In order to introduce minor-
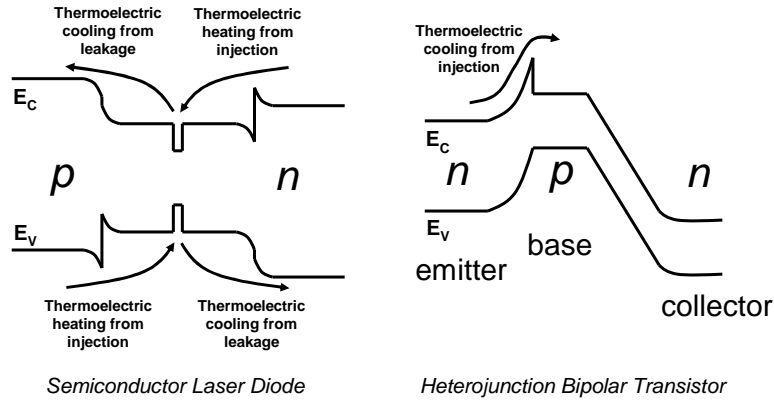
Figure 1-11: Band structures for semiconductor laser diode and heterojunction bipolar transistor.
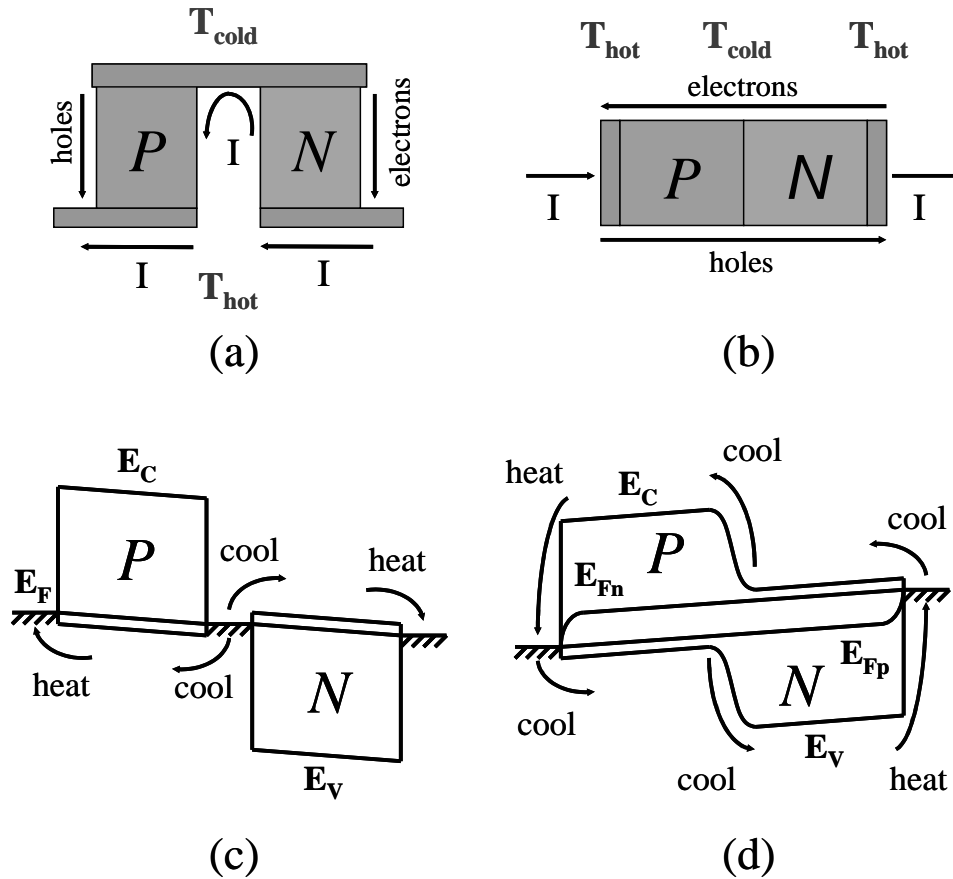
Figure 1-12: Illustration and band structure of (a,c) conventional Peltier cooler and (b,d) p-n junction diode. Note that the direction of current to achieve the same cooling profile is different in the two cases.

ity carriers and examine the resulting thermoelectric heat exchange model, we move to the diode structure of Figure 1-12b, in which the p-type and n-type regions are directly connected.

Chapter 2

Bipolar Thermoelectrics

Active devices such as lasers and transistors rely on the action of both electrons and holes for functions such as amplification and switching. While bipolar transport is crucial to the operation of these devices, the thermoelectric effects that are tied to carrier flow in bipolar devices have not been studied.

The work described in this chapter is an investigation of thermoelectric phenomena in bipolar semiconductors and p-n junctions. In contrast to majority-carrier semiconductors in which a constant material-dependent Peltier coefficient is defined for a given temperature, bipolar devices can be modeled by introducing a bias-dependent Peltier coefficient at interfaces that takes into account the variation of the carriers' average transport energy. It will be shown that this effective Peltier coefficient can vary by orders of magnitude as a function of applied bias, and can give rise to interfacial thermoelectric cooling or heating depending on device parameters. The bias-dependent bipolar Peltier coefficient will be modeled analytically for short-length and long-length diodes, and the different regimes of bias for which cooling is achieved will be described along with the effects of device length, recombination, and doping. Analytical expressions to optimize the thermoelectric effect inside an idealized diode cooler will be presented with numerical results for several common semiconductors, and a figure of merit for internal diode cooling will be introduced. Numerical simulation of thermoelectric effects in heterojunction diodes will then be presented, in order to extend the theory to modern heterostructure devices.

2.1 Previous Work

Optical refrigeration has been proposed as a cooling mechanism in light-emitting semi-conductor devices [35, 36, 37]. In this process, heat energy is transported out of a device through the radiative recombination of thermally-excited carriers whose energies are greater than the electrical bias energy. While this phenomenon is relevant to optical devices in general, cooling has only been measured to date in optically pumped devices, for which Joule heating is negligible. The dominant heating processes in this case are non-radiative recombination and photon absorption; a high external efficiency is thus required in order to demonstrate overall optical cooling [38].

Electrical refrigeration has been demonstrated in semiconductor devices through both thermoelectric effects [39] and thermionic emission [40, 41]. Thermoelectric effects such as Peltier cooling occur when carriers move between regions in which their near-equilibrium energy distribution changes, while thermionic emission is a non-equilibrium effect analogous to evaporative cooling through which hot electrons are selectively emitted across a heterointerface. Although many light-emitting devices are electrically pumped, internal thermoelectric effects arising from electrical transport have generally been neglected as a mechanism for cooling.

The bipolar nature of such devices leads to a thermoelectric description that is significantly more complicated than the traditional bulk model used for conventional Peltier coolers. Previous work has applied descriptions of thermopower in bulk regions where electrons and holes are not in equilibrium [42, 43] to the modeling of heterojunction bipolar transistors [44, 45] and photovoltaic devices in reverse bias and low current conditions [46].

In some of these studies, both electron and hole populations have been considered when modeling transport (for example, in the case of radiation absorption), and each population has been assigned a separate Seebeck coefficient. The variation of these coefficients during device operation, however, has not been examined. This variation is large in most bipolar devices due to the fact that such devices typically exhibit exponential changes in minority carrier concentration at different bias levels.

The relationship between thermoelectric power and carrier concentration causes the minority-carrier Seebeck coefficient to be strongly bias-dependent; it will later be shown that Peltier cooling at a p-n junction can change sign as a function of device bias. Previous thermoelectric analyses of biased diode structures have touched on junction Peltier effects related to minority carrier injection but have not studied their bias dependence, related these effects to a temperature profile, or derived a figure of merit [47].

A description of the operating point dependence of the bipolar thermoelectric coefficients under forward bias is useful for examining the regimes for which device cooling is optimized, especially for devices such as lasers that operate exclusively in forward bias. The analytic expressions derived can be used to tailor the design of devices from a thermoelectric perspective. While net cooling (optical refrigeration) may not be easily achieved in electrically-pumped light-emitting devices, the distribution of heating and cooling sources can be rearranged to reduce the temperature of certain regions of the device.

Here we derive the relevant parameters through analytic means for ideal short-base and long-base homojunction p-n diodes; in comparison with conventional Peltier coolers, we then optimize cooling with respect to region width, current density, and doping for several semiconductor materials [48, 49].

2.2 Peltier Heat Exchange and Carrier Concentration

The Peltier effect describes heat exchange that takes place at the junction of two different materials when electrical current flows between them. It is caused by the fact that the average energy that electrons transport can vary from material to material; when crossing between two such regions, charged carriers compensate for this energy difference by exchanging heat energy with the surrounding lattice. As introduced in Section 1.2, a material's Peltier coefficient Π is related to the average energy (with

respect to the Fermi energy) transported by its electrical carriers through $\overline{E_{tr}} = q|\Pi|$; the amount of heat exchanged for a given current I across a junction is equal to $\Delta\Pi * I$.

For a non-degenerate semiconductor, the Boltzmann approximation to f_o

$$f_{Be}(E) = \exp(\frac{E_F - E}{k_{\mathrm{B}}T}) \tag{2.1a}$$

$$f_{Bh}(E) = \exp(\frac{E - E_F}{k_{\mathrm{B}}T}) \tag{2.1b}$$

is valid and Equations 1.17 and 1.18 can be approximated for electrons and holes as [50]

$$\Pi_e \approx -\frac{k_BT}{q}\left(\frac{E_C - E_F}{k_BT} + (2 + r_e)\right) \tag{2.2a}$$

$$\Pi_h \approx \frac{k_BT}{q}\left(\frac{E_F - E_V}{k_BT} + (2 + r_h)\right) \tag{2.2b}$$

The dependence of the Peltier term on doping is illustrated in Figure 2-1, which explicitly shows the electron Peltier term in n-GaAs. For $E_F < E_C$ (i.e. the Boltzmann limit), the electron Peltier term is equal to $(E_F - E_C)/q$ minus a small offset due to the variation of the average transport energy within the band as described by Equation 2.2. As the doping increases beyond the level approximated by the Boltzmann limit, $E_F - E_C$ increases rapidly, but the Peltier coefficient decreases in magnitude rapidly; the net effect is that the Peltier coefficient increases approximately linearly with the logarithm of the doping. Defining the Peltier coefficient in terms of carrier concentration, then, is exact in the Boltzmann limit and also a good approximation in the Fermi-Dirac limit:

$$\Pi_e \approx -\frac{k_BT}{q}\left(\ln\frac{N_C}{n} + \frac{5}{2}\right) \tag{2.3a}$$

$$\Pi_h \approx \frac{k_BT}{q}\left(\ln\frac{N_V}{p} + \frac{5}{2}\right) \tag{2.3b}$$

for electrons and holes respectively (again assuming $r_e = r_h = \frac{1}{2}$), where n and p are the electron and hole concentrations and $N_{C,V}$ is the effective density of states given

37
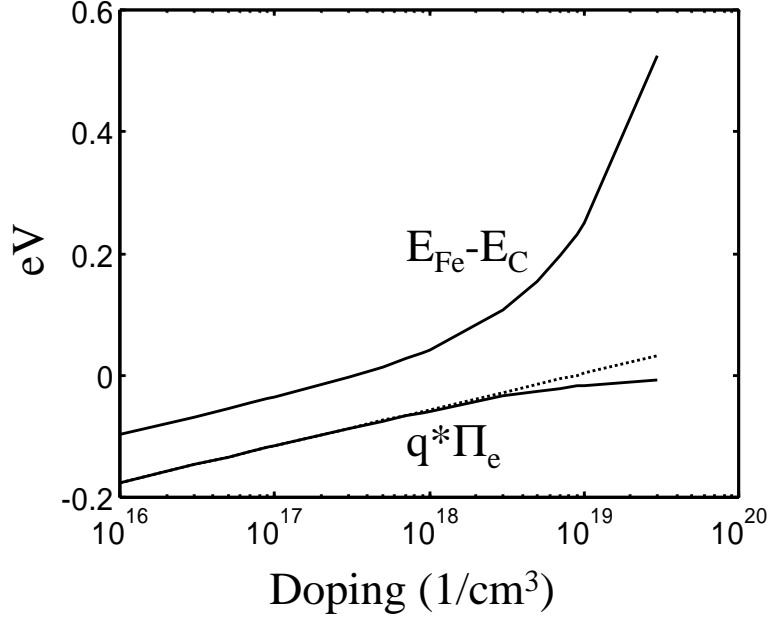
Figure 2-1: Variation of the electron Peltier coefficient in n-GaAs. The solid line is calculated using Fermi-Dirac statistics (Equation 1.17); the dotted line is the linear fit of Equation 2.2a.

by

$$N_{C,V} = 2 \left(\frac{m_{e,h} k_B T}{2\pi\hbar^2} \right)^{\frac{3}{2}} \tag{2.4}$$

This relationship between Peltier coefficient and carrier concentration will prove useful in describing thermoelectric effects that occur inside active devices such as p-n diodes whose operation is governed by concentration gradients.

2.3 Thermoelectric Description of the *P-N* Diode

The p-n diode, a fundamental building block of most modern electronic and opto-electronic devices, is formed by the junction of a p-type semiconductor and an n-type semiconductor (as shown in Figure 1-12b). Under equilibrium conditions, a large built-in electric field exists at the p-n interface, and the drift current caused by this field balances the diffusion current out of the doped regions. As the diode is forward biased, the potential barrier seen by carriers at the interface is decreased, and a net

current develops according to the standard diode equations [51]. Because a drift current typically causes Joule heating as carriers are accelerated by an electric field, one may wonder why an unbiased diode does not spontaneously heat up due to the drift of carriers in the built-in field. The answer is that the diffusion current causes an equal amount of cooling through a thermoelectric effect at the junction. Increasing the device bias causes an increase in the diffusion current relative to the drift current, and therefore a net cooling at the junction must develop.

As electrons diffuse from the n-type region into the p-type region, they gain energy in order to surmount the built-in potential barrier. Analogous to the thermoelectric description of an n/metal interface given above, the average transport energy of electrons increases as they move from being majority carriers in the n-type region to being minority carriers in the p-type region, and heat is removed from the surrounding lattice to make up the difference. The electron Peltier coefficient on either side of the junction can be calculated using Equation 2.3a. As the diode bias is increased, the minority electron concentration in the p-type region increases exponentially, causing a decrease in magnitude of the electron Peltier coefficient for that region (see Figure 1-10). The minority carrier Peltier coefficient is therefore bias-dependent, causing the Peltier cooling to likewise depend on the voltage applied to the device.

Because the same thermoelectric cooling process occurs for holes which move from the p-type region into the n-type region, this junction effect can be seen as bipolar Peltier cooling that depends on the applied bias through the variation of the internal potential [52]. The electron and hole thermoelectric cooling terms superimpose and both work to cool the forward-biased p-n junction. The complementary thermoelectric heating in a diode structure occurs upon the recombination of the minority carriers and can therefore take place in the bulk semiconductor or at an Ohmic contact depending on the device length relative to the recombination length. In the following sections, both limits of device length for a biased diode will be studied; as a first step, however, the unbiased case will be investigated. While the net current is zero for this case and therefore Peltier cooling does not occur, the thermoelectric behavior of the device is measurably changed by the presence of minority carriers.
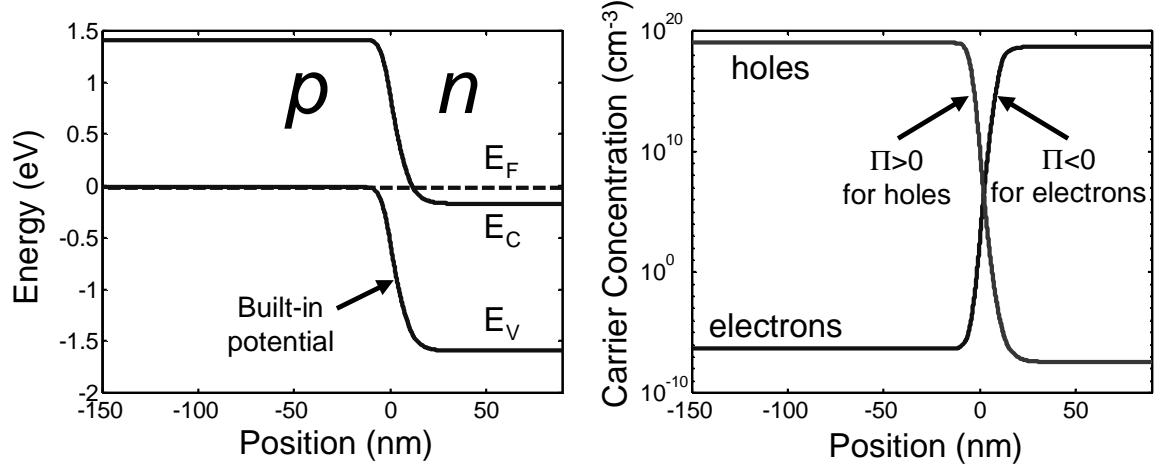
Figure 2-2: Band structure and carrier concentration of an unbiased GaAs p-n diode doped at $N_A = 1 \times 10^{19}$ cm^{-3} (acceptor concentration) and $N_D = 5 \times 10^{18}$ cm^{-3} (donor concentration).

2.4 Unbiased Diode

In a diode at zero bias, electrons and holes are in equlibrium with each other, and a single Fermi level exists for both, as shown in Figure 2-2. Near the junction, in the depletion region, the carrier concentration drops dramatically, suggesting through Equation 2.3 that the thermoelectric terms for electrons and holes both increase in magnitude. Likewise, the Peltier coefficient is expected to change sign abruptly at the junction, as the majority carrier changes between electron and hole.

The diode shown in Figure 2-2 has been examined using the new technique of Scanning Thermoelectric Microscopy (SThEM) [53]. In a setup similar to Scanning Tunneling Microscopy (STM), the diode sample was heated to 320K while the STM tip was at an ambient temperature of 300K. Upon lowering the STM tip to make nanocontact with the sample, the voltage between the tip and sample was measured. This thermoelectric voltage is shown as a function of position in Figure 2-3, along with the voltage $\Pi(320K) - \Pi(300K)$ predicted by Equation 1.16 [54]. The predicted thermoelectric voltage shown has been convolved with a Gaussian profile of width 4nm that corresponds to the approximate carrier scattering length over which equilibrium is expected to occur.
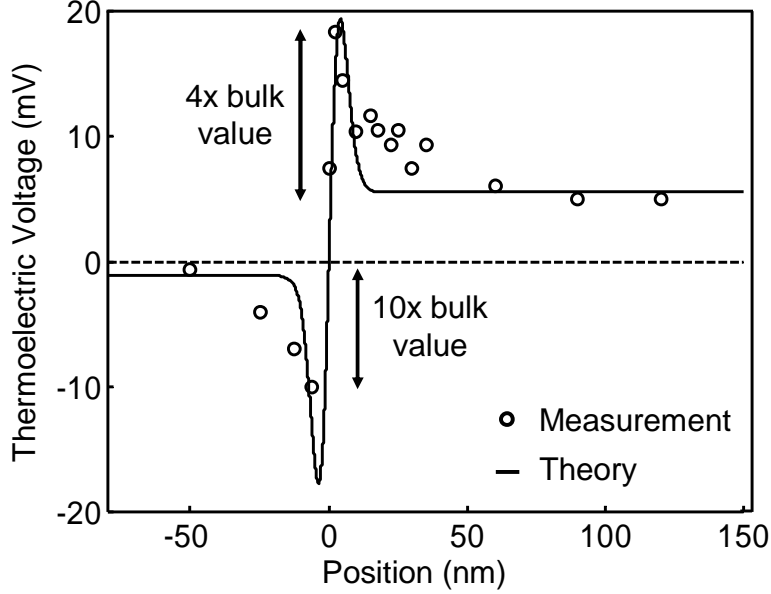
Figure 2-3: Predicted and measured thermoelectric voltage at unbiased GaAs *p-n* diode junction. A large enhancement occurs due to the effects of minority carriers.

Due to the presence of minority carriers, the thermoelectric voltage measured is enhanced by a factor of 10 for electrons and 4 for holes over their bulk values. This large increase suggests that substantial thermoelectric cooling could occur at the diode junction in the presence of net current.

2.5   Diode in Forward Bias

To develop the thermoelectric model of the *p-n* diode when net current is flowing, we examine the idealized structures shown in Figure 2-4. Reflecting the fact that electrons and holes are no longer in equilibrium with each other, there now exist separate quasi-Fermi levels for each population. We must now treat electrons and holes separately, keeping track of two Peltier coefficients (one for each type of carrier) within each region. The total Peltier coefficient given in Equation 1.16 reduces to the separate Π_e and Π_h coefficients given in Equation 2.3 for the electron and hole populations respectively.
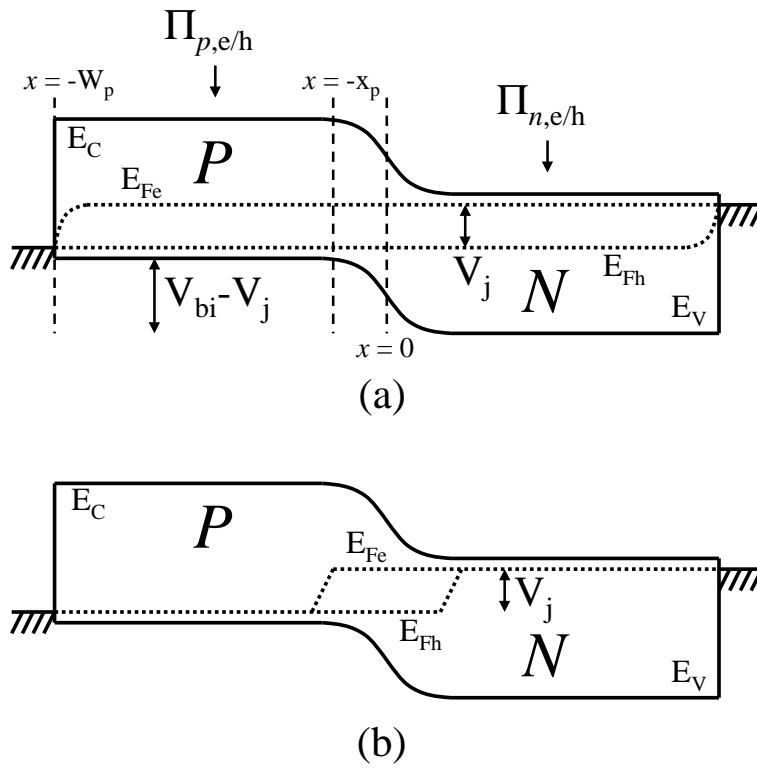
Figure 2-4: Homojunction diode in forward bias for (a) short-length approximation and (b) long-length approximation.

2.5.1 Short-Length Approximation

Under the short-length approximation illustrated in Figure 2-4a, all of the injected minority carriers are assumed to recombine at the ohmic contacts at the boundaries. The injected carrier concentration gradient is assumed to vary linearly between the edge of the depletion region and the ohmic contact, and the Peltier coefficient for injected electrons in the p-type region between the contact and the edge of the depletion region $(-W_p < x < -x_p)$ is given by applying Equation 2.3a with a spatially-varying concentration:

$$
\Pi_{p,e}(x) = \frac{k_B T}{q} \left\{ \ln \left[\frac{n_{po}}{N_C(W_p - x_p)} \right. \right.
$$
$$
\left. \left. \times \left((x + W_p) e^{\frac{qV_j}{k_B T}} - (x + x_p) \right) \right] - \frac{5}{2} \right\} \tag{2.5}
$$

where V_j is the junction voltage drop and $n_{po} = \frac{n_i^2}{N_A}$ is the equilibrium electron concentration in the p-type region in terms of the intrinsic concentration n_i. The doping concentration is given as N_A for acceptors (N_D for donors). We neglect for now voltage drops due to resistance in the quasi-neutral regions that cause the overall bias voltage V to be different from the junction voltage ($IR = V - V_j \approx 0$) and examine these effects in Section 2.6. As carriers experience diffusion cooling while traversing the quasi-neutral region, the logarithmic relationship of concentration to the average transport energy causes the Peltier coefficient $\Pi_{p,e}$ to remain relatively constant throughout much of the region while exhibiting a pronounced increase in magnitude near the contact as shown in Figure 2-5. We neglect this sharp rise in transport energy due to the fact that carriers will immediately release this same amount of energy as they recombine at the contact; the short spatial scale suggests that a temperature gradient will not develop here.

In order to obtain a simple analytic expression for the bias dependence of $\Pi_{p,e}$, we approximate $\Pi_{p,e}$ by its value at the edge of the depletion region ($x = -x_p$) and
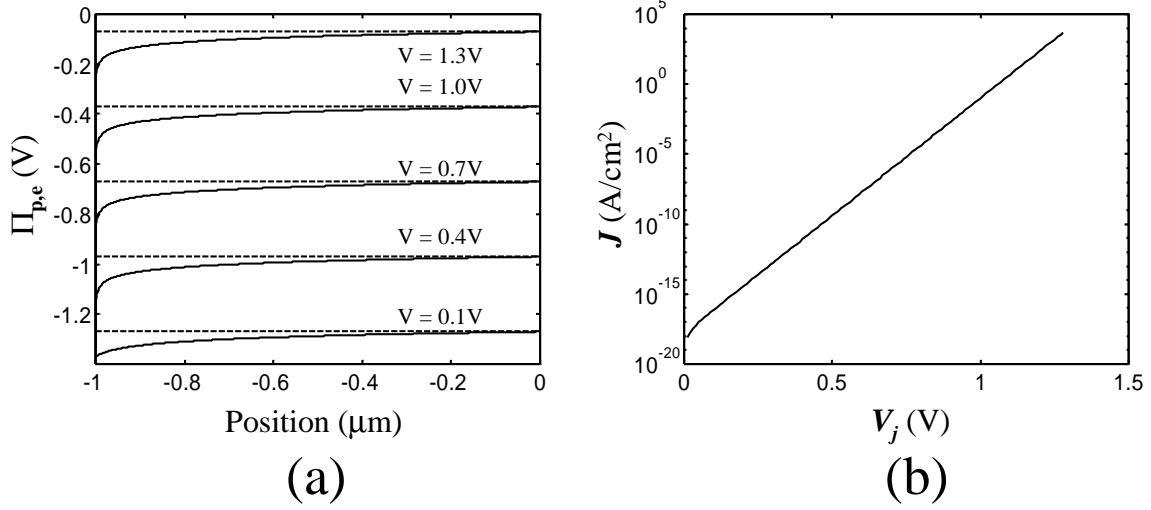
Figure 2-5: (a) Variation of $\Pi_{p,e}$ with applied voltage and in the p-type quasi-neutral region $(-W_p < x < -x_p \approx 0)$ of a 2 μm GaAs diode doped symmetrically at $N_D = N_A = 1 \times 10^{18}$ cm^{-3}. Dotted lines refer to the effective value used for the region as given in Equation 2.6. (b) Current-voltage relationship.

rewrite Equation 2.5 as

$$
\begin{aligned}
\Pi_{p,e} \quad &= \Pi_{n,e} - (V_{bi} - V_j) \\
&= V_j - \frac{k_B T}{q}\left(\ln\frac{N_C}{n_{po}} + \frac{5}{2}\right) \\
&= -\frac{k_B T}{q}\left(\ln\frac{N_C J_0}{n_{po}(J_0 + J)} + \frac{5}{2}\right)
\end{aligned}
\tag{2.6}
$$

where V_{bi} is the built-in voltage given by

$$
V_{bi} \approx \frac{k_B T}{q}\ln\frac{N_A N_D}{n_i^2}
\tag{2.7}
$$

and J_0 is the diode saturation current density given in terms of the electron and hole mobilities $\mu_{e,h}$ by

$$
J_0 = n_i^2 k_B T\left(\frac{\mu_e^A}{W_p N_A} + \frac{\mu_h^D}{W_n N_D}\right)
\tag{2.8}
$$

where μ_e^A refers to the electron mobility in a region of doping concentration N_A. The

44
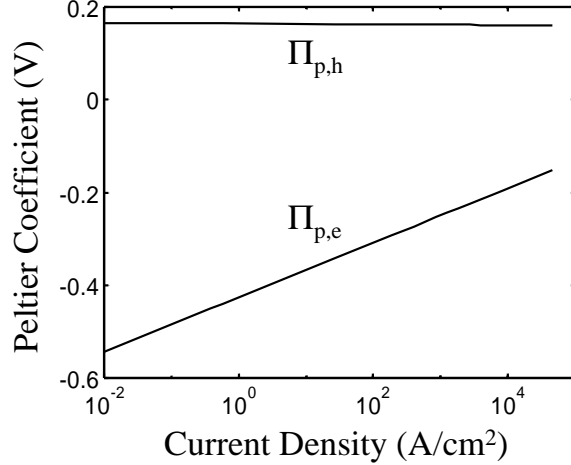
Figure 2-6: Bias dependence of the bipolar Peltier coefficient of the *p*-type region

diode current density is related to the applied voltage by

$$J = J_0 \left(\exp \frac{qV_j}{k_B T} - 1 \right) \tag{2.9}$$

Since we are using the linear approximation as shown in Figure 2-1, we apply Equation 2.7 even for large doping densities. The validity of this approximation will be examined at the end of this section.

The decrease of the bipolar Peltier coefficient within the *p*-type region as the current bias is increased is depicted in Figure 2-6. Notice that the majority-carrier component stays roughly constant, while the minority-carrier component does not.

The difference in Peltier coefficient (for both electrons and holes) on either side of the depletion region is equal to $\Delta \Pi = V_{bi} - V_j$. Due to the fact that carriers are symmetrically distributed around the Fermi level in a metal, the Peltier coefficient can be approximated as zero inside the ohmic contacts. Noting that the minority carriers recombine at the contacts and release heat energy qV_j, the heat exchange density at the *p*/metal contact (in the absence of other heating processes such as contact resistance) can be written as

$$Q_{p/\text{metal}} = -J_e(\Pi_{p,e} - V_j) - J_h \Pi_{p,h} \tag{2.10}$$

where J_e and J_h are the electron and hole current densities (both taken to be positive) and $\Pi_{p,e}$ and $\Pi_{p,h}$ are the electron and hole Peltier coefficients in the p-type region given in Equations 2.6 and 2.3b. Similar equations can be derived for the n-type region; the heat exchange at the junction is given by

$$
\begin{align}
Q_j &= J_e(\Pi_{p,e} - \Pi_{n,e}) - J_h(\Pi_{n,h} - \Pi_{p,h}) \tag{2.11a}\\
&\approx -J(V_{bi} - V_j) \tag{2.11b}
\end{align}
$$

where $J = J_e + J_h$.

Notice that the total heat exchange given by the sum of the contact terms and the junction term is equal to JV, which is the total bias power on the device; the definition of the Peltier coefficient satisfies energy conservation. Since the bias current density J is related exponentially to the voltage V_j, the amount of cooling at the junction increases as the device is increasingly forward biased, until V_j approaches V_{bi}. By setting $\frac{\partial Q_j}{\partial V_j} = 0$, we see that the cooling power is maximized when $V_{bi} - V_j = \frac{k_B T}{q}$. This value of the junction barrier height is a similar conditions to that cited for heterobarrier coolers utilizing thermionic emission [55]. Using this value in Equation 2.11b gives

$$
Q_{j,\text{opt}} = -\frac{1}{e}\left(\frac{k_B T}{q}\right)^2\left(\frac{\tilde{\sigma}_p}{W_p} + \frac{\tilde{\sigma}_n}{W_n}\right) \tag{2.12}
$$

where we define "minority conductivities" $\tilde{\sigma}_p \equiv q\mu_e^A N_D$ and $\tilde{\sigma}_n \equiv q\mu_h^D N_A$; e.g. the minority conductivity for the p-type region is the product of the electron mobility μ_e^A in that region times the donor concentration in the n-type region. If both N_D and N_A are increased, the minority mobilities decrease, but the minority conductivities show an overall increase; thus, diode coolers typically do not have an optimum doping as majority-carrier coolers do. As shown in Figure 2-7, the maximum junction cooling power occurs for the maximum doping.

Figure 2-8 plots Q_j for a symmetric ($W_n = W_p = 0.5\mu$m) GaAs diode at several different symmetric ($N_D = N_A$) doping levels. Carrier transport energies were cal-
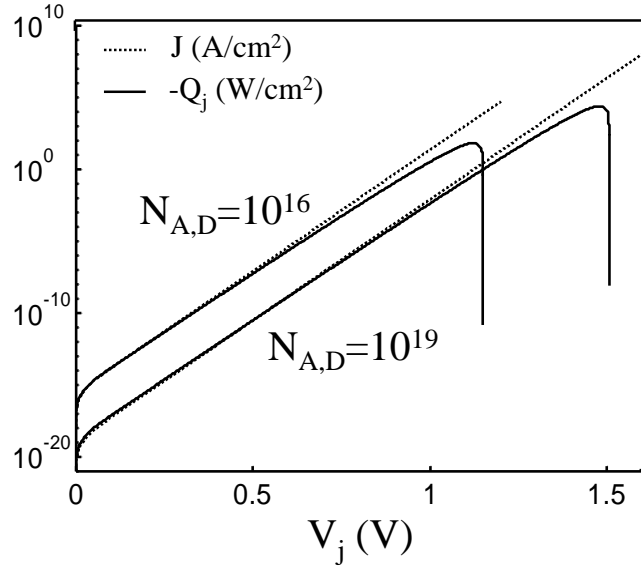
Figure 2-7: The variation of J and $-Q_j$ with increasing V_j in a symmetrically-doped 1 μm GaAs diode at two different doping levels.
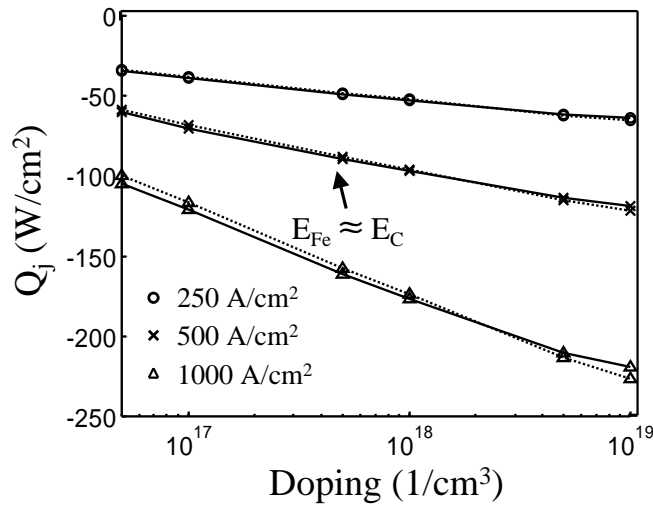
Figure 2-8: The variation of Q_j with doping in a symmetrically-doped 1 μm GaAs diode: dotted lines are derived from Equation 2.11b; solid lines are derived from Equation 2.11a using drift-diffusion simulations and reflect corrections due to nonzero recombination and Fermi-Dirac statistics at high doping levels.

47
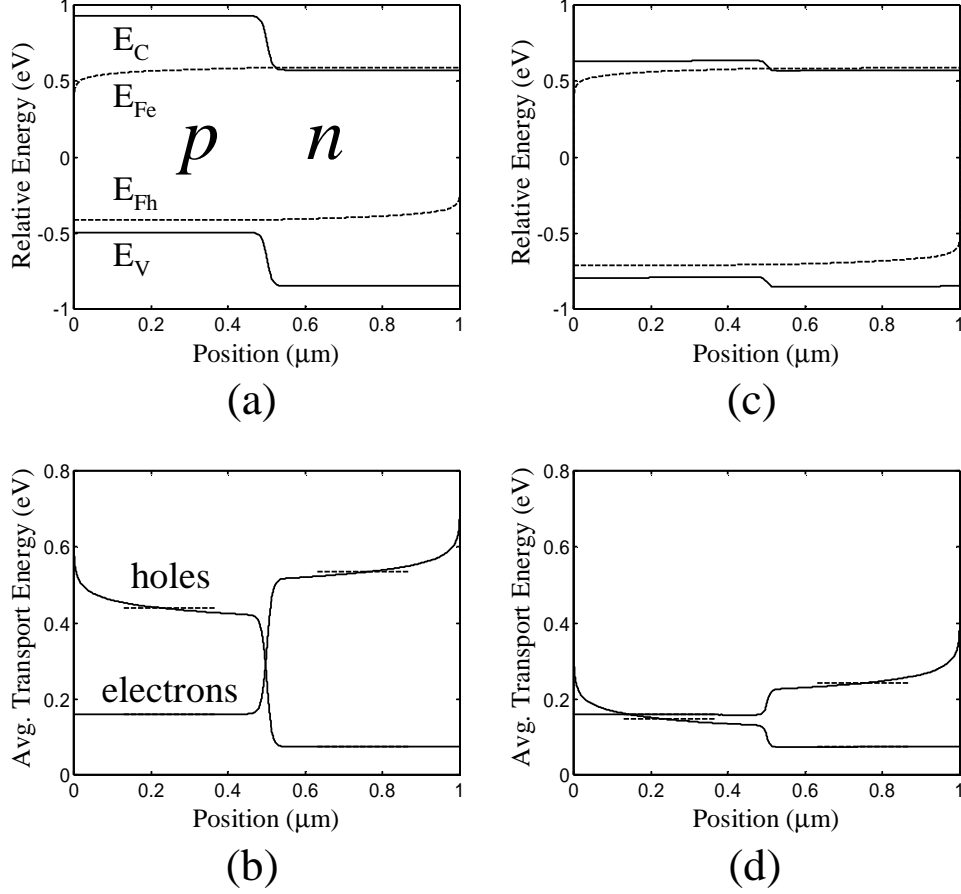
Figure 2-9: Homojunction diode: band structure (a,c) and average transport energy $\overline{E_{tr}} = q|\Pi|$ (b,d) at 1.00V and 1.30V respectively for a 1 μm GaAs diode doped symmetrically at $N_D = N_A = 5 \times 10^{17}$ cm^{-3}. In (B,D) the dotted lines refer to the averaged Peltier values used to calculate Q_j.

culated by solving the drift-diffusion equations self-consistently with Poisson's equation [56, 57, 58], and the bipolar Peltier coefficients used in Equation 2.11a were calculated by averaging Equations 1.17 and 1.18 for carriers in the quasi-neutral regions outside the diode depletion width (rather than simply taking the value at $x = x_p$), as shown in Figure 2-9. There is generally good agreement with Equation 2.11b. This can also be seen in Figure 2-10, which also compares the analytic expressions derived above to numeric solutions. Notice that the error in the linear approximation depicted in Figure 2-1 is small compared to the total difference in Peltier coefficients across the junction $\Delta\Pi \approx V_{bi} - V_j$ shown in Figure 2-10. The small error evident in the plots of Q_j at low doping levels in Figure 2-8 is due to the resistance of the n-type
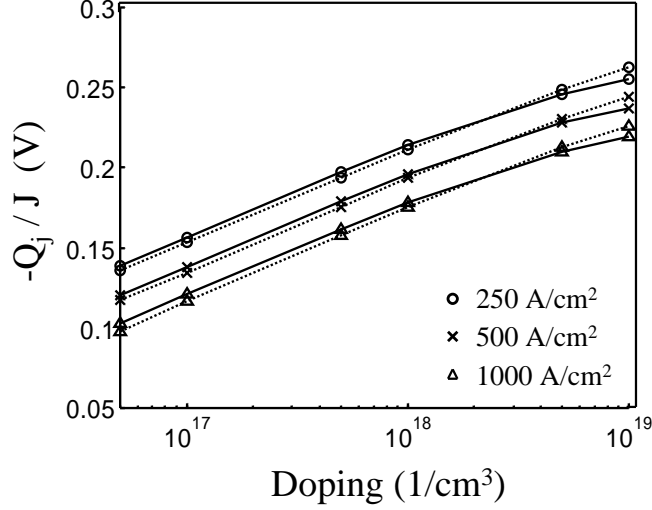
Figure 2-10: Comparison of analytic and numeric solutions for 1 μm GaAs diode: $-\frac{Q_j}{J} = V_{bi} - V_j$ computed numerically from Equation 2.11a (solid lines) and approximated by Equation 2.11b (dotted lines).

and p-type regions that causes an additional voltage drop.

The change in effective Peltier coefficient for electrons and holes at the diode's junction takes place over their respective depletion widths, whose sum is given in terms of the dielectric permittivity ϵ_s by

$$x_{\text{tot}} = x_n + x_p = \sqrt{\frac{2\epsilon_s}{q}(\frac{N_A + N_D}{N_A N_D})(V_{bi} - V_j)} \qquad (2.13)$$

Notice that increasing the doping level leads to an increased V_{bi} and therefore a larger total cooling at the junction through Equation 2.11. For the symmetric case ($N_D = N_A$), assuming $N_D, N_A > n_i$, the cooling region width x_{tot} also decreases with increased doping; this implies more concentrated cooling at the diode junction. However, calculation of the spatial variation of the cooling term within the depletion region is not described by this thermoelectric analysis due to the comparable magnitudes of the energy relaxation length and depletion width.

2.5.2 Long-Length Approximation

For a biased diode in which the p-type and n-type regions are much longer than the electron and hole diffusion lengths, all of the injected carriers are expected to recombine in the quasi-neutral regions rather than at the contacts. This approximation is depicted in Figure 2-4b.

The bias power dissipated in the device is given by

$$JV_j = P_{\text{recomb}} - J(\Pi_{p,h} - \Pi_{n,e}) \tag{2.14}$$

We can rewrite the power dissipated through recombination in terms of the bandgap E_g as

$$P_{\text{recomb}} = J\frac{E_g}{q} - J(V_{bi} - V_j) \tag{2.15}$$

where we have made use of the relation

$$\Pi_{p,h} - \Pi_{n,e} = \frac{E_g}{q} - V_{bi} \tag{2.16}$$

which is valid for homojunction diodes in the Boltzmann approximation. The recombination power given in Equation 2.15 is made up of two components E_g and $V_{bi} - V$ that are related to the recombination energy and the energy gain of carriers prior to recombination respectively.

If a fraction η_{opt} of the recombination power is radiative and leaves the diode, the total heat density (neglecting resistive drops) can be written as

$$Q_{\text{total}} = J(V - \frac{E_g}{q}\eta_{opt}) \tag{2.17}$$

which for $Q_{\text{total}} < 0$ yields the traditional constraint for optical refrigeration [35, 36].

The long-length approximation is similar to the behavior of a semiconductor laser diode, which is designed so that all carriers recombine in an intrinsic region between the p-type and n-type layers. We will return in Section 3.3 to analyze internal heat exchange and thermoelectric effects that occur in a laser diode.

2.6 Temperature

For a layered device structure with thermal conductivity $k(x)$, the heat source distribution $\mathcal{Q}(x)$ produces a steady-state temperature profile $T(x)$ according to the one-dimensional heat equation $\frac{\mathrm{d}}{\mathrm{dx}}\left(k\frac{\mathrm{d}T}{\mathrm{d}x}\right) = -\mathcal{Q}$, where $\mathcal{Q}$ is in units of W/cm³. Heat flux is governed by $k\frac{\mathrm{d}T}{\mathrm{d}x} = -Q$, where Q is in units of W/cm² as before. In order to examine the effects of the rearrangement of the heat sources in a diode, we compare its internal temperature profile to that of the traditional unipolar Peltier cooler shown in Figure 1-12a.

2.6.1 Conventional Thermoelectric Cooler

For a traditional Peltier cooler with n-type and p-type branches of areas A_n and A_p respectively, the net heat transported by thermoelectric effects from the cold contact is countered by both thermal conduction from the hot contact and Joule heating within the branches. The total cooling power q_c at the cold contact of the traditional cooler is given (in units of Watts) in terms of the Seebeck coefficients of the p-type and n-type regions S_p and S_n by

$$q_c = (S_p - S_n)IT_{\mathrm{cold}} - K(T_{\mathrm{hot}} - T_{\mathrm{cold}}) - \frac{I^2 R}{2} \tag{2.18}$$

where K is the thermal conductance of the n-type and p-type regions in parallel:

$$K = k_p\frac{A_p}{W_p} + k_n\frac{A_n}{W_n} \tag{2.19}$$

and R is the electrical resistance of the two regions in series:

$$R = \rho_p\frac{W_p}{A_p} + \rho_n\frac{W_n}{A_n} \tag{2.20}$$

Here we have made the assumption that half of the Joule heat produced in the branches flows to each contact. The electrical resistivity of the n-type region ρ_n is

given by

$$\rho_n = \frac{1}{q\mu_h^{p+n}p + q\mu_e^{p+n}n} \approx \frac{1}{q\mu_e^D N_D} \qquad (2.21)$$

As stated earlier, the Seebeck coefficient S is related to the Peltier coefficient by $\Pi = TS$. By maximizing q_c with respect to current, we find [30] that the maximum temperature difference $T_{\text{hot}} - T_{\text{cold}}$ for the traditional cooler can be written in terms of the figure of merit Z by

$$(T_{\text{hot}} - T_{\text{cold}})_{\text{max}} = \frac{1}{2}ZT_{\text{cold}}^2 \qquad (2.22)$$

where

$$Z = \frac{(S_p - S_n)^2}{KR} \qquad (2.23)$$

It can be shown that KR is minimized when

$$\frac{W_n A_p}{W_p A_n} = \left(\frac{\rho_p k_n}{\rho_n k_p}\right)^{\frac{1}{2}} \qquad (2.24)$$

The figure of merit reflects the optimal balance of Joule heating, heat conduction, and Peltier cooling.

2.6.2 Diode Cooler

For a diode, we consider the short-length case in which both ohmic contacts are heat sunk at a temperature T_0; here we can calculate the maximum temperature difference $(T_0 - T_j)_{\text{max}}$ that can be achieved between the heat sink and the diode junction. From the perspective of Figure 1-12, we connect the p-type and n-type regions directly together at the "cold" contact and let $T_j = T_{\text{cold}}$ and $T_0 = T_{\text{hot}}$. We neglect thermoelectric voltage drops caused by temperature gradients across the semiconductor regions.

By making an analogy to Equation 2.18 and using Equation 2.11b, we can write

the cooling power density Q_j at the junction in the short-length limit as

$$Q_j = J(V_{bi} - V_j) - \frac{K}{A}(T_0 - T_j) - \frac{J^2 RA}{2} \tag{2.25}$$

where the nonzero resistance of the quasi-neutral regions is taken into account through $V_j = V - JRA$ and half of the Joule heat is assumed to flow back to the junction [30]. The device is assumed to have uniform cross-section: $A_p = A_n = A$. From a comparison of Equations 2.18 and 2.25 we see that the effective Seebeck coefficients for the diode are dependent on bias as well as on geometry and material.

The maximum cooling power density, found by setting $\frac{dQ_j}{dJ} = 0$, is given by the condition

$$V_{bi} - V_{j,\text{opt}} = \frac{k_B T_j}{q} + J_{\text{opt}} RA \tag{2.26}$$

where $J\frac{dV_j}{dJ} \approx \frac{k_B T}{q}$ for a diode in the short-length approximation (cf. Equation 2.9). Equation 2.26 does not have an analytic solution for the value of J_{opt}, but we can arrive at a numeric solution by rewriting it as

$$1 + f + \ln f = \ln\left[\left(\frac{\tilde{\sigma}_p}{W_p} + \frac{\tilde{\sigma}_n}{W_n}\right)\left(\rho_p W_p + \rho_n W_n\right)\right] \tag{2.27}$$

where $f \equiv \frac{q}{k_B T_j} J_{\text{opt}} RA$. Likewise, we can write

$$KR = k\left(\frac{1}{W_p} + \frac{1}{W_n}\right)\left(\rho_p W_p + \rho_n W_n\right) \tag{2.28}$$

where we have assumed $k_n = k_p = k$.

In order to calculate the optimal diode geometry and bias, we first examine the symmetric case ($N_A = N_D$) and later look briefly at the asymmetric case. Equation 2.12 suggests that both the p-type and n-type regions should be maximally doped in order to achieve the most cooling, making the symmetric case especially important. Equation 2.27 now simplifies to

$$1 + f + \ln f = \ln\left(W^* + \frac{1}{W^*} + \mu^* + \frac{1}{\mu^*}\right) \tag{2.29}$$
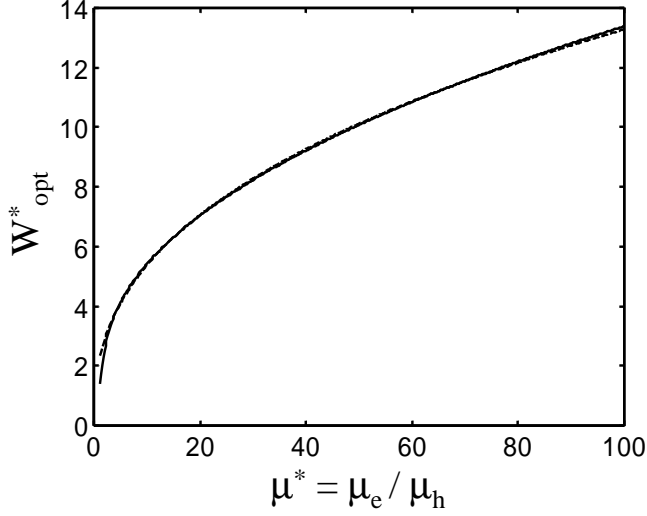
Figure 2-11: W^*_{opt} (solid line) and fit $W^*_{\text{opt}} = 2.17(\mu^*)^{0.39}$ (dotted line)

where $W^* \equiv \frac{W_n}{W_p}$ and $\mu^* \equiv \frac{\mu_e}{\mu_h}$. Equation 2.28 can be written as

$$KR = k\rho_n \frac{(W^* + 1)(W^* + \mu^*)}{W^*} \tag{2.30}$$

The maximum value of the temperature difference $\Delta T = T_0 - T_j$ is then given by setting $Q_j = 0$ in Equation 2.25 so that the cooling at the junction exactly balances the heat conduction:

$$\begin{aligned}
\Delta T &= \frac{1}{2k\rho_n}\left(\frac{k_B T_j}{q}\right)^2 \frac{(f^2 + 2f)W^*}{(W^* + 1)(W^* + \mu^*)} \\
&= \frac{1}{2k\rho_n}\left(\frac{k_B T_j}{q}\right)^2 g(W^*, \mu^*) \tag{2.31}
\end{aligned}$$

The optimal value of W^* can be found in terms of μ^* by the condition $\frac{\partial \Delta T}{\partial W^*} = 0$, as shown in Figure 2-11; for typical devices, $\mu^* > 1$. The function $g(W^*, \mu^*)$ defined in Equation 2.31 can now be expressed as a function of just μ^*, as shown in Figure 2-12; g_{opt} is very closely approximated by a first-order polynomial in $\ln \mu^*$. Also shown is the value of g for a diode with equal region widths ($W^* = 1$) for comparison. The
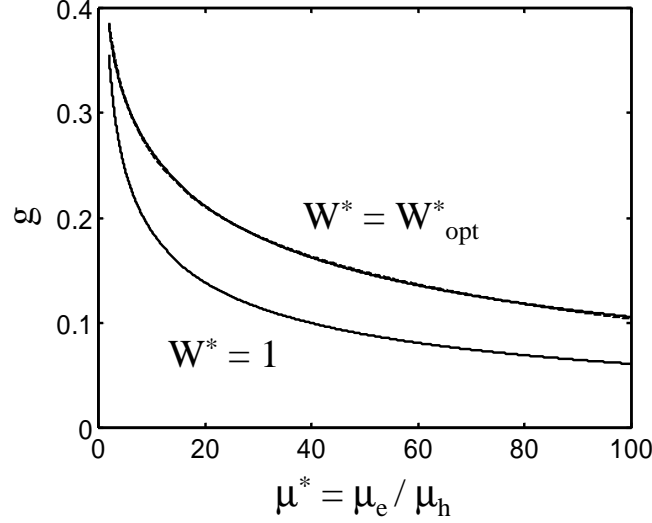
Figure 2-12: $g(\mu^*)$ for $W^* = W^*_{\text{opt}}$ and for $W^* = 1$ (solid lines); fit $g_{\text{opt}} = 0.42 - 0.07 \ln \mu^*$ (dotted line).

optimal value of ΔT can now be derived from Equation 2.31:

$$\Delta T_{\text{opt}} = \frac{1}{2k\rho_n} \left(\frac{k_B T_j}{q} \right)^2 \left(0.42 - 0.07 \ln \frac{\mu_e}{\mu_h} \right) \tag{2.32}$$

From comparison with Equations 2.23 and 2.22 we see that the effective Seebeck coefficients for the diode after optimizing for current density and geometry are proportional to $\frac{k_B}{q}$ by a factor which is dependent on the ratio of the mobilities. Notice that increasing the total diode width $W_{\text{tot}} = W_n + W_p$ (while keeping W^* constant) has no effect on ΔT_{opt} but does cause the optimal current J_{opt} to decrease, since f is fixed but R increases.

In order to examine the dependence of ΔT on current density and width ratio, we plot $\frac{\Delta T}{\Delta T_{\text{opt}}}$ versus these variables in Figure 2-13 for the value of $\mu^* = 30$ (typical for many diodes). As we move the current density away from its optimal value, we keep W^* fixed at its optimal value for $J = J_{\text{opt}}$, and vice versa. For $J < J_{\text{opt}}$ and for $W^* < W^*_{\text{opt}}$, conduction from the side heat sinks dominates, while for $J > J_{\text{opt}}$ and for $W^* > W^*_{\text{opt}}$, Joule heating dominates.

Values of W^*_{opt}, J_{opt}, and ΔT_{opt} are plotted for symmetrically-doped diodes of several semiconductor materials in Figures 2-14, 2-15, and 2-16 respectively. The
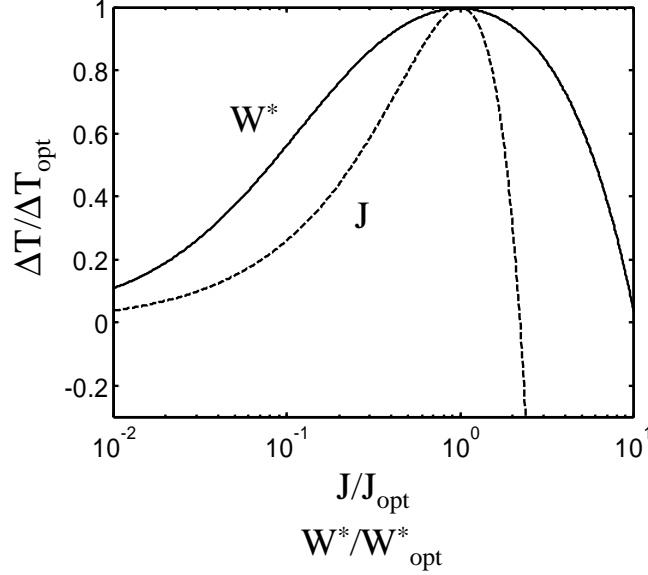
Figure 2-13: Variation of ΔT around the optimality point defined by Equation 2.32 for $\mu^* = 30$.

	k (W/cmK)	μ_e[1] (cm^2/Vs)	μ_h[1] (cm^2/Vs)	μ^{*}[2]
Si	1.31	3200-100	560-100	6-1
GaAs	0.55	8000-3000	400-100	20-30
InSb	0.18	100000-10000	1000-400	100-25
Ga$_{0.47}$In$_{0.53}$As	0.05	18000-3000	800-100	22-32
Hg$_{0.8}$Cd$_{0.2}$Te	0.01	20000-5000	600-60	34-86

Table 2.1: Material parameters of several semiconductors. [1]Doping range: 10^{16}-10^{19}cm^{-3}. [2]Calculated.

material parameters used are summarized in Table 2.1. From Figure 2-14 we see that W_p must often be kept small in order to ensure that W_n is less than the diffusion length and satisfies the short-length approximation. In Figure 2-17 we plot the optimal current as a function of total region width W_{tot} for several materials doped symmetrically at 1×10^{19} cm^{-3}. To examine the large internal diode temperature gradients that can occur in a material with very low thermal conductivity and high mobility such as Hg$_{0.8}$Cd$_{0.2}$Te, we plot the temperature profile of a 2 μm device doped symmetrically at 1×10^{19} cm^{-3} for several values of W^* in Figure 2-18, assuming $J = J_{\text{opt}} = 3.85 \times 10^5$A/cm^2. In Figure 2-19, we assume $W^* = W^*_{\text{opt}} = 12.5$ and plot
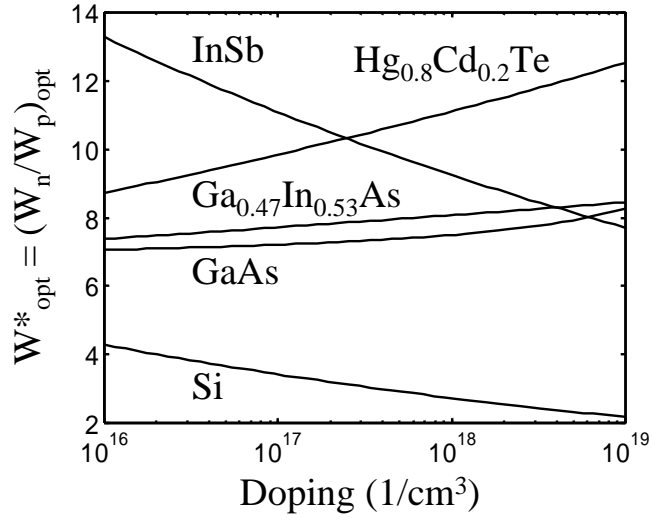
Figure 2-14: Optimal value of W^* for several semiconductor diode materials.
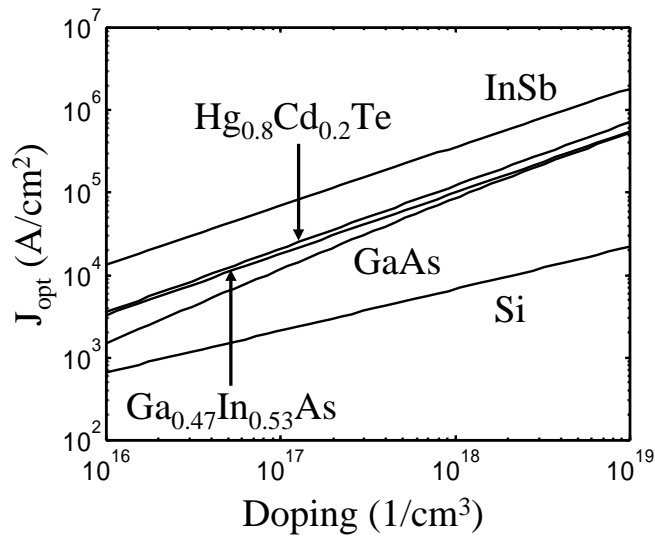
Figure 2-15: Optimal value of J for several semiconductor diode materials, assuming $W_n = 1$ μm.
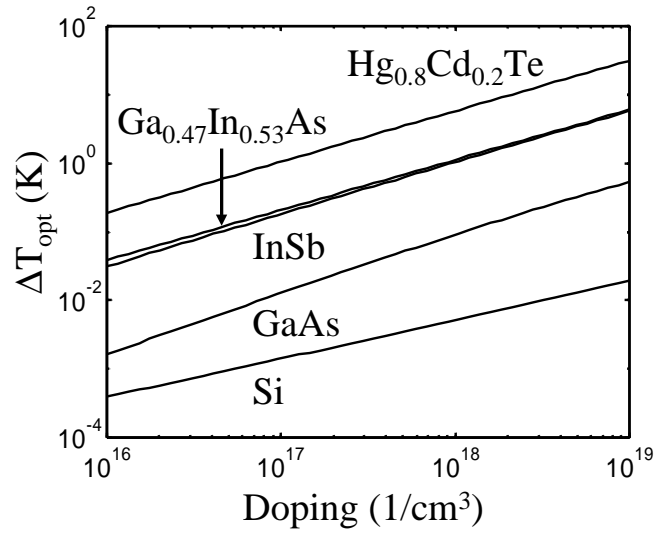
Figure 2-16: Optimal value of ΔT for several semiconductor diode materials.
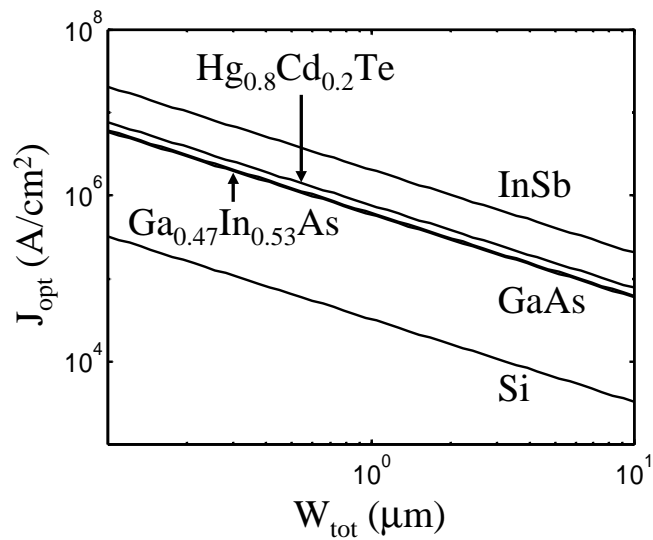
Figure 2-17: J_{opt} for several semiconductor diode materials doped symmetrically at 1×10^{19} cm^{-3}.
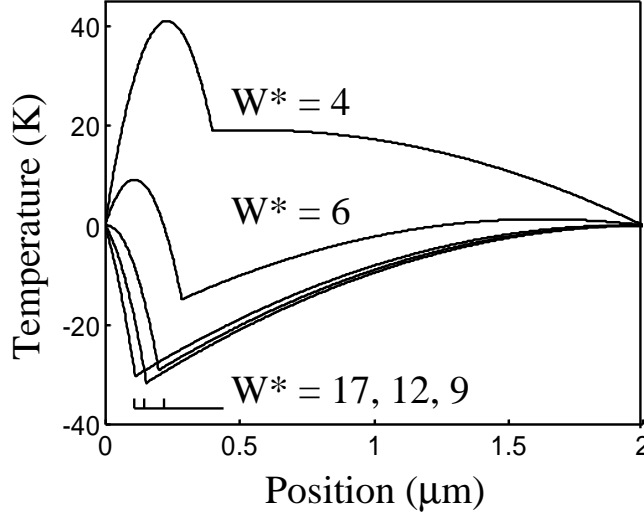
Figure 2-18: Internal temperature profile (with respect to $T_0 = 0$) at several values of W^* for a 2 μm $Hg_{0.8}Cd_{0.2}Te$ diode doped symmetrically at 1×10^{19} cm^{-3}, assuming $J = J_{opt} = 3.85 \times 10^5 A/cm^2$. The internal temperature minimum occurs at the junction for $T_{min} < 0$.

the temperature profile for several values of J.

In the above solution to Equation 2.25 we have assumed symmetric doping. To examine the asymmetric case, we plot the optimal temperature and optimal current density for a range of doping profiles for a $Hg_{0.8}Cd_{0.2}Te$ diode in which $W_p = W_n = 1\mu$m, as shown in Figures 2-20 and 2-21. As implied by Equation 2.12, the best performance is achieved at the highest doping levels (unlike conventional majority-carrier thermoelectrics, in which there is an optimum carrier concentration). When W^* is set to 1 instead of W_{opt}, the optimal current density decreases, but it comes at the cost of a lower optimal temperature.

Moving the junction to the center of the diode can be beneficial if the heat sinks are not ideal. The cooling shown in Figures 2-16 and 2-20 depends on the constraint that both contacts are heat sunk at a constant temperature, while a real device can have contact resistance and non-ideal heat sinking. For example, if a diode is grown on a thick semiconductor substrate, carriers injected from the top side will recombine over their diffusion length within the substrate; some of this heat will be conducted back to the junction. Depending on the device geometry, this can decrease the cooling
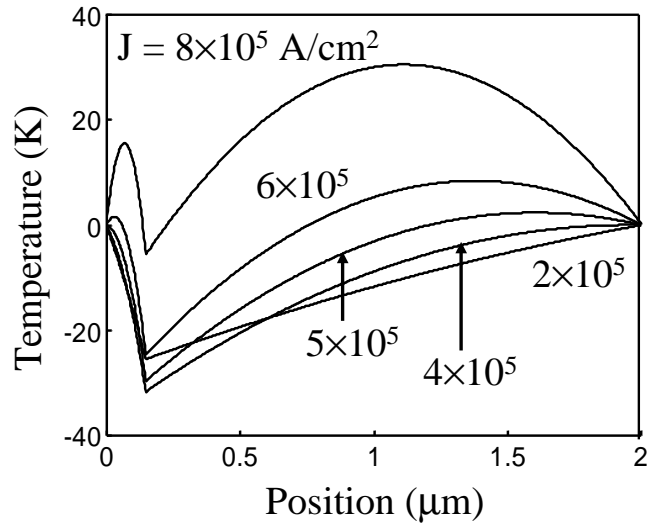
Figure 2-19: Internal temperature profile (with respect to $T_0 = 0$) at several values of J for a 2 μm Hg$_{0.8}$Cd$_{0.2}$Te diode doped symmetrically at 1×10^{19} cm^{-3}, assuming $W^* = W^*_{\mathrm{opt}} = 12.5$. The internal temperature minimum occurs at the junction.
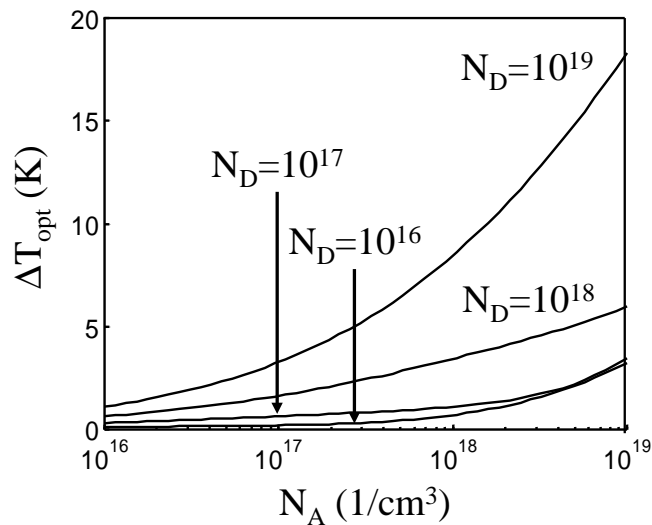
Figure 2-20: Optimal temperature for a Hg$_{0.8}$Cd$_{0.2}$Te diode with $W_p = W_n = 1\mu$m.
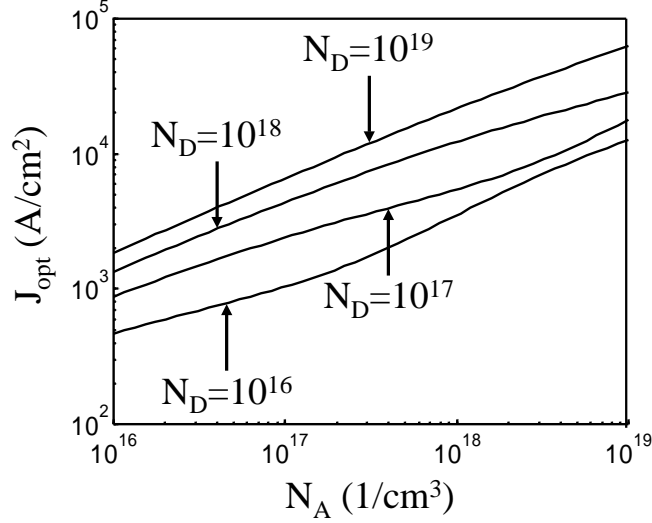
Figure 2-21: Optimal current density for a $Hg_{0.8}Cd_{0.2}Te$ diode with $W_p = W_n = 1\mu m$.

effect.

The total amount of power dissipated in the conventional Peltier cooler is equal to $(JA)^2R$, while the diode dissipates $(JA)^2R + JAV_j$. The extra power dissipated in the diode is used to transport heat from the junction to the contacts (where it is often more readily conducted away), producing the thermal gradients discussed above. In the case for which carriers recombine optically, the total power dissipated can be less than $(JA)^2R$, and an analysis similar to that given in Section 2.5.2 can be applied.

Regarding the self-consistency of the above model, it is apparent from Equations 2.9 and 2.7 that a decreased junction temperature due to thermoelectric cooling leads to changes in both the built-in voltage and the junction bias voltage. This in turn affects the thermoelectric cooling because of the Peltier term's dependence on $V_{bi} - V_j$ (see Equation 2.11b). It can be shown by simple manipulation of the diode I-V relationship that a diode operating at temperature T, upon experiencing a junction temperature change of ΔT at constant current, will have its $V_{bi} - V_j$ changed by a factor of $\frac{T+\Delta T}{T}$. The thermoelectric cooling is therefore perturbed by the same factor: $Q_j = \frac{T+\Delta T}{T}Q_{j0}$. For typical operating conditions ($T \approx 300K$), a change ΔT even as large as -10K will only decrease the thermoelectric cooling by 3%; the analysis of this chapter is therefore assumed to approximate self-consistent behavior.

The dimensionless figure of merit ZT is defined through Equation 2.22 and is given by $\frac{2\Delta T_{\text{opt}}}{T}$. The ZT of most commercial Peltier coolers using bismuth telluride is approximately 1, while the value for a $Hg_{0.8}Cd_{0.2}Te$ diode doped symmetrically at 1×10^{19} cm^{-3} is approximately 0.2. It is interesting to note that this figure is approximately the same as the bulk ZT derived elsewhere [59], implying that bipolar thermoelectric effects, although non-linear and dependent on coefficients that change with voltage, could be ultimately limited by the conventional thermoelectric bulk figure of merit. Based on the analytic expressions for bulk and diode thermoelectric figure of merit, no direct relation between them can be easily seen. This is especially the case since the optimum doping is different for the two cases. The fact that the numerical values of these figures of merit are similar (at the highest dopings that can be easily achieved for a diode) needs further investigation. While the diode is not appropriate as an external cooler, the internal temperature difference that it can sustain is significant. For a device in which external cooling is unsuitable, the internal cooling mechanism of the diode (and of bipolar devices in general) can be optimized.

2.7 Heterojunction Diode and Non-Equilibrium Effects

In order to apply internal thermoelectric cooling concepts to modern active devices, the model presented above must be extended to heterostructures. While the carrier energy difference across a homojunction diode is caused only by the built-in field which opposes diffusion, a heterostructure device has extra energy differences due to potential barriers at interfaces between different materials. In analyzing the thermoelectric properties of a complicated device such as a semiconductor laser diode that has several heterojunctions, it is more practical to derive thermoelectric quantities from transport simulation rather than from analytic expressions.

Here we demonstrate this technique with a simple heterojunction diode and return later (in Chapter 4) to apply this technique in the thermoelectric optimization of a
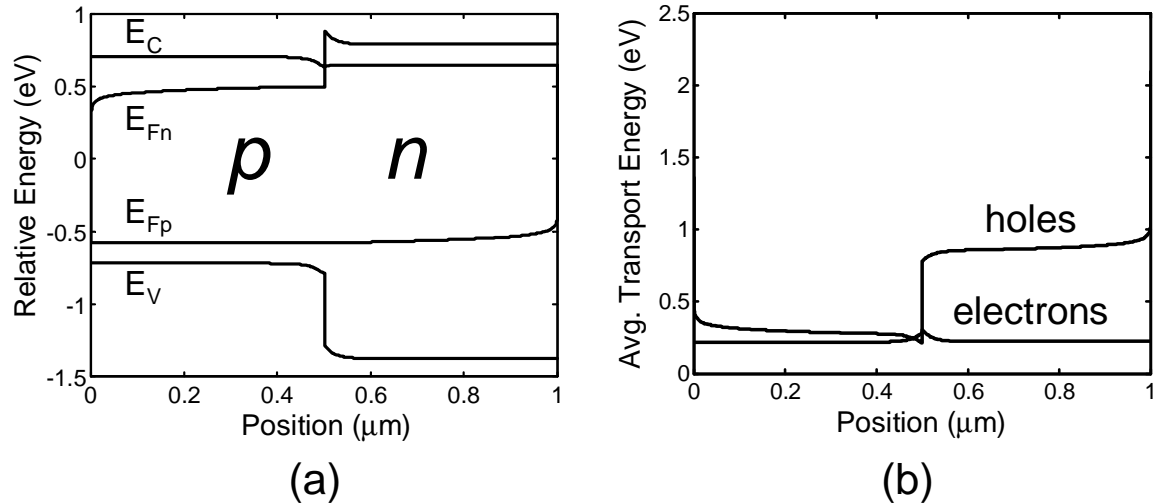
Figure 2-22: GaAs/AlAs heterojunction diode: band structure (a) and average transport energy (b) at 1.25V

more complicated device. Figure 2-22 shows a biased GaAs/AlAs diode doped symmetrically, with the donor concentration N_D and the acceptor concentration N_A both equal to 5×10^{16}, calculated by solving the drift-diffusion equations self-consistently with Poisson's equation [58]. The average transport energy $\overline{E_{tr}} = \Pi * q$ stays roughly constant within each region for each type of carrier, and we average this value over the thickness of each region as before in the homojunction case. We can now determine the junction heat exchange density Q in terms of the Peltier coefficients Π and current densities J as before according to $Q = \Delta\Pi_e * J_e + \Delta\Pi_h * J_h$ [60].

In the case of the homojunction diode, a built-in potential exists for all typical bias ranges, and therefore the junction thermoelectric terms always cause cooling. For the heterojunction diode, however, band offsets cause an additional potential to develop at the junction. If the sign of this band offset potential is such that it opposes the built-in diode potential, at high biases it can overcome the built-in potential and cause net thermoelectric heating at the junction. Heat exchange can therefore be either positive or negative depending on the bias point, as shown in Figure 2-23.

The case of the heterojunction diode also brings to light the issue of hot-carrier effects: in regions of large electric field or high current density, carriers can be out of equilibrium with the lattice. The strength of the coupling between the electron
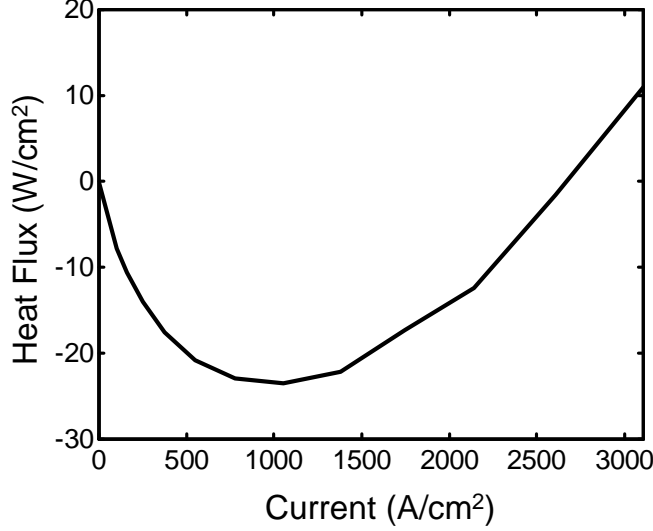
Figure 2-23: Bias dependence of the thermoelectric heat exchange at a diode hetero-junction: both cooling and heating can be achieved depending on the bias point.

and phonon systems sets the difference between the electron temperature T_e and the lattice temperature T_l and also governs the length scale over which these temperatures differ.

Under steady-state conditions, the energy balance equation derived from the one-dimensional Boltzmann Transport Equation using the displaced Maxwellian approximation leads to the following coupled equations for electron and lattice temperatures [28]:

$$-K_e \frac{\mathrm{d}^2 T_e}{\mathrm{d}x^2} + G(T_e - T_l) = JE - Q_{\mathrm{TE}} \tag{2.33a}$$

$$-K_l \frac{\mathrm{d}^2 T_l}{\mathrm{d}x^2} + G(T_l - T_e) = 0 \tag{2.33b}$$

where K_e and K_l are the electron and lattice thermal conductivities respectively, G is a coupling term for energy transfer between electrons and phonons, Q_{TE} is a thermoelectric cooling term, and E is an accelerating electric field acting on electron current J.

In heavily-doped diodes for which the built-in potential is large and thermoelectric cooling is important, the majority of the applied bias is applied over a narrow region at the junction; we therefore approximate $E \approx 0$ and $Q_{\mathrm{TE}} = J(V_{bi} - V)\delta(x - x_j)$ where

64

x_j is the junction location and $V_{bi} - V$ is the diode potential barrier. An expression for G is given by [28]:

$$G = \frac{3nk_B}{2\tau_e} \tag{2.34}$$

where n is the electron concentration and τ_e is the energy relaxation time.

The solution to Equations 2.33 is dependent on imposed boundary conditions, but by assuming that the solutions of T_e and T_l are of the form $e^{-x/\lambda}$, we can derive an approximate length scale λ over which electrons and phonons are expected to be out of equilibrium [61]:

$$\frac{1}{\lambda^2} \approx G \frac{K_e + K_l}{K_e K_l} \tag{2.35}$$

For a typical InGaAs diode at a high current density ($J \approx 10^6$ A/cm^2), we approximate $n \approx 10^{19}$cm^{-3}, $K_l \approx 5$ W/mK, $K_e \approx 0.5$ W/mK, $\tau_e \approx 1$ps [62, 63, 64]. This yields $G \approx 2 \times 10^8$ W/cm^{3}K and $\lambda = 400$nm, implying that electron and lattice temperatures will in the worst case equilibrate only 400nm from the junction. The complete transfer of heat from the lattice to the carriers is thus expected to occur in close proximity to the junction, verifying the thermal model presented in Section 2.6.2. Further reduction of this relaxation length is expected from electron-hole scattering, which can be of the same order as electron-phonon scattering [65, 66]. In modeling thermoelectric effects in semiconductor laser heterostructures, G will remain roughly the same but the current density J (and hence Q_{TE}) will typically be much smaller. This will reduce the source term in Equations 2.33 and further validate the assumption that the carriers and lattice are in equilibrium a short distance from a heterointerface.

2.8 Conclusion

The bipolar Peltier coefficient can be used to model thermoelectric heat exchange as a function of device bias in minority-carrier devices. Analytic expressions have been derived which yield optimal bias conditions for thermoelectric cooling; several material systems show the capability for large internal temperature gradients. Internal

thermoelectric cooling has many implications for device designs in which heat management is important and for which external cooling is not desirable or not effective.

Because of the high thermal conductivities of traditional semiconductors such as silicon and gallium arsenide, internal thermoelectric effects are not large in devices made from these materials, although they have been reported in simulations of heterojunction bipolar transistors (shown in Figure 1-11) [6, 67]. New device materials such as III-V quaternary compounds are likely to have larger internal temperature gradients due to their low thermal conductivity.

The mechanism of internal thermoelectric cooling is especially relevant to semiconductor laser diodes, whose performance is strongly dependent on junction temperature. Since most lasers employ complicated heterostructures for the confinement of carriers and the optical mode, numerical transport simulations must be performed in order to model their internal thermoelectric effects. In order to test the validity of these simulations as well as other models for heat exchange, the next chapter will present experimental work related to the electrical and thermal modeling of semiconductor laser diodes.

Chapter 3

Internal and External Heat Exchange in Semiconductor Lasers

In order to apply the idea of internal thermoelectric cooling to the design of a bipolar device, we must first have an understanding of the other heat exchange mechanisms which work in concert with thermoelectric effects to set the temperature profile of the device. They include both the internal production and flow of heat and the external heat transfer mechanisms that govern the exchange of energy between the device and its environment.

3.1 Semiconductor Laser Diode

The device that we will investigate here is the semiconductor laser diode (see Figure 3-1). Much like the diodes discussed in Chapter 2, a laser diode relies on bipolar transport from p-type and n-type layers. However, in a laser diode these layers are not directly joined but rather are separated by an intrinsic region that provides confinement for both recombining carriers and emitted photons. A common design that accomplishes this is the *separate confinement heterostructure*, in which the intrinsic region is made up of two different alloys: a narrow center active region ("quantum well") that traps electrons and holes so that they overlap and recombine to emit light, and a separate region ("waveguide core") that provides a relatively high refractive
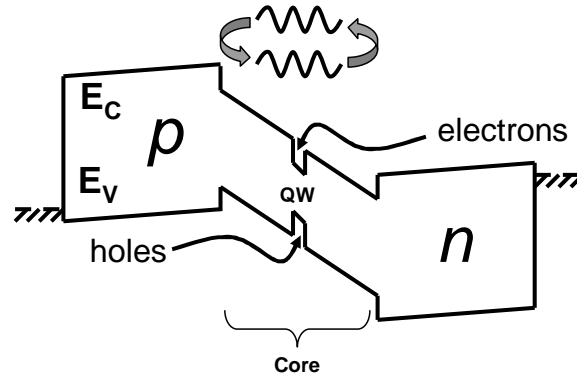
Figure 3-1: Carrier transport in a separate confinement heterostructure semiconductor laser diode.

index to confine the emitted light. Photons emitted by optical recombination in the quantum well are reflected both at the interfaces between the core and the n-type and p-type "cladding" layers and at the core/air facets; the reflected light then stimulates the further optical recombination of carriers in the quantum well. As the laser is biased up to a certain point known as *threshold*, this positive feedback leads to a sudden large increase in the stimulated emission of light. Below threshold, the light output is small and governed by spontaneous emission, while above threshold a significant fraction of the device's input power is emitted as monochromatic light.

Several effects can lead to severe heating in diode lasers. In addition to Joule heating due to current flow through resistive layers, lasers are plagued by processes such as radiation absorption and non-radiative recombination (through which carriers emit heat rather than light). Increased temperature leads to a larger spread in energy of the carrier distribution in the active region, consequently decreasing device efficiency due to both increased leakage of carriers out of the quantum well and decreased carrier density at the lasing optical transition. In addition, higher operating temperature can cause the wavelength of the output light to drift and can decrease device lifetime (see Figure 3-2) [7, 8, 9]. In extreme cases, strong absorption at a laser's output facet can cause a thermal runaway effect which ends in the catastrophic failure and melting of the device.

Thermal management is thus a critical issue in the performance of semiconductor
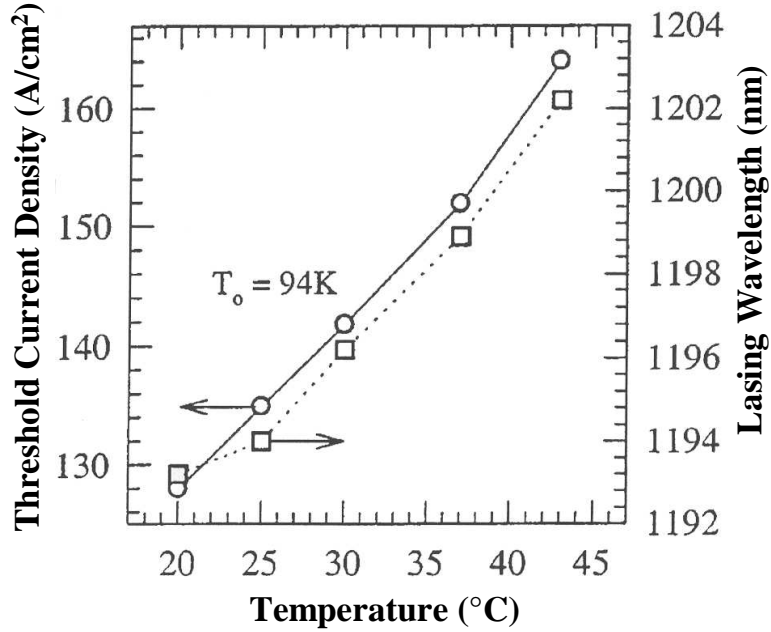
Figure 3-2: Threshold current density and lasing wavelength versus operating temperature for $\lambda = 1.2\mu$m InGaAs laser [4].

laser diodes. While internal heating sources such as non-radiative recombination, Joule heating, and contact heating have been studied extensively [68, 69], external heat exchange models that describe the transport of energy to and from a device have focused primarily on the mechanism of thermal conduction [69]. Analysis of convective effects has been very limited [70]. In this chapter, we will first develop new models for external heat exchange in a laser diode and then later return to a description of internal transport.

3.2 External Heat Exchange

By measuring the total energy flow from an optical device, we can arrive at new design strategies for thermal stabilization. Here we develop a comprehensive model for heat exchange between a semiconductor laser diode and its environment that includes the mechanisms of conduction, convection, and radiation. We perform quantitative measurements of these processes for several devices, deriving parameters such as a laser's heat transfer coefficient, and then demonstrate the feasibility of thermal
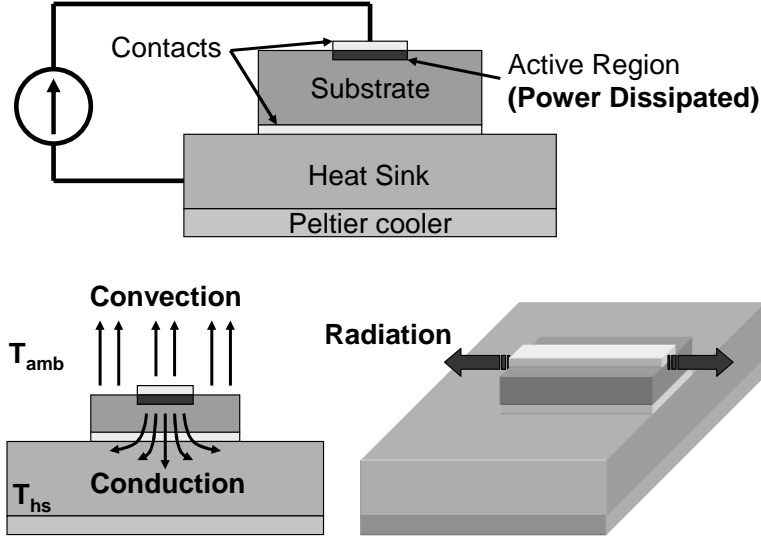
Figure 3-3: The power dissipated through heat in the active region of a semiconductor laser diode is removed by the mechanisms of convection, conduction, and radiation.

probing for the nondestructive wafer-scale characterization of optical devices.

3.2.1 Heat Transfer Processes

There are three mechanisms by which a device can exchange heat energy with its environment: conduction, convection, and radiation [71]. These processes are illustrated in Figure 3-3 for a laser diode.

Conduction occurs across a temperature gradient through atomic vibrations and collisions in which no translational motion of the individual particles takes place; it is thus typical of solids. The heat equation that governs steady-state thermal conduction in a region with thermal conductivity k is given by $\nabla \cdot k \nabla T = -q$ where q is the power generated per unit volume. For quasi-one-dimensional heat flow in a source-free region, the temperature difference ΔT between a boundary heat source and a point within the region can be approximated using a thermal impedance model as $\Delta T = Z_T P_{\mathrm{cond}}$ where Z_T is a geometry-dependent impedance and P_{cond} is the power generated by the source [69]. In this approximation, the temperature dependence of the thermal conductivity is also neglected. For example, heat conduction in one dimension can be described by the thermal impedance $Z_T^{1D} = \frac{L}{kA}$ where L and A are

(respectively) the thickness and area of the region across which ΔT is maintained.

Convection occurs across a temperature gradient in which heat energy is transferred by the translational motion of individual particles; it is thus typical of fluids. The heat transferred by convection from a planar source surface of area A and temperature T_{surf} to a surrounding fluid at temperature T_{amb} is given by $P_{\mathrm{conv}} = hA(T_{\mathrm{surf}} - T_{\mathrm{amb}})$ where the heat transfer coefficient h depends on parameters such as the fluid's velocity and specific heat and the nature of the fluid/surface contact. While conduction and radiation are the primary mechanisms of heat transfer near the surface, where the fluid is stationary, it is common practice to lump the total heat transfer from a surface to a moving fluid into the convection model.

Radiation occurs when charged carriers transmit energy in the form of electromagnetic waves; this energy can be acquired by the carriers thermally (as in blackbody radiation) or through electrical pumping (as in optoelectronic devices). For typical device temperatures, the blackbody term is small, but for optical devices such as laser diodes the radiated power due to electrical pumping can be significant.

3.2.2 Balance of Terms for a Laser

In the steady state, the power generated by a device is balanced by the power removed from the device, and we can write

$$P_{\mathrm{diss}} = P_{\mathrm{cond}} + P_{\mathrm{conv}} + P_{\mathrm{rad}} \tag{3.1}$$

where the mathematical dependencies of these terms are illustrated for a laser diode in Figure 3-4. The radiated power below and above threshold can be written as

$$P_{\mathrm{rad}} = \begin{cases} \eta_{\mathrm{LED}} I & (I < I_{\mathrm{th}}) \\ \eta_{\mathrm{LED}} I_{\mathrm{th}} + \eta_{\mathrm{d}}(I - I_{\mathrm{th}}) & (I \geq I_{\mathrm{th}}) \end{cases} \tag{3.2}$$

where the differential efficiencies η_{LED} and η_{d} are device-dependent and represent the fraction of recombining carriers that contribute to (respectively) spontaneous and
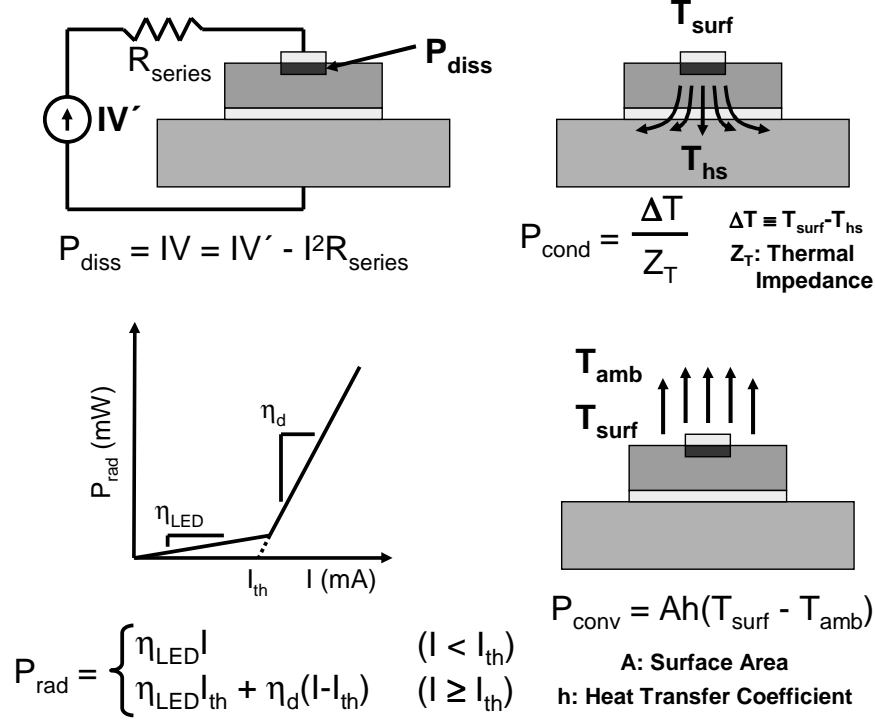
Figure 3-4: Mathematical relationships for heat exchange mechanisms.

stimulated emission.

For a semiconductor laser diode structure composed of a thin active region in contact with a thick substrate that also contacts a heat sink, we consider the typical case in which recombination and absorption are restricted to the vicinity of the active region and Joule heating in the substrate is small. Under these conditions, the bias power IV that is injected at the contacts (accounting for series resistance in the wires of the source) is almost completely dissipated near the active region [72]. We can write the heat exchange balance for the laser diode, accounting for conduction through the substrate, convection from the top surface, and radiation from the active region, as

$$IV = \frac{\Delta T}{Z_T} + A_{\text{eff}} h (T_{\text{surf}} - T_{\text{amb}}) + P_{\text{rad}} \tag{3.3}$$

where $\Delta T = T_{\text{surf}} - T_{\text{hs}}$ is measured between the top surface electrical contact and the heat sink [73]. Due to lateral heat spreading, the area A_{eff} over which convection occurs is larger than the top contact area; however, we assume that it is small enough

that air flow remains laminar and convection is proportional to $T_{\text{surf}} - T_{\text{amb}}$ (as with the thermal impedance model). In our model, as well as in our experimental setup, we use free convection (i.e. no forced air motion) and ignore the small dependence of h on temperature [71]. Simple two-dimensional finite-element simulations that maintain constant heatsink and ambient temperatures confirm that total convected power remains proportional to surface temperature at different heat source magnitudes and therefore that A_{eff} does not vary with injected power in this approximation.

At zero bias ($I = 0$), convected and conducted power balance, and Equation 3.3 can be solved to give

$$A_{\text{eff}}h = \frac{\Delta T_0}{Z_T(T_{\text{amb}} - T_{\text{surf}})_0} \tag{3.4}$$

Below threshold, assuming a low level of spontaneous emission, we can now write

$$Z_T IV = \Delta T - \Delta T_0 \frac{T_{\text{surf}} - T_{\text{amb}}}{(T_{\text{surf}} - T_{\text{amb}})_0} \tag{3.5}$$

and determine Z_T through thermal measurement below threshold.

3.2.3 Experimental Determination of Heat Flow

To quantify heat exchange in actual devices, we examine two semiconductor laser diodes: a ridge-waveguide InP-based device that has a small top contact area and an oxide-stripe GaAs-based device that has a large contact area. We begin with the former, a $15 \times 500\mu\text{m}^2$ 5-QW InGaAsP/InP laser emitting at $\lambda = 1.55\mu\text{m}$ that sits atop a $100\mu\text{m}$-thick InP substrate that is mounted on a large ($4 \times 3 \times 0.4$ cm^3) gold-plated copper block heatsink. The copper block is cooled from below by an external Peltier cooler, and a thermistor at temperature T_{therm} located approximately 5 mm from the laser is used for heatsink temperature feedback control. To perform temperature measurements, we use $25 \times 25\mu\text{m}^2$ NIST-traceable microthermocouples that have an accuracy of 200 mK and a resolution of 10 mK [74, 75]. As illustrated in Figure 3-5, surface temperature T_{surf} is taken directly on the top surface contact, and heatsink temperature T_{hs} is measured on the heatsink approximately 50 μm from the
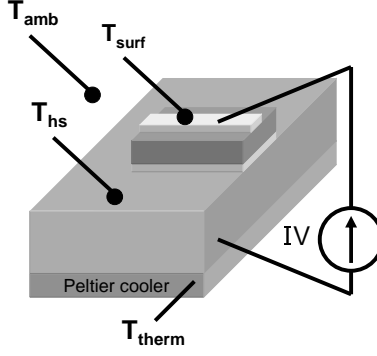
Figure 3-5: Microthermocouple measurement setup.

substrate and just outside of the light path. Ambient temperature T_{amb} is measured several millimeters above the laser, and convection is natural (i.e. not forced). During the course of a measurement, surface temperature is determined at several locations and averaged, showing the variation across the surface to be less than 200mK.

Figure 3-6 shows experimental data for this laser structure. We measure a series resistance of 0.9 Ω in the wires of the IV' power source and take this into account by setting $IV = IV' - I^2 R_{\text{series}}$. Although the thermistor is maintained at 17 °C, the large-area cooler is unable to effectively control the heat sink temperature near the laser. In Figure 3-7, we see that ΔT exhibits a kink at threshold due to the sudden increase in radiated power. By plotting the right side of Equation 3.5 versus IV and fitting the slope below threshold as shown in Figure 3-8, we determine Z_T to be 19.6 K/W. This value is close to previously reported values for geometrically similar InP-based laser diodes that were measured by different methods or predicted theoretically [72, 76, 77]. Small discrepancies may be due to thermal gradients in the heat sink (as shown in Figure 3-6) which lead to a non-isothermal boundary condition. Using Equation 3.4, we measure $A_{\text{eff}}h$ to be $1.8{\times}10^{-3}$ W/K. Although A_{eff} is unknown, an estimate that assumes one-dimensional heat flow ($Z_T \approx Z_T^{\text{1D}}, k = 68$ W/mK) yields $A_{\text{eff}} \approx 150 \times 500\mu\text{m}^2$ and $h \approx 2.4 \times 10^4$ W/m^{2}K, the latter of which is comparable to reported experimental values for micron-scale semiconductor devices [78].

Given the measured temperature variation between the laser and the ambient air, we can characterize the process of natural convection by the Rayleigh number, given
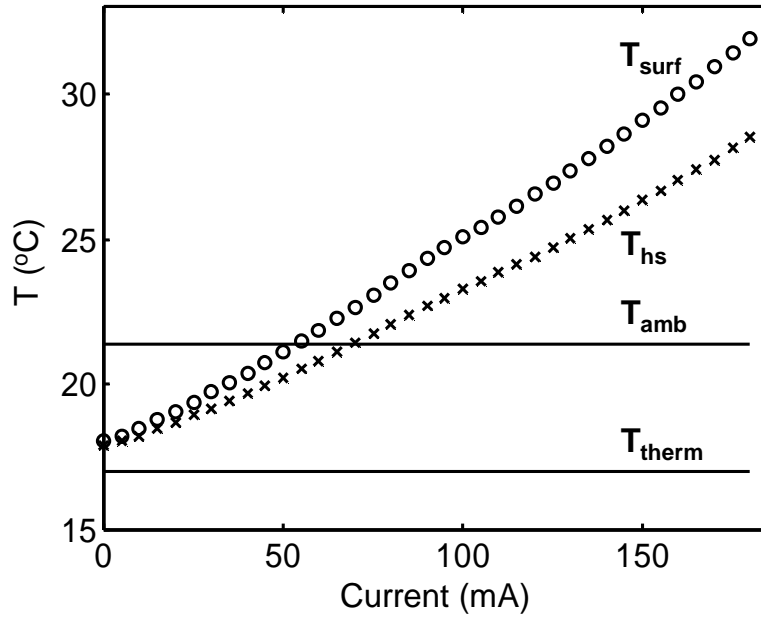
Figure 3-6: Measured temperatures of InGaAsP/InP laser surface, heatsink, and ambient air. Thermistor set temperature is also shown.
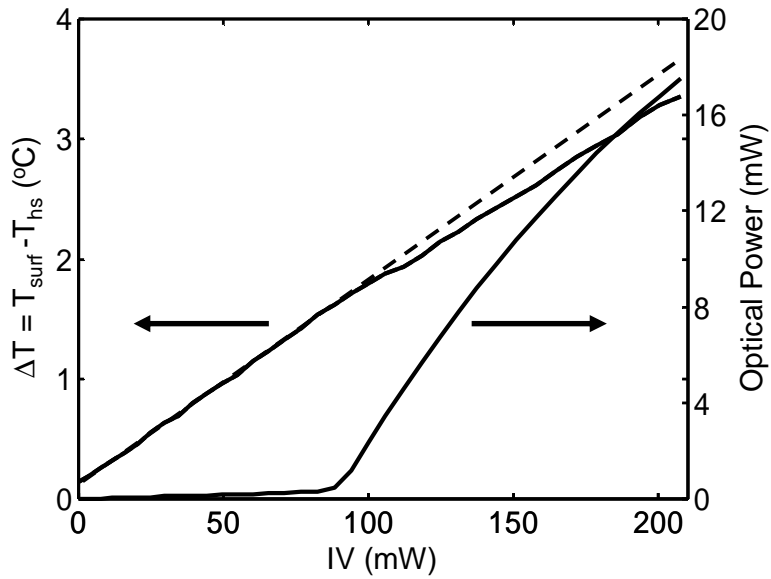
Figure 3-7: Measured ΔT and optical power; each has a kink at threshold.
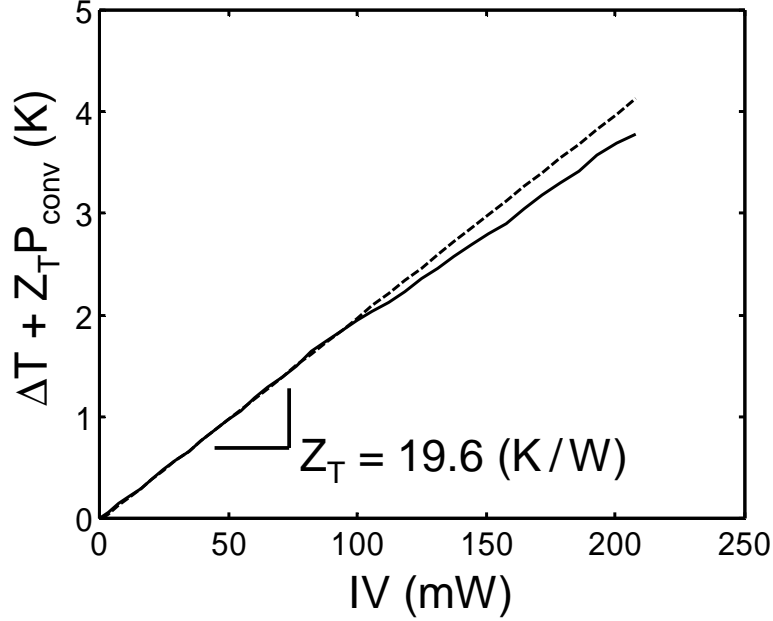
Figure 3-8: Z_T determined experimentally by linearly fitting the right side of Equation 3.5 to the input power IV.

by [71]

$$\text{Ra} = \frac{\beta \Delta T g L^3}{\nu^2} \text{Pr} \tag{3.6}$$

For convection into air at 300K, the expansion coefficient $\beta \approx 1/300$ K^{-1}, the surface-to-ambient temperature difference $\Delta T \approx 10$ K, the gravitational acceleration $g \approx 9.8$ m/s^2, the length $L \approx 500$ μm, the kinematic viscosity $\nu = 15.66 \times 10^{-6}$ m^2/s, and the Prandtl number Pr $= 0.69$. This yields Ra ≈ 0.1; since convective flow does not become turbulent in the case of a heated horizontal area facing up for Ra $< 10^7$, we conclude that the convection pattern remains laminar [71].

Given that the flow remains laminar, we do not expect a sudden change in the heat transfer coefficient that would take place upon a transition to turbulent flow. We likewise recognize that the heat transfer coefficient computed here is a quantity which is averaged over the effective area of convection, i.e.

$$h = \frac{1}{A_{\text{eff}}} \int_0^{A_{\text{eff}}} \tilde{h}(x, y) \, dA_{\text{eff}} \tag{3.7}$$
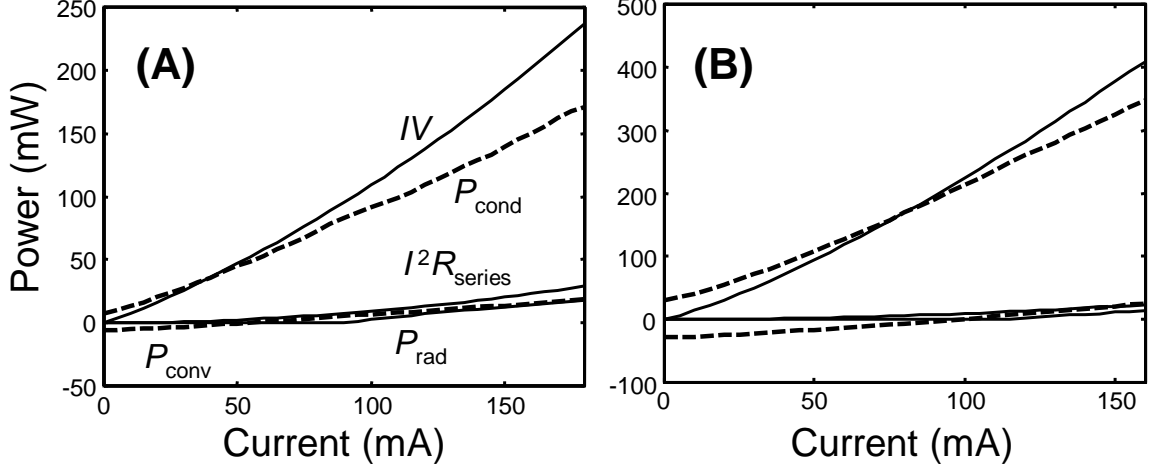
Figure 3-9: Heat exchange terms as derived through thermal probing for devices at (A) $\lambda = 1.55\mu$m and (B) $\lambda = 980$nm. Conduction and convection terms are shown as dotted lines; P_{rad} is measured using an optical power meter.

Since the slope-fit Z_T implicitly takes into account conduction from an area A_{eff} that increases with bias, the lumped value of $A_{\mathrm{eff}}h$ calculated by Equation 3.4 mirrors this dependence in its conduction to a laminar fluid. As the device heats up and the effective area increases, we expect $A_{\mathrm{eff}}h$ to remain roughly constant.

Having determined quantitatively the parameters for heat exchange, we can plot the contributions of the various mechanisms at different bias levels, as shown in Figure 3-9 [79]. While conduction is the dominant term, the convected power is the same order of magnitude as the radiated power. Also shown are results for a $30 \times 500\mu$m^2 oxide-stripe InGaP/InGaAs/GaAs device operating at $\lambda = 980$nm that has a top contact size of $100\times 500\mu$m^2 and a GaAs substrate thickness of 100μm. The same setup is used in both cases, and $R_{\mathrm{series}} = 0.9\Omega$ as before. For the GaAs device, we measure $Z_T = 16.3$ K/W and $A_{\mathrm{eff}}h = 8.4 \times 10^{-3}$ W/K. The smaller Z_T and larger $A_{\mathrm{eff}}h$ with respect to the InP device are most likely due to heat conduction into the large metal contact; the InP contact is only $15 \times 500\mu$m^2 and is connected to a side contact pad. Estimating $Z_T \approx Z_T^{1D}$ as before, we find that $A_{\mathrm{eff}} \approx 225 \times 500\mu$m^2 and $h \approx 7.5\times 10^4$ W/m^{2}K for the GaAs ($k = 55$ W/mK) device. The larger effective area is consistent with the larger contact size, and the greater heat transfer coefficient is
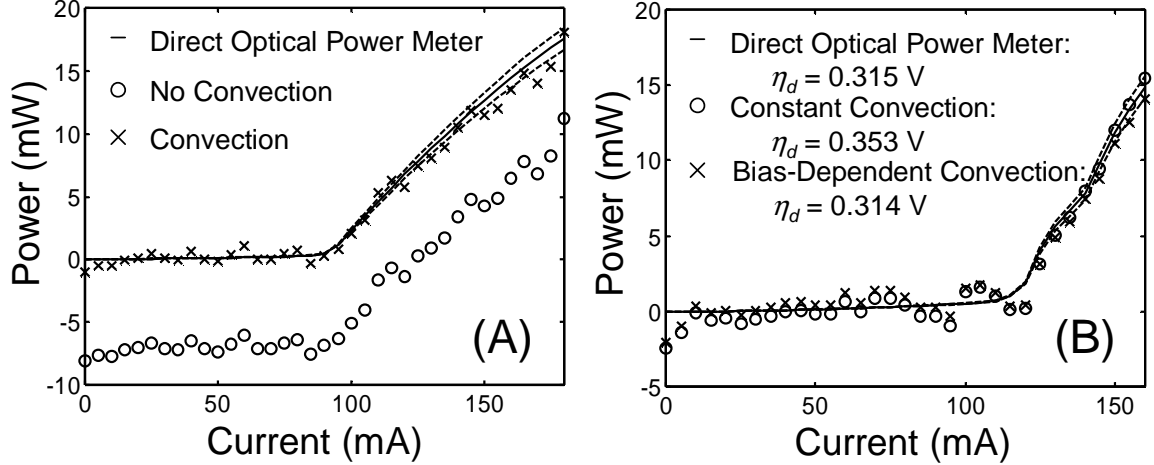
Figure 3-10: Optical power as directly measured by a detector and as derived through thermal probing (dotted lines: $\pm 5\%$) for devices at (A) $\lambda = 1.55\mu$m and (B) $\lambda = 980$nm. The elimination of convection from the thermal model causes the error in output power shown as well as a substantial error in Z_T.

most likely due to a more even temperature profile across the broad, high thermal conductivity contact, or possibly due to a greater surface roughness in the metal leading to more nucleation sites for droplet condensation [71].

In order to verify the accuracy of the experimental data, we plot $IV - P_{\mathrm{cond}} - P_{\mathrm{conv}}$ (see Equation 3.1) and compare it to measurements taken directly using an optical power meter. As shown in Figure 3-10, the technique of thermal probing can be used to accurately measure the optical power output of the laser diodes. In Figure 3-10A we model the InP laser both with and without convection included in the thermal model. In the zero-convection case, Equation 3.5 becomes $Z_T IV = \Delta T$; the heat balance of Equation 3.1 requires that heat conduction must rise accordingly, and Z_T is reduced to 17.1 K/W. Disregarding convection entirely thus results in an error for Z_T of 13%.

Since $A_{\mathrm{eff}}h$ is small for the InP laser, the zero-bias power convected into the device is likewise small (~ 6 mW), and P_{conv} is approximately proportional to IV. For this reason, the convection and zero-convection models differ by only a constant 6 mW (although their values of Z_T are different). In the case of the GaAs laser, however, the zero-bias power convected into the device is larger (29 mW), and a simple reduction

in Z_T does not capture the bias dependence of the convection term. In Figure 3-10B we model the GaAs laser with the convection term as well as with a zero-convection model. As before, the elimination of convection from the model reduces Z_T to 14.0 (an error of 14%), but now there is an additional bias-dependent error. This can be demonstrated by calculating the laser's differential efficiency above threshold η_d. By including the bias dependence of the convection term, the error in η_d is reduced from 12% to a negligible amount. The differential quantum efficiency $\eta_d \frac{q}{h\nu}$ changes from 27.9% to the directly measured value of 24.8%. It is worth noting that the largest error reduction is at high bias values. For the InP laser, the error in η_d is 5%. A reason for the abrupt smoothing of the temperature fluctuations above threshold (and smaller error) in the GaAs device is not immediately obvious.

3.2.4 Further Uses

This technique shows promise as a means for the nondestructive wafer-scale testing of photonic integrated circuits for which detectors are unavailable or are unable to be placed in the light path, such as the case of a laser that is laterally coupled into a waveguide electroabsorption modulator [80]. A similar method has been proposed recently which makes use of thermoreflectance microscopy of a laser's facet [81]. While this method utilizes the same general technique of relating device temperature to optical output, it is not applicable to wafer-scale testing. The advantage of the technique proposed here is that a simple setup may be used in a nondestructive way (that does not require calibration) on many different devices during normal operation. The location of lasing threshold is easily determined through temperature measurements, and light output power can be calculated to within a few percent. No prior knowledge of material parameters, geometry, or even light wavelength is necessary. All parameters are obtained experimentally; a careful measurement of the derivative above threshold (where many internal processes have clamped) could yield even better accuracy. This method also shows promise for the determination of other laser parameters such as η_{LED} and for application to other devices such as optical amplifiers [82, 83].

By using microthermocouple probes and carefully accounting for all heat pathways, we have experimentally quantified heat flow through the pathways of conduction, convection, and radiation in two optical devices, and have determined approximate values of the effective area and the heat transfer coefficient that are used in modeling convection heat exchange. Convection is often a non-negligible effect, and its absence in thermal models can result in errors in the measurement of thermal impedance of approximately 14%. The numerical models that are normally employed to predict parameters such as Z_T and T_0 for a packaged device can likewise suffer errors from the assumption of an isothermal heatsink boundary condition, which we have shown to fail in certain common geometries.

Having developed a model for the exchange of heat energy between a semiconductor laser diode and its environment, we will next examine heat exchange mechanisms that are internal to the laser. By modeling transport processes such as Joule heating and non-radiative recombination, and then confirming these models with electrical and thermal measurements, we will be in a position to later use these models to study the optimization of internal thermoelectric cooling for a laser diode.

3.3 Internal Heat Exchange

In analyzing ideal diode structures in Chapter 2, the short-length approximation was often considered, restricting recombination to the Ohmic contacts. Additionally, these contacts were assumed to be perfect heat sinks, maintaining a given temperature regardless of incident heat flux. While these approximations are useful in that they facilitate the analytic derivation of transport parameters for ideal diodes, they are of limited use in describing more complicated devices such as the semiconductor laser diode (shown in Figure 3-1).

For the case of a laser diode, recombination occurs throughout the device; it is designed to be especially concentrated in the active region. A fraction of this recombination is non-radiative and therefore takes the form of a highly intense quantum well heat source. As demonstrated in Figure 3-6, the contacts are usually not ideal
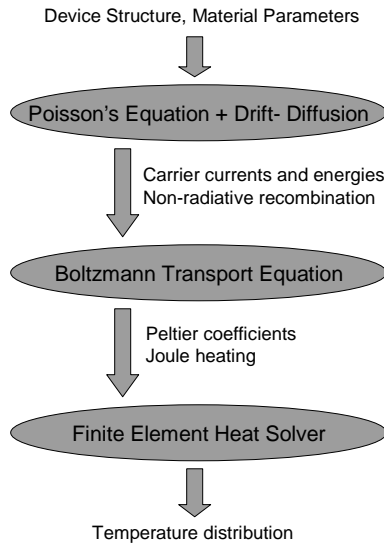
Figure 3-11: Flowchart for electrical and thermal modeling.

and do not maintain a constant temperature. Topside metal/semiconductor contact resistance appears as an additional heat source for the device.

In the discussion of a laser's external heat exchange mechanisms in Section 3.2.2, the majority of the heat generated was assumed to be lumped into a single source, and the entire laser was assumed to operate at a single (surface) temperature. Because laser heterostructures are typically formed from ternary and quaternary alloys that have low thermal conductivity, however, a complicated and highly peaked internal heat source pattern can lead to large variations in internal temperature. The effects of these internal variations were simply lumped into the experimentally-measured thermal impedance above, but we return to them in this section due to the fact that it is a laser's active region temperature, not its surface temperature, that determines its performance. Below, we model the drift-diffusion processes that govern transport inside two different laser diodes, using finite element simulation to relate internal heat exchange to temperature profiles. A flowchart for the model is shown in Figure 3-11.
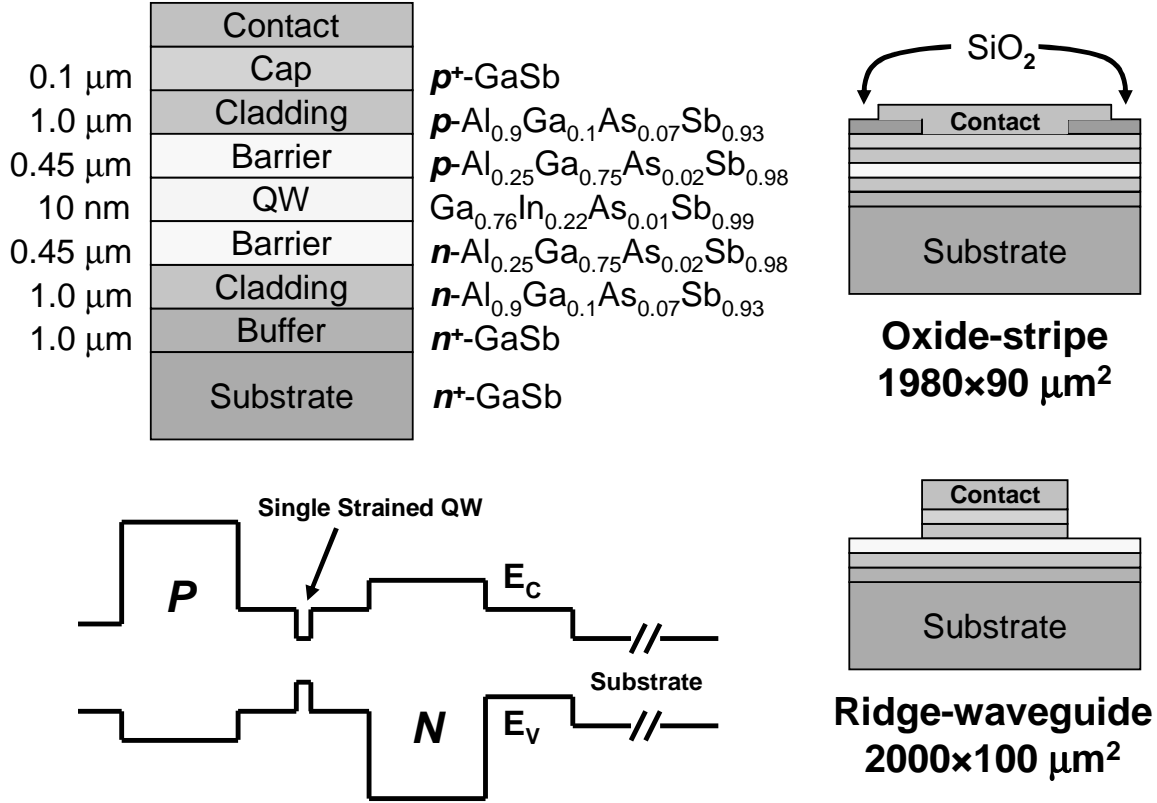
Figure 3-12: Layer structure, band structure, and contact geometries for the oxide-stripe and ridge-waveguide lasers under examination.

3.3.1 Electrical Model

The specific devices to be examined are two strained single-quantum-well lasers, one an oxide-stripe device and the other a ridge-waveguide device, that are grown on GaSb substrates and operate at $\lambda = 2.05\mu$m. The layer structure of each is composed of a $Ga_{0.76}In_{0.22}As_{0.01}Sb_{0.99}$ well, AlGaAsSb core barriers, and cladding layers, as described elsewhere [5]. The top (p-side) contact area is approximately $100 \times 2000\mu$m^2 for both devices. Illustrations of the layer structure, band structure, and contact geometry are provided in Figure 3-12. The threshold current density for the ridge-waveguide laser is significantly lower than that of the oxide-stripe device, as shown in Figure 3-13. Because the cap and p-cladding layers have been etched away on either side of the ridge, current confinement is improved versus the oxide-stripe device. Confinement of the optical mode is also improved due to the lateral index contrast between the
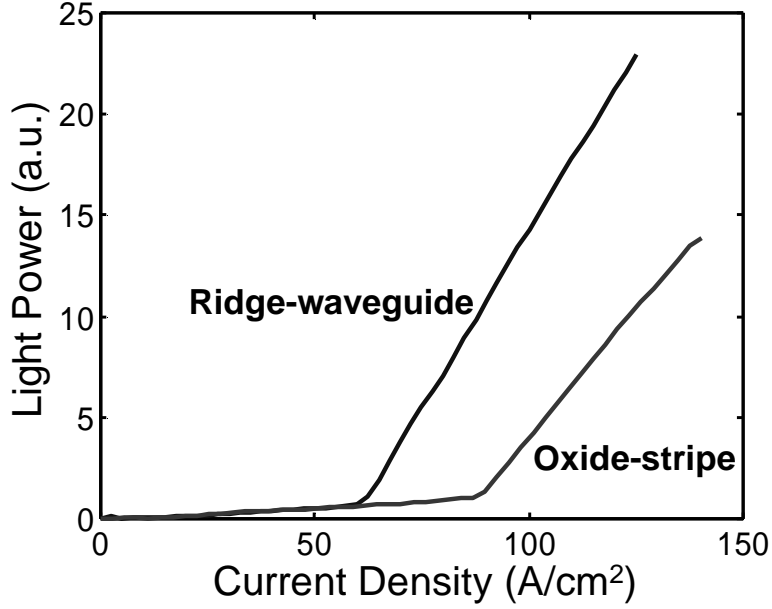
Figure 3-13: Light output curve showing the threshold current density for each laser. Light power was measured by suspending a microthermocouple in the light path and using it as a bolometer.

p-cladding and the air.

In order to model carrier transport within these lasers, we solve the drift-diffusion equations self-consistently with Poisson's equation (as in Section 2.7). Figure 3-14 shows the calculated band structure at a voltage bias of 0.7V. Auger recombination, which is known to be a dominant source of non-radiative recombination in GaInAsSb-based lasers [9], is shown in Figure 3-15. In this process, a recombining electron-hole pair releases energy not through emitting a photon but rather through exciting a second electron high into the conduction band [69]. As the electron thermalizes, a bandgap's worth of energy is deposited in the surrounding lattice. Because the rate of Auger recombination increases sharply with carrier density, a large spike appears at the quantum well, decreasing the laser's efficiency both by providing a non-radiative pathway for recombination as well as by increasing its temperature. The Auger coefficient used for the simulation is 5×10^{-29} cm^{6}s^{-1} [5]; the coefficients used for bimolecular (radiative) recombination and Shockley-Read-Hall recombination are 5×10^{-11} cm^{3}s^{-1} and 10^7 s^{-1} respectively [84].
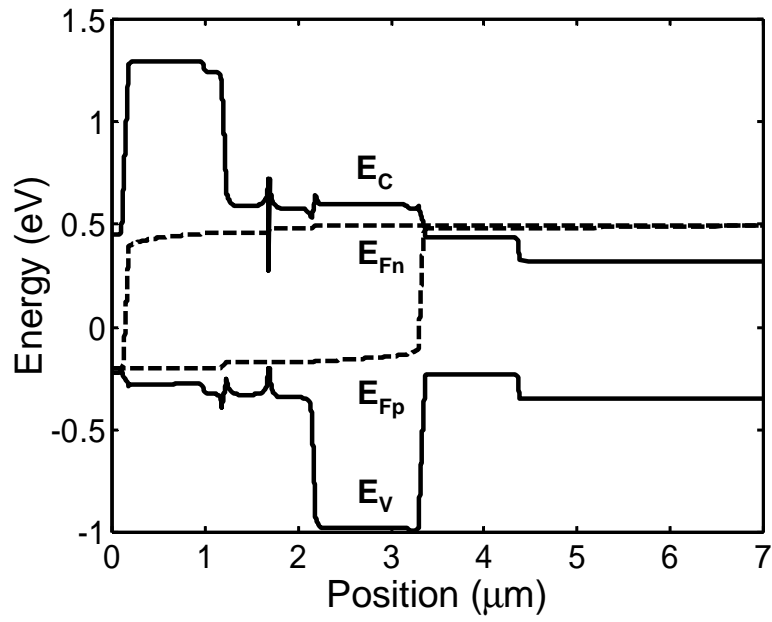
Figure 3-14: Calculated laser band structure at a voltage bias of 0.7V.
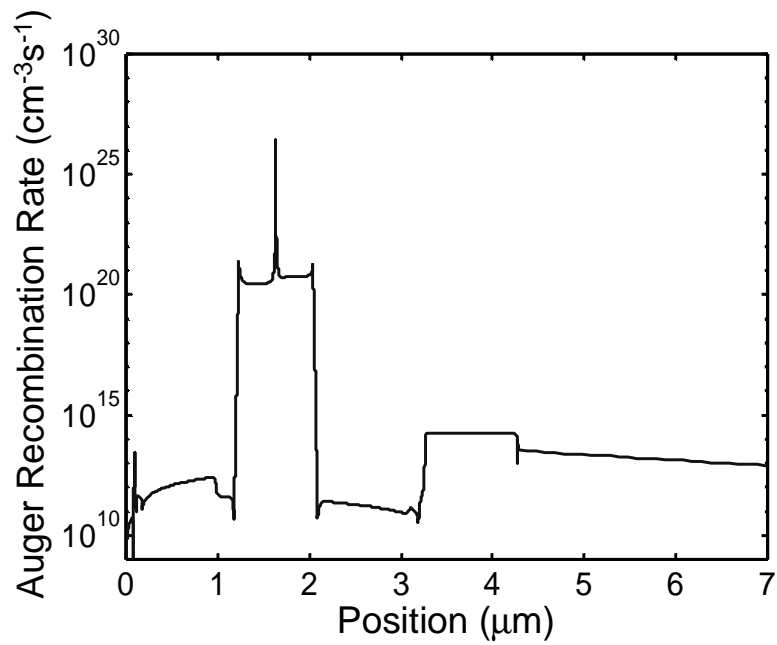
Figure 3-15: Calculated Auger recombination rate at a voltage bias of 0.7V.
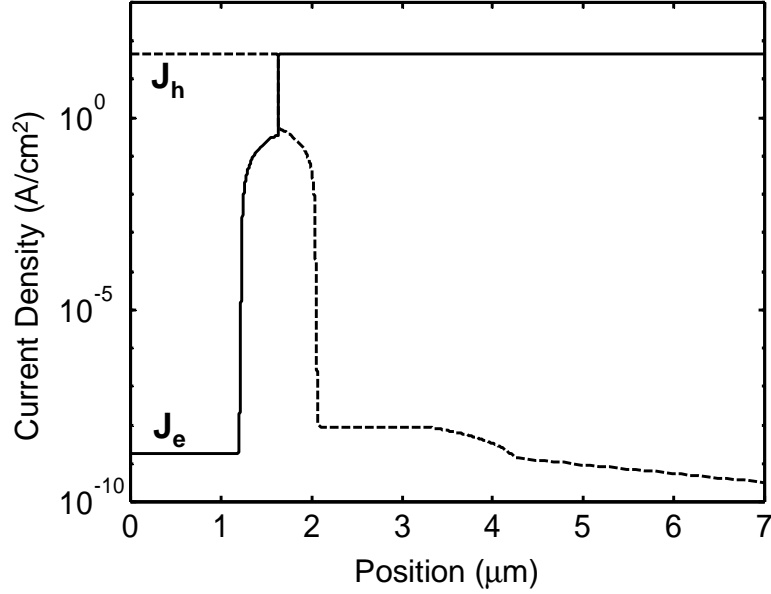
Figure 3-16: Electron and hole current densities at a voltage bias of 0.7V. Nearly all carriers recombine in the quantum well; leakage current is negligible.

In most laser diodes, including those under discussion in this chapter, leakage current out of the core region is minimal due to large blocking (cladding) layers; nearly all carriers injected in forward bias recombine in the active region (see Figure 3-16). If a diode is biased at a voltage V and current I, the power released by this recombination is equal to $I\frac{E_G}{q}$, where E_G is the energy gap at which recombination occurs. Because V and $\frac{E_G}{q}$ are independent of each other (as shown in Figure 3-17), the injected power IV and recombination power are not necessarily equal. In order to complete an internal energy balance model for a diode, the energy gain and loss prior to recombination must be taken into account; this includes Joule heating as well as thermoelectric effects. In Figure 3-18, we see that the electron and hole Peltier coefficients (defined by Equations 1.17 and 1.18) vary throughout the laser diode but stay roughly constant within each material layer. To calculate the thermoelectric heat exchange that takes place as carriers move between the layers of the device, we can average the Peltier coefficient for each carrier type within each layer as in Section 2.7 and then multiply the difference $\Delta\Pi$ on either side of a junction by the current that flows across it. Noting that the Peltier coefficients are bias-dependent (due to their
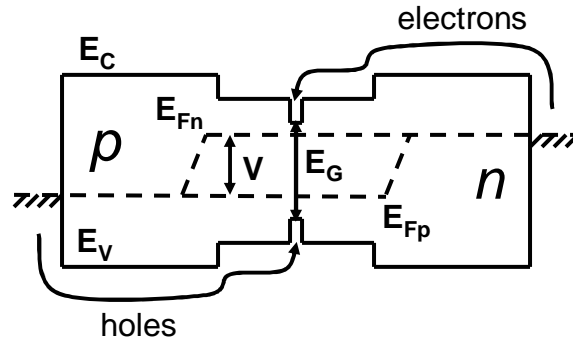
Figure 3-17: The bias voltage V is independent of the voltage $\frac{E_G}{q}$ at which carriers recombine. An energy balance model must account for the variation of carrier energy prior to recombination.
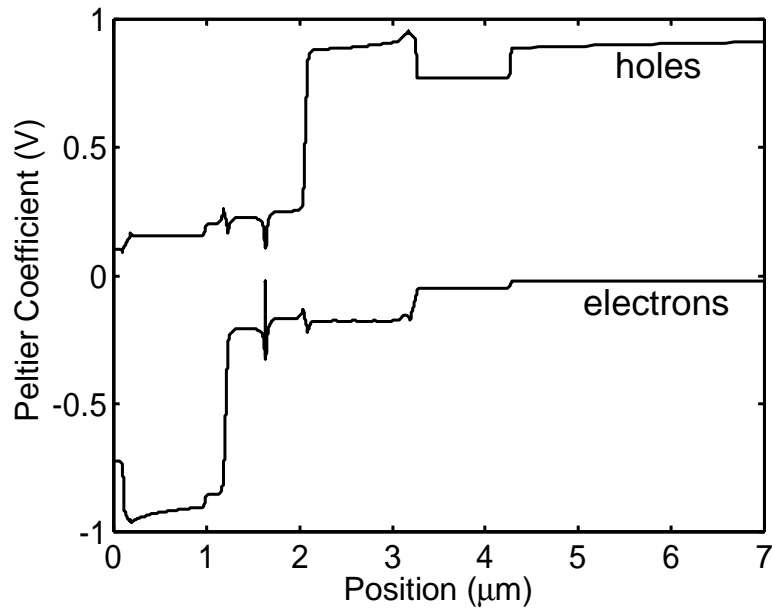
Figure 3-18: Spatial variation of the electron and hole Peltier coefficients at a voltage bias of 0.7V.
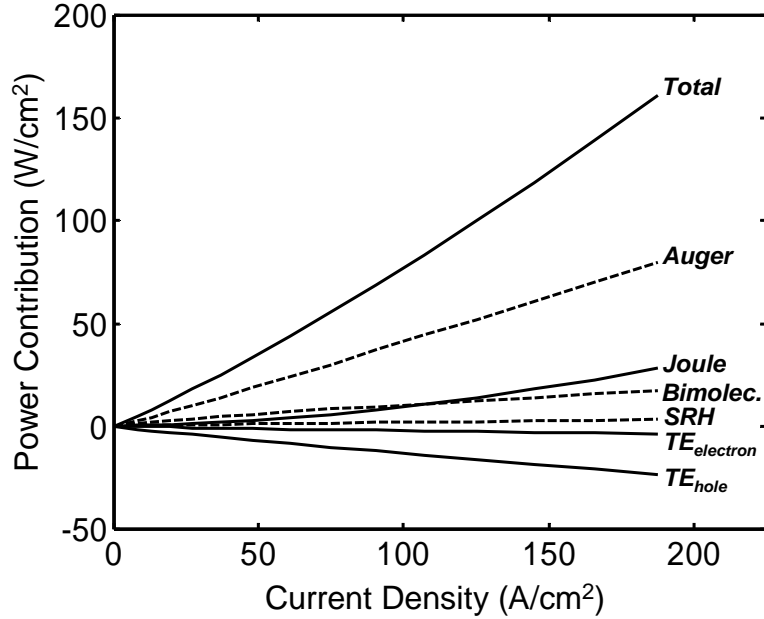
Figure 3-19: Total contributions of the modeled transport processes (assuming zero contact resistance). Dotted lines indicate recombination processes (Auger, spontaneous emission, and SRH) that clamp above the laser's threshold current density; threshold is not shown here since it depends on geometry. Thermoelectric terms are shown as negative for plotting purposes and to illustrate a reduction in device temperature.

relationship with the quasi-Fermi level), the total thermoelectric heat exchange can be calculated for a given device bias. The spatial profile of thermoelectric heat exchange and its implications for device design will be studied at length in Chapter 4.

The different transport processes for the laser diode under study are shown as a function of device bias (assuming zero contact resistance) in Figure 3-19 [85]. All processes shown have been summed over the length of the device to yield a total contribution. The Joule term is found by adding together the resistive drops within each region (which turn out to be very small) and the quasi-Fermi discontinuities at the heterojunctions.

In order to estimate the contact resistances of the two lasers, we examine their I-V characteristics, as shown in Figure 3-20. For a laser in steady-state above threshold, the photon density gain inside the cavity must remain at its threshold value (equal to the loss); otherwise, stimulated emission would cause the field amplitude to grow
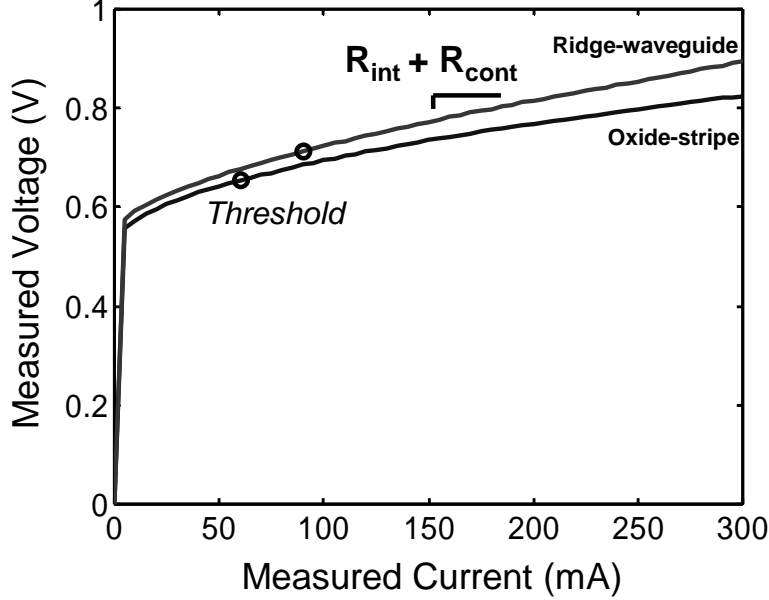
Figure 3-20: Contact resistance is found by examining the *I-V* characteristic above threshold.

without bound. This restriction leads to the clamping of the active region carrier density and in turn to the clamping of the Auger, spontaneous emission, and Shockley-Read-Hall processes [69]. Above threshold, therefore, the total resistance $\frac{\mathrm{d}V}{\mathrm{d}I}$ is equal to only the internal resistance R_{int} plus the contact resistance R_{cont}. In order to calculate R_{int}, we subtract the recombination terms in Figure 3-19 from the total power density; fitting this to $J^2 R_{\mathrm{int}}$ yields $R_{\mathrm{int}} \approx 1.1 \times 10^{-3}$ Ω-cm^2. Using a slope fit in Figure 3-20, we determine R_{cont} to be 0.19 Ω (3.4×10^{-4} Ω-cm^2) for the ridge-waveguide device and negligible (less than 0.01 Ω (2×10^{-5} Ω-cm^2)) for the oxide-stripe device. The effects of 3D current spreading have been neglected in this calculation. Contact resistance is expected to be low in these devices due to the fact that the topside contact, which typically dominates contact resistance due to its small size relative to the bottomside contact, is formed with *p*-GaSb, a material known to exhibit decreased band-bending due to Fermi-level pinning. Contacts to *p*-GaSb have had measured resistivities down to 10^{-8} Ω-cm^2 under appropriate formation conditions [86]. The reason for the larger contact resistance of the ridge-waveguide device is not known for certain, as the processing of these devices was performed
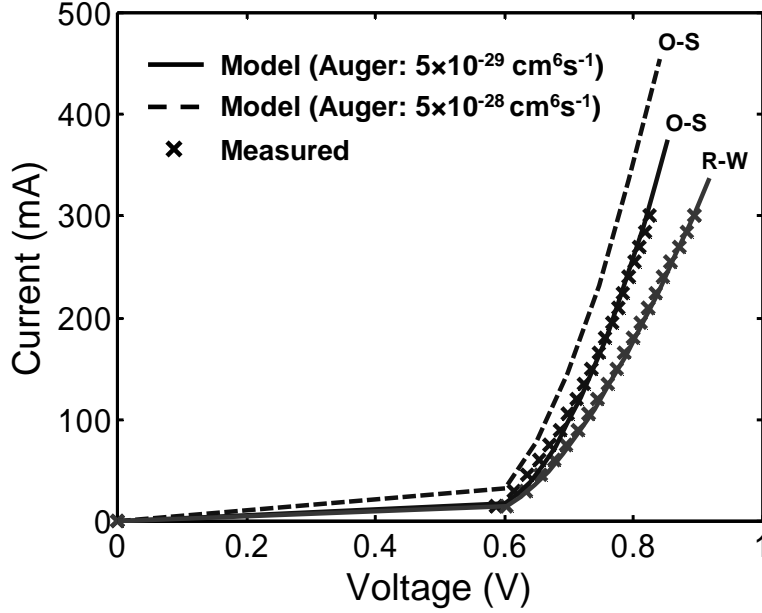
Figure 3-21: Current-voltage characteristics of ridge-waveguide (R-W) and oxide-stripe (O-S) lasers, both modeled and measured experimentally. Sensitivity to the literature value of the Auger recombination rate (5×10^{-29} cm^{6}s^{-1}) is demonstrated.

elsewhere [5].

Taking into account these measured contact resistances, the full *I-V* characteristics of the devices can be modeled, as shown in Figure 3-21. The measured values are also shown, as well as a curve which demonstrates the sensitivity of the model to the Auger recombination rate by increasing the literature value by an order of magnitude.

Having some confidence that the electrical model used to simulate transport in these devices is accurate, we proceed to relate this model to a temperature profile.

3.3.2 Thermal Model

Using the carrier transport model as described above, we have derived heat exchange terms due to non-radiative recombination, Joule heating, and thermoelectric effects in two GaSb-based semiconductor lasers. While the majority of the heat produced in each device is deposited by Auger recombination in the quantum well, some of the heat exchange is distributed by other mechanisms to different regions of the device. In order to numerically solve for the temperature profile generated by the distributed
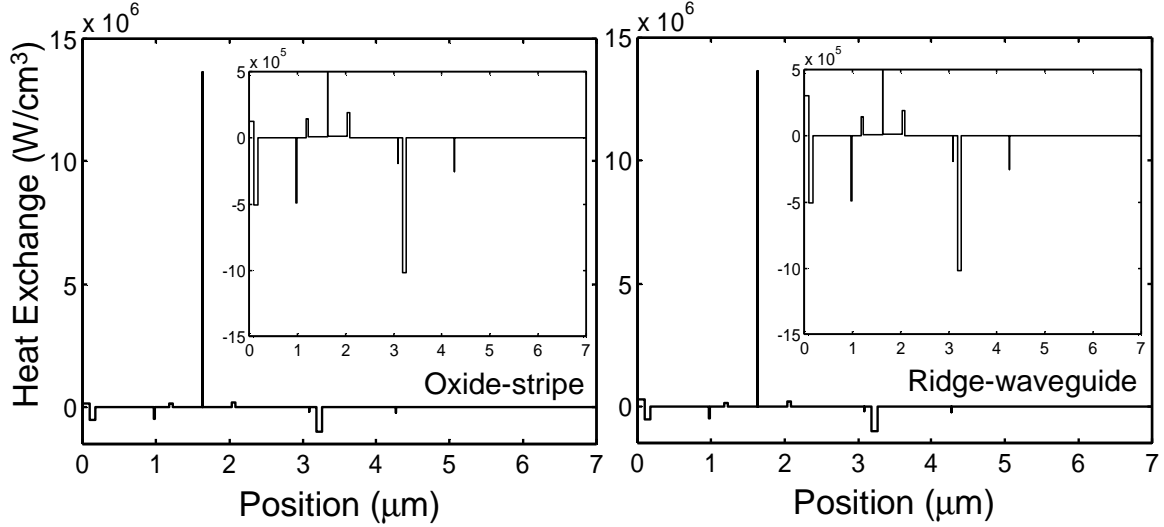
Figure 3-22: Heat source distributions in both devices at a voltage bias of 0.7V. The ridge-waveguide device has a slightly higher contact resistance, as shown more clearly in the insets.

internal heat sources, we use two-dimensional finite element analysis [68, 87]. Based on Figure 3-9, we neglect convection and radiation, assuming that most power is dissipated through conduction.

Because the heat source distribution is smoothly varying and the finite element method requires discretization on a solution mesh, we will approximate the heat source by defining a mesh that has a layer corresponding to each device layer and a thin region between each layer for junction effects. The heat exchange within each layer is then averaged as before, and the value is given for the entire mesh layer; the junction terms (such as thermoelectric effects and Fermi-level discontinuities) are inserted in the thin junction mesh layers. Heat exchange distributions at a voltage bias of 0.7V are illustrated in Figure 3-22. The resulting cross-section temperature profiles are shown in Figures 3-23 and 3-24. Figure 3-25 shows the temperature profile of a vertical slice through the center of each contact (position = 0 μm), and Figure 3-26 shows the temperature profiles of the contact surfaces.

The fact that the quantum well of the oxide-stripe device is at a higher temperature than the surface implies that heat is being conducted to the surface; this is reasonable because the surface of the device (and the surrounding area) is covered with a broad

90
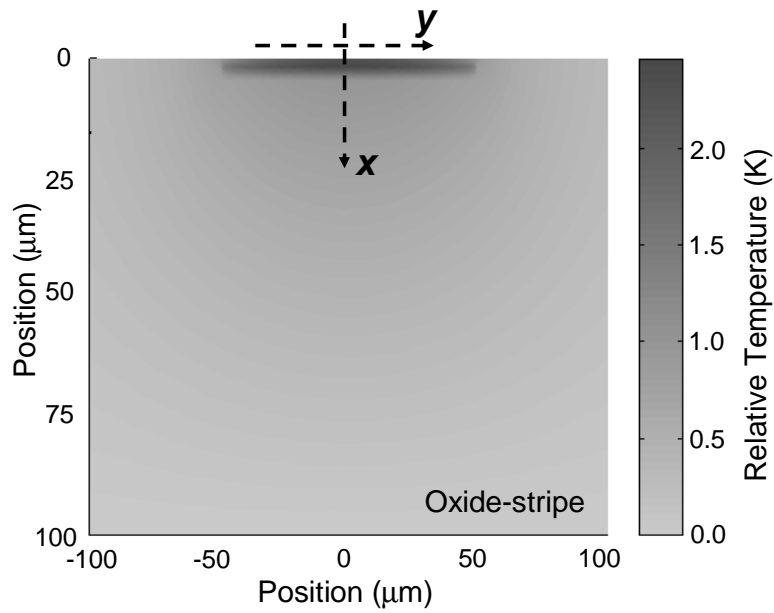
Figure 3-23: Temperature profile of oxide-stripe laser at a voltage bias of 0.7V.
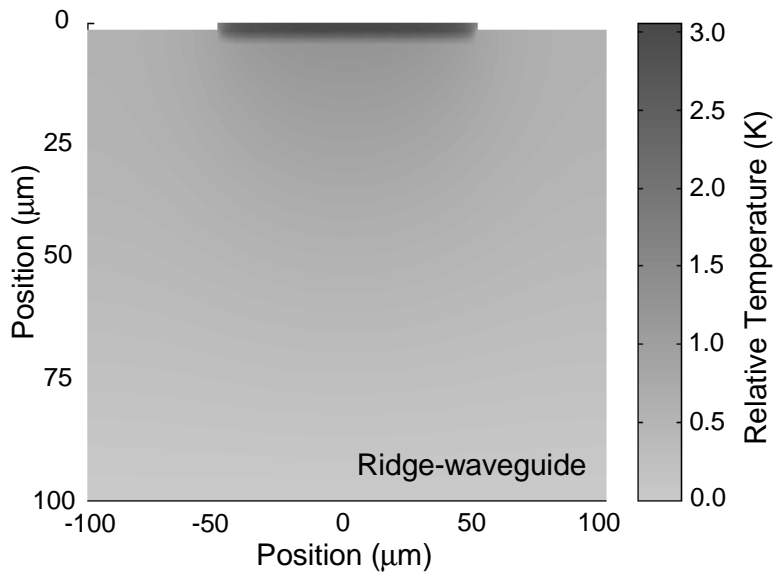
Figure 3-24: Temperature profile of ridge-waveguide laser at a voltage bias of 0.7V.
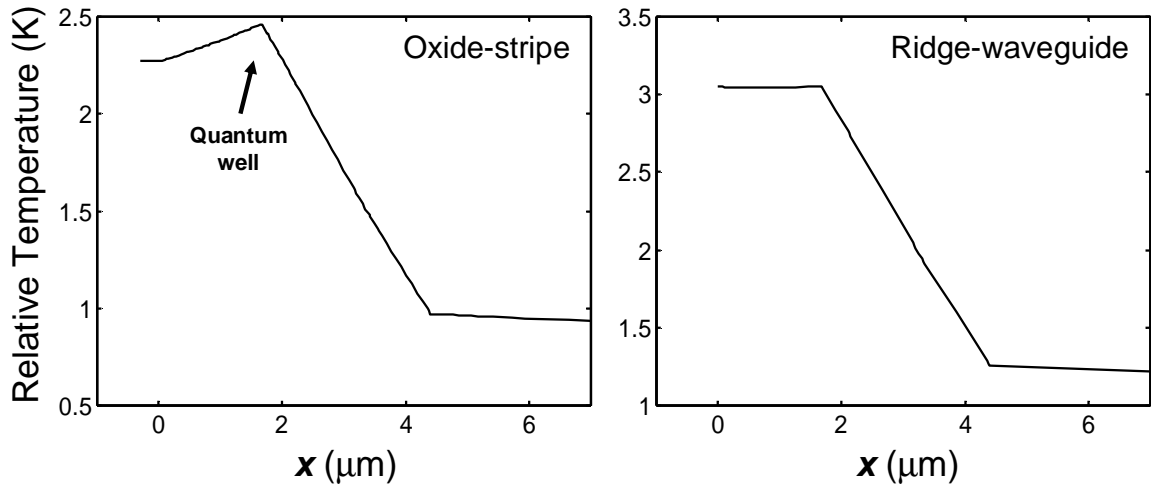
Figure 3-25: Temperature profile of a vertical slice through the contact center at a voltage bias of 0.7V. The horizontal axis refers to depth into the laser.
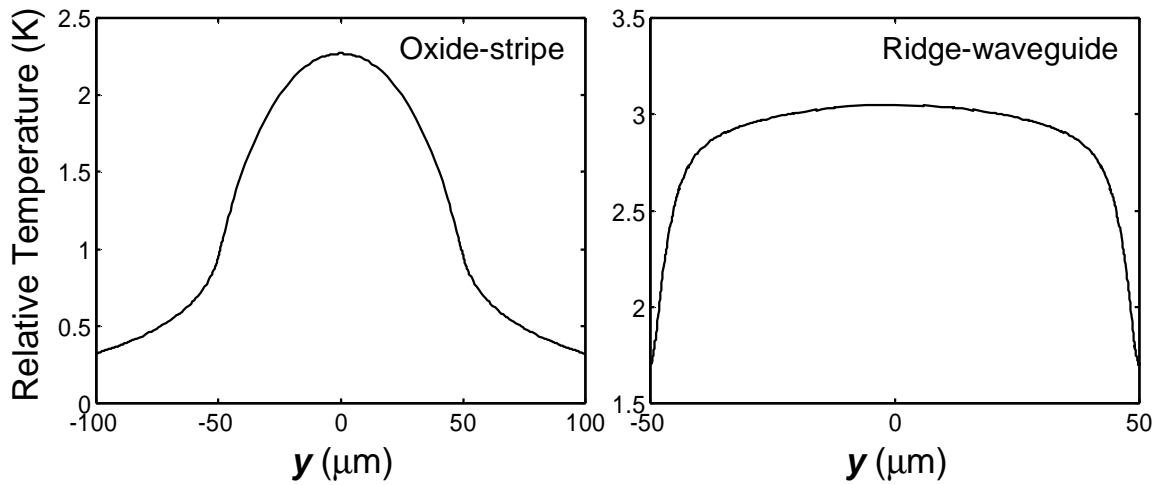
Figure 3-26: Temperature profile of a horizontal slice at the contact surface at a voltage bias of 0.7V. The horizontal axis refers to position along the width of the contact.
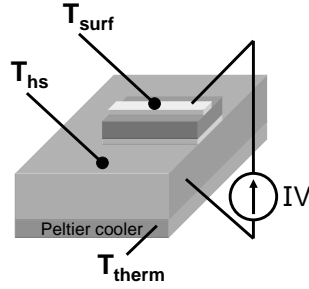
Figure 3-27: Microthermocouple probe measurement setup.

metal contact. The highly peaked temperature profile on the contact surface again implies that heat is being carried away from the device by the metal contact. The ridge-waveguide laser, on the other hand, has very little conduction of heat from the quantum well to the surface contact. Because the contact area is limited to the surface of the ridge, there is nowhere for the heat to be transported.

We verify this thermal model by placing the devices on a large copper-block heatsink and using $25 \times 25 \mu m^2$ microthermocouple probes (as in Section 3.2.3; see Figure 3-27) to measure the temperature difference ΔT between the topside contact and the bottomside heatsink under bias [79]. Surface temperature measurements, performed for the first time on a mid-IR laser, were averaged from data taken across the laser contacts (due especially to the large size of the probe with respect to the temperature variations in the oxide-stripe contact). Figure 3-28 demonstrates the correlation of the measured data with the finite-element model.

By integrating drift-diffusion / Poisson's equation simulation with a finite element model, we have demonstrated that we can predict temperature rise in diode lasers using independently measured material parameters (such as electrical conductivity, thermal conductivity, and Auger coefficient) without recourse to fitting parameters. Note that we did not self-consistently introduce a temperature dependence into the material parameters (see Figure 3-11); however, the error is expected to be small because the thermal gradients are not large. Next we will use these models to suggest design improvements for these devices based on decreasing their internal series resistances.
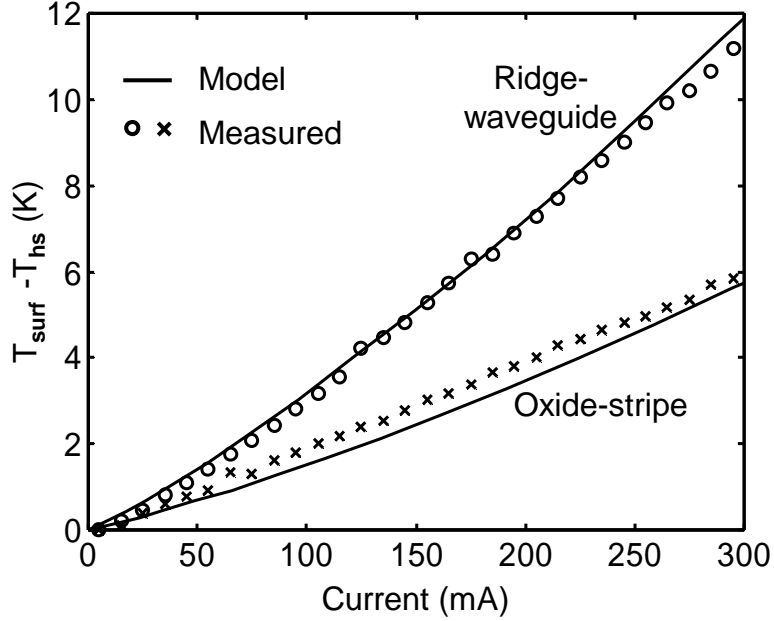
Figure 3-28: Modeled and measured surface to heatsink temperature difference.

3.4 Decreasing Series Resistance

As for most devices, high-bias operation causes performance rollover due to increased temperature in the GaSb-based laser diodes discussed above. This is illustrated for the oxide-stripe device in Figure 3-29. In the design of this device, 50-nm doping-graded regions were inserted between the cladding and barrier layers on both the p-type and n-type sides in order to decrease the heterojunction resistances by lowering the band spikes. As shown in Figure 3-30, however, the spikes at these interfaces remain as high as $2k_BT$ and are expected to impede current flow.

By increasing the widths of both the p-type and n-type graded regions, the heights of the spikes are decreased, as shown in Figure 3-30. This appears as a decrease in the series resistance of the device, as shown in Figure 3-31, and a consequent reduction in the operating temperature of the device, as shown in Figure 3-32. While this modeling suggests that increasing the lengths of the graded regions will improve electrical transport and therefore improve thermal performance, it is important to note that the optical properties of the devices may be adversely affected due to increased loss in the p-graded region.
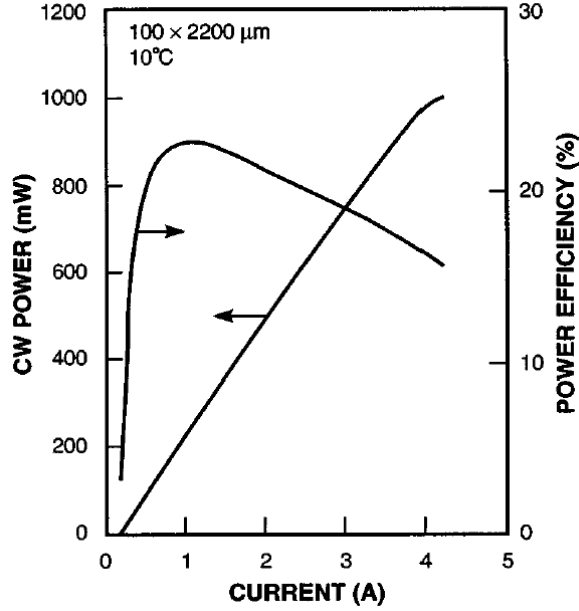
Figure 3-29: Rollover in light power and power efficiency of the oxide-stripe device at high bias levels due to increased temperature [5]. This is the baseline device with 50-nm graded regions.

3.5 Conclusion

The models developed in this chapter can be used to fully characterize the electrical and thermal behavior of a semiconductor laser diode. An examination of external heat flow mechanisms demonstrated that while convection is not an important effect in the cooling of a laser diode, it is substantial enough to warrant inclusion in a full energy balance model for the device. This energy balance model can then be used to optically characterize the laser through a non-destructive thermal probing technique.

The experimentally-verified carrier transport and thermal models developed in this chapter for internal heat exchange can facilitate the optimization of electrical properties such as series resistance, and can also be used to predict operating temperature. In addition, they enable the optimization of bipolar thermoelectric properties as discussed in Chapter 2; in the next chapter, we will examine a novel design for a semiconductor laser diode that utilizes internal Peltier cooling to lower the temperature of the active region.
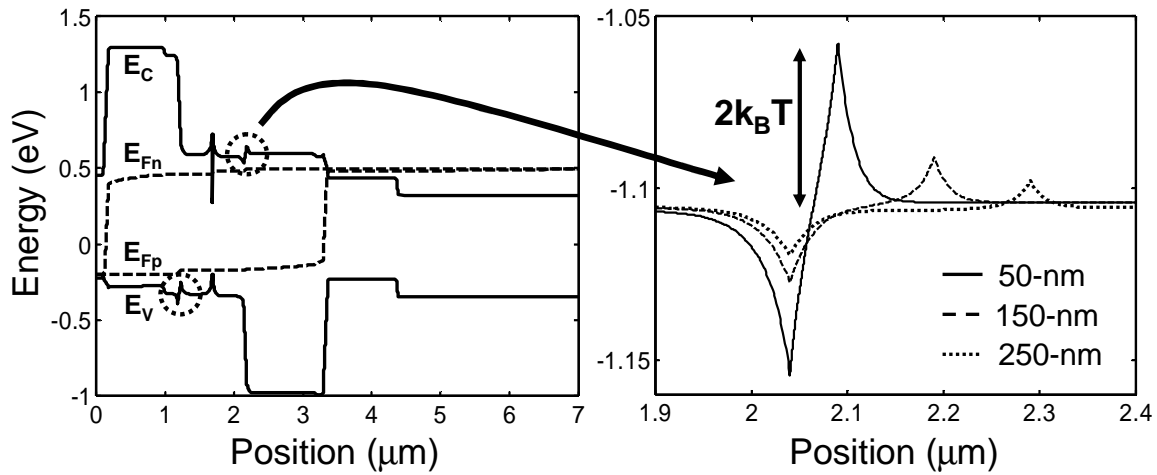
Figure 3-30: Band structure of GaSb-based lasers at a voltage bias of 0.7V. As shown in the magnification at right, the cladding/barrier band spikes are large in the baseline device; increasing the length of the graded interface decreases the spike height and improves transport across the junction.
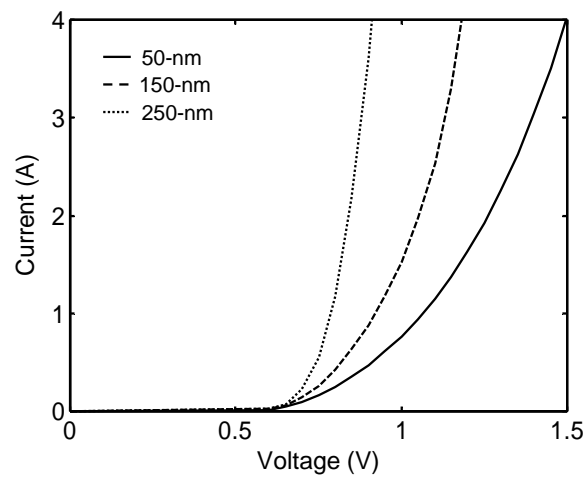
Figure 3-31: Current-voltage relationships for devices with graded region lengths of 50, 150, and 250 nm.
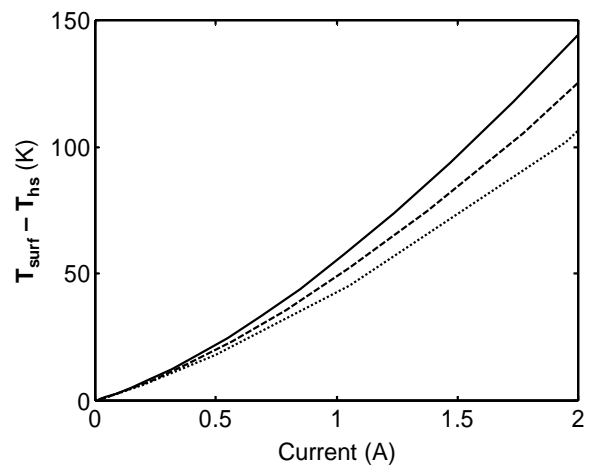
Figure 3-32: Operating temperatures (with respect to heatsink temperature) for devices with graded region lengths of 50, 150, and 250 nm.

Chapter 4

Thermoelectric Optimization of Laser Design

In previous chapters, we have developed a description of thermoelectric effects in bipolar devices, modeling and optimizing thermoelectric cooling in simple diode structures. In order to extend the discussion to a more complicated device, namely the semiconductor laser diode, we analyzed both internal and external heat exchange in lasers, verifying our transport model with electrical and thermal measurements. Having confidence in our transport simulations, we now examine the role that thermoelectric effects play in the operation of a laser diode, proposing a new device design that targets active region heating by placing thermoelectric cooling sources nearby.

4.1   Thermoelectric Model of a Laser Diode

In the design of a semiconductor laser, it is desirable to have both the optical mode and the carriers confined to the active region, in order to produce the greatest overlap between the mode and the gain medium. This is accomplished in the traditional double-heterostructure device by using a core material which has a smaller bandgap than the adjacent cladding regions, since for most material systems refractive index has an inverse relationship with bandgap [69]. Carrier confinement is simultaneously realized since the heterointerfaces between most III-V materials are Type-I; additional
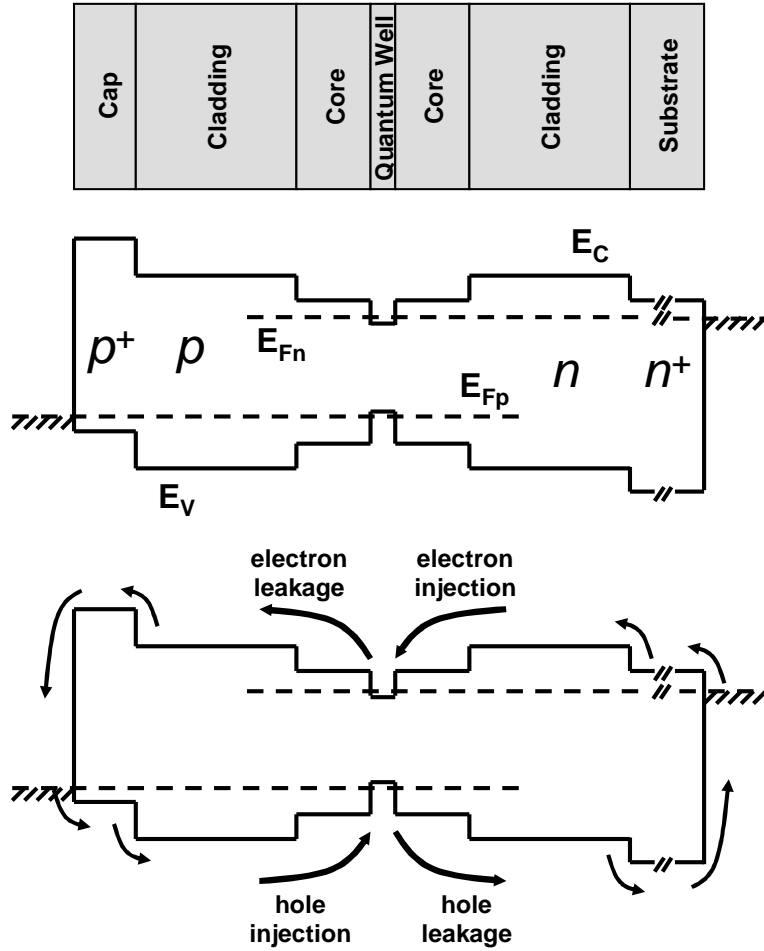
Figure 4-1: Layer structure, band structure, and average transport energy variation for an SCH laser diode. The processes of injection and leakage are also illustrated.

carrier confinement is achieved in a separate-confinement heterostructure (SCH) device by adding a quantum well to the waveguide core. Shown in Figure 4-1 is a typical SCH laser diode, with ohmic contacts, a p^+ cap, and an n^+ substrate, biased approximately at threshold. The purpose of the capping layer is to decrease the electrical resistance between the metal contact and the laser.

When forward bias is applied to the laser, electrons and holes are injected into the core from the n-type and p-type regions respectively; they then travel across the core and are trapped in the quantum well. A laser is traditionally designed to maximize the amount of optical recombination that occurs in the well, since it is this photon emission that makes up the stimulated emission of light from the device. A certain

fraction of the injected carriers do not contribute to optical recombination, however, due to non-radiative recombination or leakage out of the quantum well and core. The magnitude of the leakage current is set by the depth of the quantum well, the height of the core/cladding band offset, and the operating temperature. As the active region temperature increases (due, for example, to non-radiative recombination), carriers have more energy to leak out of the well.

As with the *p-n* diode, we recognize that electrons and holes have separate quasi-Fermi energies; we define Peltier heat exchange terms for each type of carrier at the heterointerfaces, adding them together to yield the total bipolar thermoelectric heat source distribution. As the carriers enter the core region, their average transport energy is reduced, causing heat to be generated at the cladding/core interfaces. A portion of the injected carriers leak out of the core region without recombining, giving rise to thermoelectric cooling at the second core/cladding interface. Since the injection current is typically much larger than the leakage current, however, the core/cladding junctions will exhibit an overall positive heat flux as shown in Figure 4-2. In the case of appreciable leakage current, less thermoelectric heating is expected, although this comes at the expense of the laser's quantum efficiency [88, 89].

A similar argument can be used to estimate thermoelectric cooling or heating at the quantum well interfaces. Here the non-equilibrium nature of the carrier distribution in the well should be taken into account [90]. In the following discussion, however, these effects are ignored; we will keep the quantum well heat exchange terms the same for the various designs so that small errors in the calculation of quantum well heating will not change the validity of the analysis.

4.2   Optimized Design

By modifying the traditional SCH band structure, one can construct a device whose thermoelectric heat exchange distribution includes sizable cooling terms in the vicinity of the core without sacrificing carrier confinement. Figure 4-3 depicts the band structure of such a device [91]. In this case, injection current and leakage current
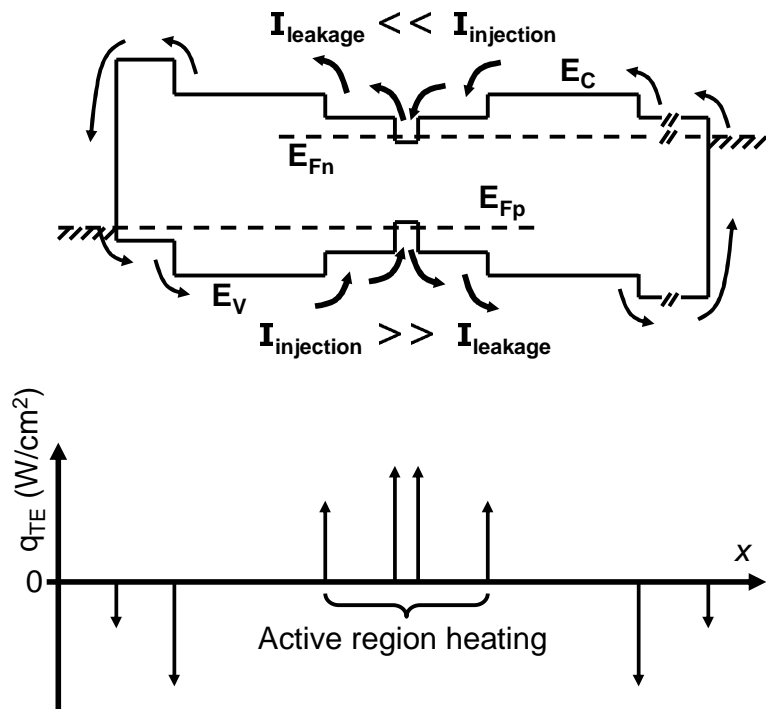
Figure 4-2: Illustration of thermoelectric heat exchange for an SCH laser diode. The injection current heats the active region, while the leakage current (typically much smaller than the injection current) cools it.
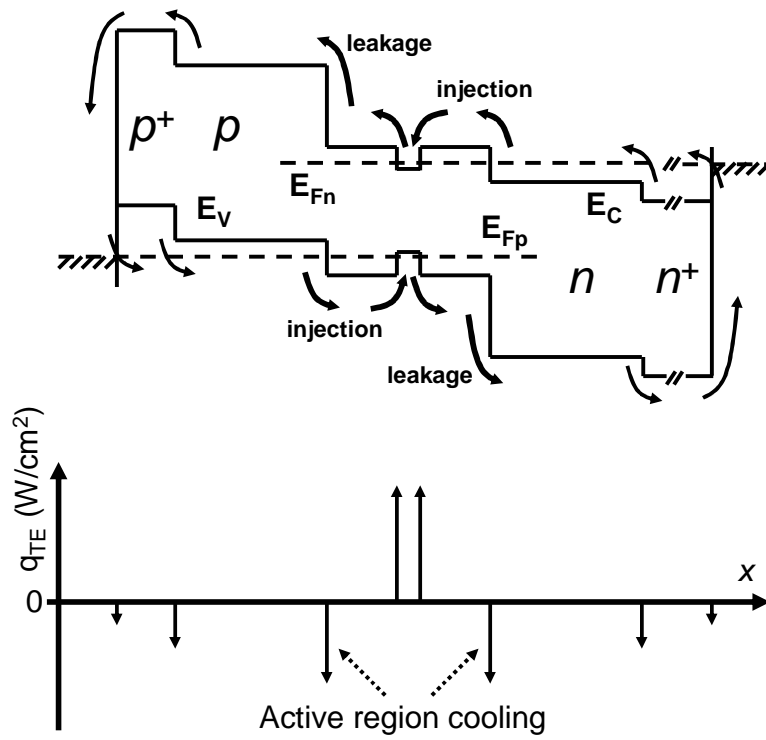
Figure 4-3: ICICLE structure: both injection and leakage currents add to thermoelectric cooling of the active region.

both contribute to cooling at the cladding/core interfaces. Because the same carriers which eventually radiatively recombine also produce cooling, this configuration is termed an ICICLE (Injection Current Internally Cooled Light Emitter). The electrical resistance of the ICICLE structure will be nearly the same as the traditional SCH design, as long as the barrier heights are small enough to restrict electron transport to the diffusive rather than the thermionic regime. It is important to note that the sums of the thermoelectric heat exchange terms for the ICICLE design and the traditional SCH design are nearly the same for the same bias. There are two ways by which the optimization of thermoelectric effects within the ICICLE design can improve the temperature characteristics of a semiconductor laser. First of all, the spatial distribution of Peltier cooling and heating terms at the interfaces is modified so that cooling happens near the active region and the complementary heating occurs at the device edges, where it is more readily conducted away. Secondly, the design can be such that the sum of the Peltier cooling and heating terms produces a net cooling in the device, analogous to optical refrigeration as discussed in Section 2.5.2.

Two ways to obtain the "staircase" ICICLE structure are to dope the cladding regions heavily or to use a material system whose alignment is Type-II. Heavy p-type doping usually leads to excessive intervalence band absorption, so it is preferable to use a Type-II interface at the p-cladding/core interface. The n-cladding/core interface can typically be pulled into correct alignment by heavy n-type doping. A Type-II interface may also be used at this interface, as long as the n-cladding bandgap remains larger than that of the core. A further design consideration for the ICICLE is the ratio between band offsets and band gap; material systems for which this ratio is high are likely to achieve better cooling due to larger Peltier terms with respect to the non-radiative recombination energy.

4.3   Antimonide ICICLE design

In order to show that the ICICLE structure is realizable in a known material system, we next model a prototypical device using the tools developed in Section 3.3.

103

Figure 4-4: Layer structure for conventional SCH and ICICLE designs realized in the $Ga_{1-x}In_xAs_ySb_{1-y}$ material system. Doping is given in units of cm^{-3}.
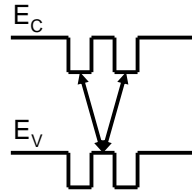
Figure 4-5: "W" quantum well band alignment: electrons recombine with adjacent holes.

Quaternary alloys in the $Ga_{1-x}In_xAs_ySb_{1-y}$ are a good match for the ICICLE due to their type-II band alignment and small band gap [9]; they also share a common GaSb material parameter base with the lasers of Section 3.3.

Layer structures for conventional SCH and ICICLE structures that we will model are shown in Figure 4-4. Note that this structure has 3 $\lambda = 2.65\mu m$ quantum wells, which can be achieved in this material system by using either a "W" alignment (as done here) or by adding strain [9]. An illustration of the "W" alignment is shown in Figure 4-5. It is common practice to use multiple quantum wells to increase the amount of optical recombination overlapping with the optical mode. In order to pull
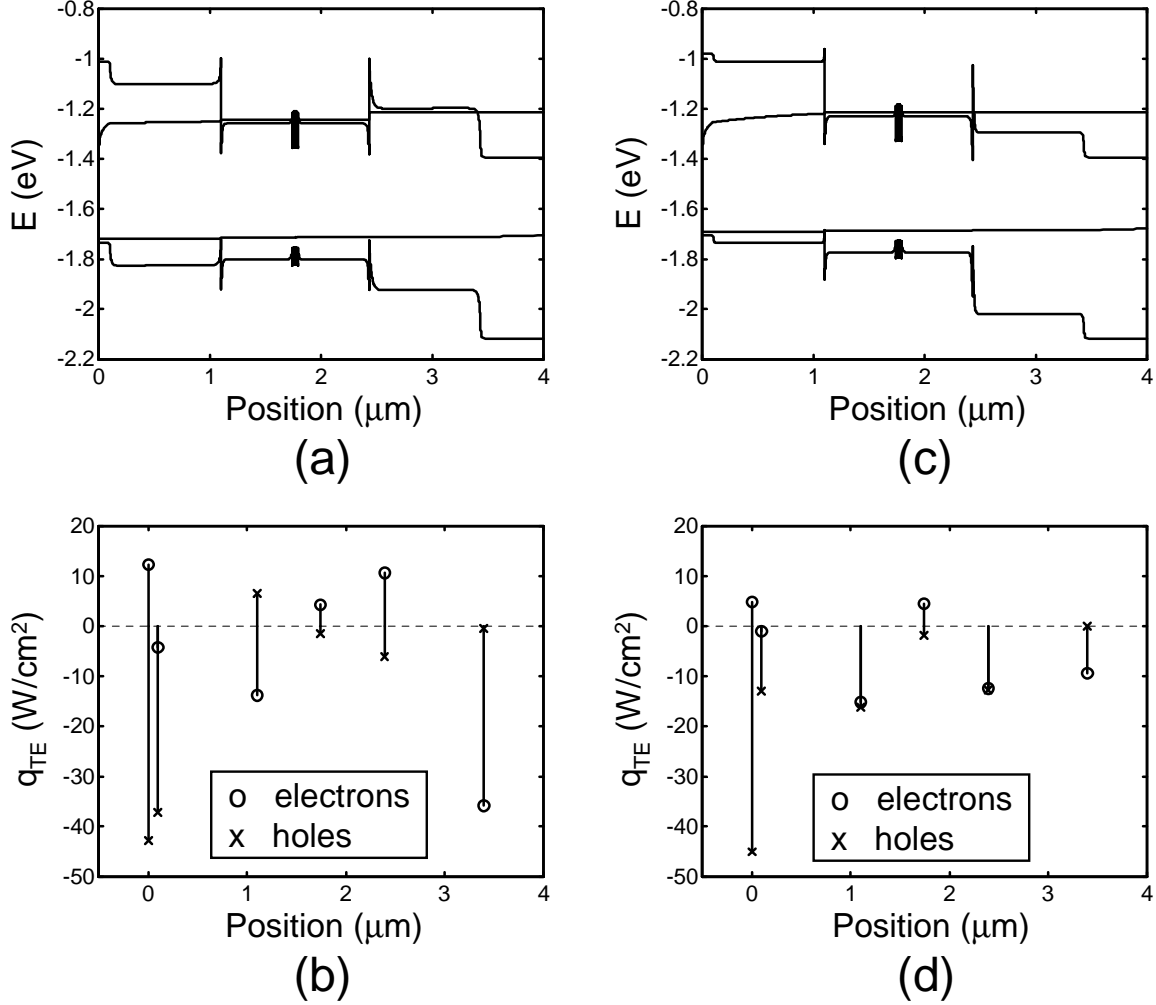
Figure 4-6: Band structure and bipolar thermoelectric heat source distribution for GaInAsSb (a & b) conventional SCH and (c & d) ICICLE structures at a current density of 475 A/cm^2. Contact/substrate term is not shown.

the conventional SCH band structure into ICICLE alignment, the doping levels of both the n-cladding and p-cladding were increased from 1×10^{17} cm^{-3} to 1×10^{18} cm^{-3}.

The band structures and bipolar thermoelectric heat exchange profiles of both devices are shown at a bias current of 475 A/cm^2 in Figure 4-6. Carrier transport was calculated by solving the drift-diffusion equations self-consistently with Poisson's equation, as before. Peltier coefficients were again determined by averaging inside each device layer. Leakage currents at threshold ($qV_{\text{bias}} \approx$ quantum well band gap [69])
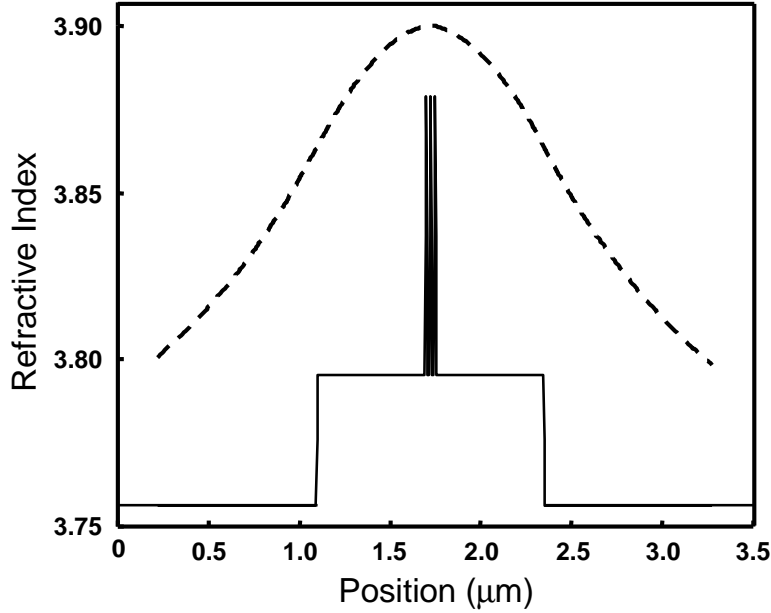
Figure 4-7: Refractive index profile and single optical mode.

are approximately 8% at 100 A/cm^2 in the conventional SCH structure and 3% at 190 A/cm^2 in the ICICLE structure. Notice that cooling caused by electron leakage out of the core in the conventional structure overcomes the hole injection heating term at the p-cladding/core interface. The reason for the slight thermoelectric cooling of holes entering the quantum well is the "W" alignment of the wells [9].

As shown in Figure 4-7, further modeling confirms that the structures are single-mode and have an optical mode overlap of 0.4% per quantum well. These character-istics are typical for lasers in this material system, which can have threshold current densities as low as 50 A/cm^2 [5] (typical laser threshold current densities for other material systems are on the order of 100 A/cm^2 [69]).

From Figure 4-6, it is apparent that the core/cladding thermoelectric terms roughly cancel each other for the conventional device, while the ICICLE design has net ther-moelectric cooling at these interfaces. This is shown more clearly in Figure 4-8, which plots the sums of the cladding/core terms as a function of current bias. The conventional design has greater cooling at the cap/cladding and cladding/substrate interfaces; as stated above, this cooling power is at a further distance from the active
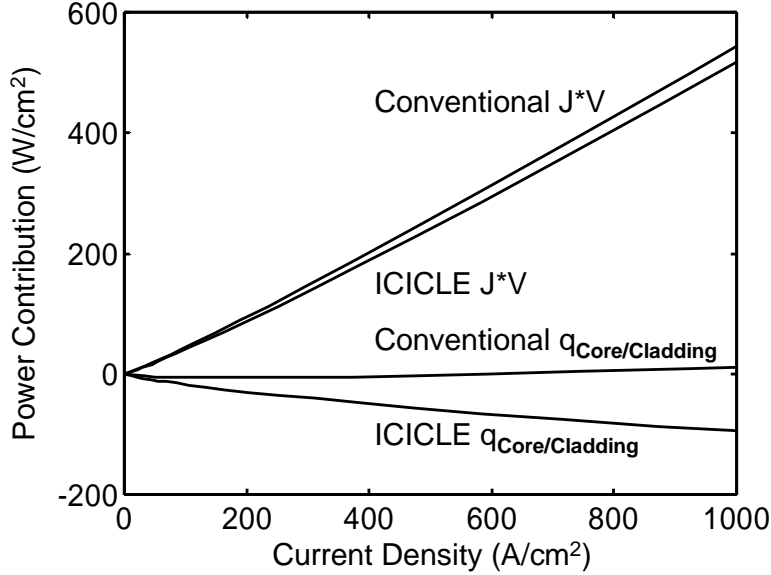
Figure 4-8: The sums of the core/cladding thermoelectric terms for both devices. Total JV power is also shown for comparison.

region and thus is less likely to influence its temperature.

In order to investigate the effects of heat source placement in the two structures, a 2D finite-element model was used as in Section 3.3.2. The geometry implemented was the standard oxide-stripe configuration, with a laser contact area of $500 \times 50 \mu m^2$. The assumed contact resistivity was 1×10^{-6} Ω-cm^2, again reflecting the low contact resistance of p-GaSb due to Fermi-level pinning.

The simulated quantum well temperature is shown for both structures in Figure 4-9. As expected, the ICICLE does a better job of cooling the active region. At a current bias of 1000 A/cm^2, the IV power of the ICICLE is 96% that of the conventional design (see Figure 4-8), while its quantum well temperature rise is only 85% that of the conventional design. This indicates that the temperature difference between the two structures is mostly due to heat source rearrangement and not due simply to a decreased input power.

In order to further examine the thermoelectric role of injection and leakage, we look at the quantum well temperature contributions of the core/cladding injection and leakage current components [92]. As shown in Figure 4-10, the ICICLE injection
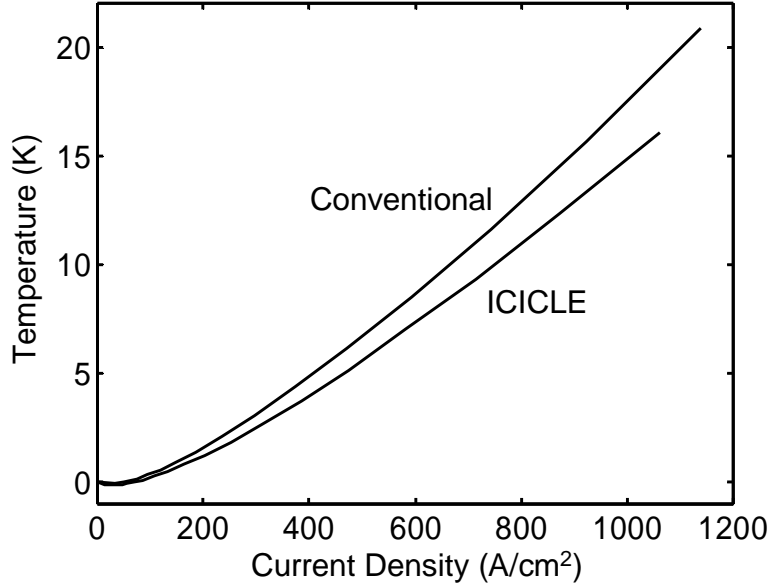
Figure 4-9: Simulated quantum well temperature (with respect to heatsink) for both devices.

current cools while the conventional injection current heats. Because the quasi-Fermi level for holes typically lies inside the band gap for reasonable doping densities, the Peltier coefficients for holes are typically larger than those of electrons, making the hole current especially important to thermoelectric injection cooling design. Electrons, on the other hand, have a lighter effective mass and therefore are more likely to contribute to leakage current. As shown in Figure 4-11, leakage electrons have a strong contribution to thermoelectric cooling in both the conventional and ICICLE designs.

4.4 Characteristic Temperature and Further Optimization

As stated in Section 3.2.2, the total radiated power of a laser above threshold $(I > I_{\text{th}})$ is equal to $\eta_{\text{LED}} I_{\text{th}} + \eta_{\text{d}}(I - I_{\text{th}})$. Given that the emitted photons each have an energy approximately equal to the band gap E_G of the quantum well, the radiated power can be rewritten as $\tilde{\eta}_{\text{LED}} \frac{E_G}{q} I_{\text{th}} + \tilde{\eta}_{\text{d}} \frac{E_G}{q}(I - I_{\text{th}})$ where $\tilde{\eta}$ is known as a *differential quantum*
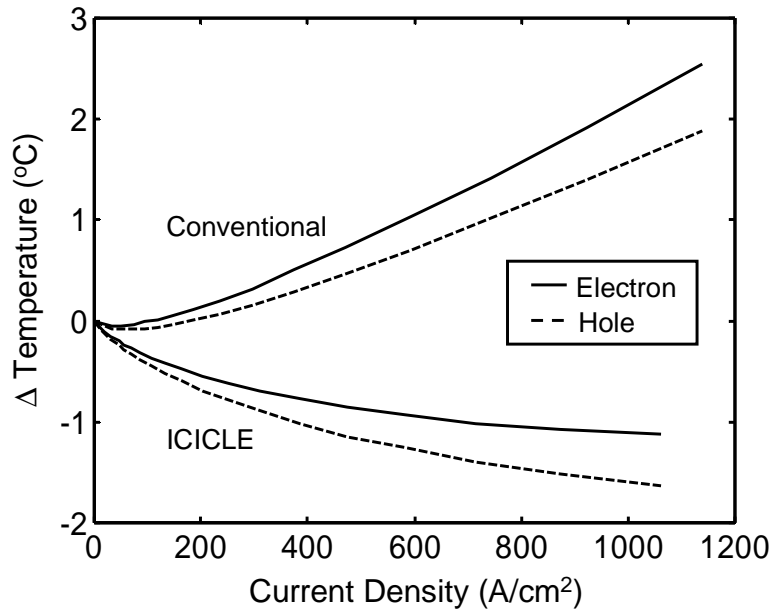
Figure 4-10: Quantum well temperature contributions of the electron and hole injection currents at the core/cladding interfaces.
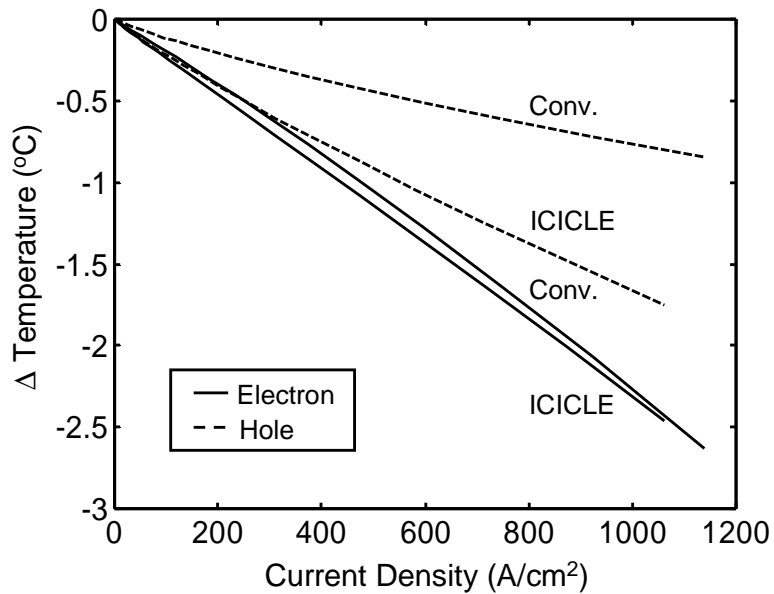
Figure 4-11: Quantum well temperature contributions of the electron and hole injection currents at the core/cladding interfaces.

efficiency; $\tilde{\eta}_d$ is the fraction of injected carriers above threshold that recombine with stimulated emission. Because the bias voltage V must be greater than $\frac{E_G}{q}$ in order to achieve stimulated emission [69], the input power IV is always greater than the radiated power when the laser is operating. Since all Peltier cooling must be balanced by Peltier heating, a laser can therefore never experience net cooling.

By rearranging the Peltier cooling terms so that they are closer to the quantum well, however, the ICICLE does lower the active region temperature below that of the conventional SCH design. In order to develop an intuitive picture of internal thermoelectric cooling, we examine the terms which most differentiate the two devices: the injection core/cladding thermoelectric terms (noting that the leakage core/cladding terms in Figure 4-6 are roughly the same for each device). We define $q_{\mathrm{TE,inj}}$ to be the sum of these two terms for each device, and the difference $\Delta q_{\mathrm{TE,inj}} = q_{\mathrm{TE,inj}}^{\mathrm{Conv}} - q_{\mathrm{TE,inj}}^{\mathrm{ICICLE}}$ to be the thermoelectric power enhancement of the ICICLE design. Similarly, we examine the quantum well temperature enhancement given by $\Delta T = T^{\mathrm{Conv}} - T^{\mathrm{ICICLE}}$. Normalizing these two quantities by the total power JV^{Conv} and temperature T^{Conv}, we plot the results in Figure 4-12.

Based on the fact that the two ratios are close for most of the bias range, we conclude that the injection energy difference between the conventional and ICICLE structures is the determining factor in the calculated temperature difference. Remembering that $q_{\mathrm{TE,inj}} = J\Delta\Pi$ for each interface (where $q\Delta\Pi$ is approximately the band offset), we can write the following relationship for the internal thermoelectric cooling of a laser diode:

$$\frac{T^{\mathrm{Conv}} - T^{\mathrm{ICICLE}}}{T^{\mathrm{Conv}}} \approx \frac{(\Delta E_C + \Delta E_V)^{\mathrm{ICICLE}} - (\Delta E_C + \Delta E_V)^{\mathrm{Conv}}}{qV^{\mathrm{Conv}}} \equiv \frac{\Delta B}{qV^{\mathrm{Conv}}} \qquad (4.1)$$

where the bulk band offsets ΔE_C and ΔE_V are shown in Figure 4-13. It is important to note that these band offsets are the *bulk* differences (taking into account band bending) and not just the heterojunction alignment; they are therefore bias-dependent since the bands move with respect to each other as the device is biased up. This is shown in Figure 4-14, which plots the injection energy difference ΔB as a function
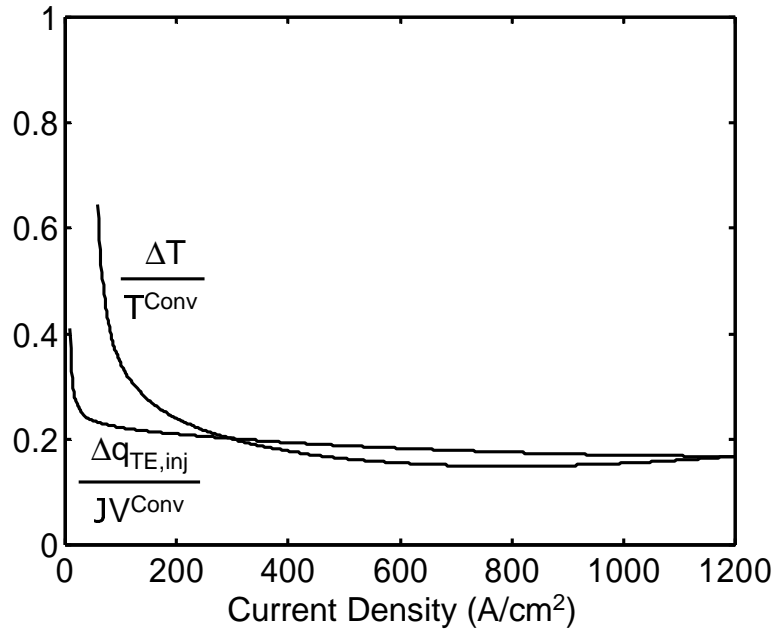
Figure 4-12: The normalized thermoelectric cooling power of injection is approximately equal to the normalized change in temperature.
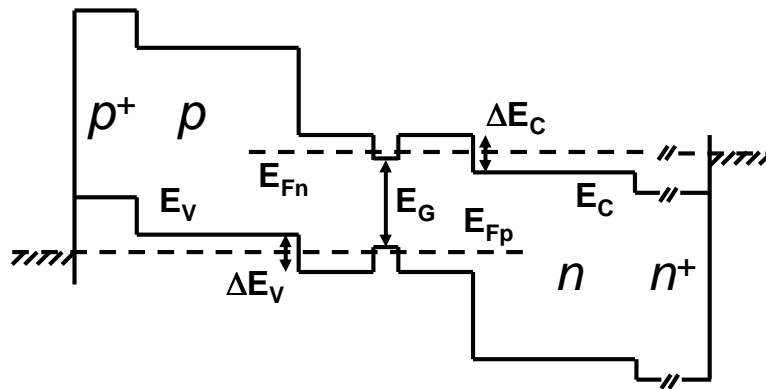
Figure 4-13: Important bulk band offsets for internal thermoelectric cooling.
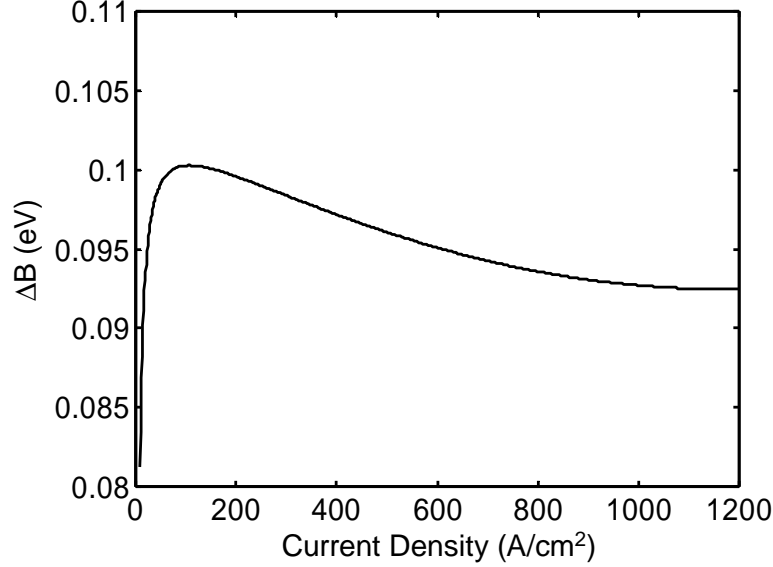
Figure 4-14: Injection energy difference ΔB between the conventional and ICICLE structures.

of bias, and Figure 4-15, which shows the individual terms of ΔB at a bias current of 475 A/cm^2. Because of the exponential current-voltage relationship, ΔB remains close to 0.1eV for a large range of current bias.

The thermal performance of a laser can be measured by the characteristic temperature T_0, defined by the change in threshold current I_{th} with operating temperature:

$$I_{\text{th}} = I_0 e^{\frac{T}{T_0}} \tag{4.2}$$

Realizing that $qV^{\text{Conv}} \approx qV^{\text{ICICLE}} \approx E_G$ at threshold, T^{ICICLE} can be substituted from Equation 4.1 into Equation 4.2 to show that

$$T_0^{\text{ICICLE}} = \frac{T_0^{\text{Conv}}}{1 - \frac{\Delta B_{\text{th}}}{E_G}} \tag{4.3}$$

For the antimonide ICICLE modeled above, Figure 4-12 gives $\frac{\Delta B_{\text{th}}}{E_G} \approx \frac{0.1}{0.47} \approx 0.2$, meaning that the ICICLE design improves the T_0 of the conventional SCH design by approximately 25%. We note that this calculation was not done self-consistently; the lowered temperature of the ICICLE structure is expected to have a nontrivial impact

112
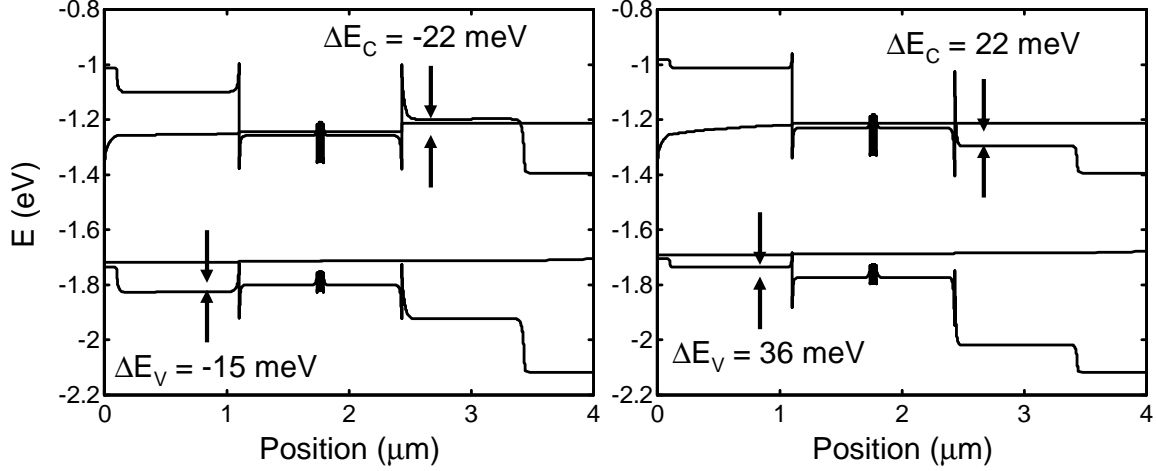
Figure 4-15: Bulk band offset injection terms that make up ΔB for conventional (left) and ICICLE (right) structures at a current bias of 475 A/cm^2.

on parameters such as Auger recombination that govern the threshold current. However, it is indicative of the fact that the ICICLE structure could have a substantially lower characteristic temperature.

This illustrates the importance of band offsets and doping concentrations in the thermal performance of a semiconductor laser. In order to further increase the thermoelectric cooling of the active region, there are several possible improvements that could be made. The band offset term ΔB could be improved by increasing the heterojunction offsets or the doping. Also, the thermal conductivity of the core region could be improved so that heat flows more easily to the thermoelectric cooling sources. Finally, a more radical design could be to modify the type of laser itself: an inter-subband laser, for example, is a unipolar laser that relies on stimulated emission via optical intersubband transitions [93]. Non-radiative heat sources (such as Auger-like effects) in these devices are on the order of intersubband transitions rather than on the order of the band gap. Since these transitions are roughly the same size as the band offsets, it could be possible to get enhanced operation by designing for internal thermoelectric cooling. This could be very important to intersubband lasers because they typically are very sensitive to operating temperature.

4.5 Conclusion

In summary, by modifying the conventional SCH laser design to shift internal thermoelectric cooling to the active region, device overheating can be reduced in a way that is quite different from methods which utilize an external cooler. Quantifying internal heat exchange requires a bipolar thermoelectric model that accounts for the changing values of thermoelectric parameters at different bias points. This model suggests that a "staircase" structure such as the ICICLE can achieve measurable cooling through the use of Type-II interfaces and appropriate doping. Some preliminary simulation results for long-wavelength GaInAsSb-based lasers have been presented, and the internal thermoelectric cooling effect on T_0 has been explored.

The modeling of the conventional SCH and ICICLE structures was not performed self-consistently (taking into account electrical, optical, and thermal effects) but is intended to demonstrate an application of internal thermoelectric cooling concepts to a laser structure below threshold. For high-power operation, internal cooling effects could be even more important due to the fact that they do not clamp as do non-radiative recombination processes at threshold [69]; every injected carrier contributes to thermoelectric cooling.

Chapter 5

Conclusion

The work presented here is a study of the thermoelectrics of bipolar devices in general and specifically the semiconductor laser diode. Starting with a thermoelectric description that included minority-carrier effects, we examined an unbiased homojunction diode and experimentally confirmed a large increase in the Peltier coefficient at the junction. Applying this model for the first time to forward-biased diodes, we proposed bias-dependent bipolar thermoelectric terms and derived the resulting analytical expressions for thermoelectric effects in simple homojunction structures. We then used numerical simulation to determine the optimum bias point for maximized internal cooling in several common diode material systems, demonstrating the thermoelectric importance of materials with high mobility and low thermal conductivity. In anticipation of more complicated devices, we demonstrated an averaging model based on the results of a transport simulation, applying this model to a simple heterojunction diode and demonstrating that the sign of internal Peltier cooling can change sign as a function of bias.

With the intention of eventually studying thermoelectric effects in a semiconductor laser diode, we sought to accurately model the heat exchange that occurs both internal to a laser and between a laser and its environment. To this end, we developed a total energy balance model for a laser diode, using microthermocouple probes to experimentally quantify the heat convection process from a laser diode for the first time. This energy balance model had the additional benefit of being useful for

the nondestructive wafer-scale testing of a laser's optical characteristics. We then used transport simulations and finite element analysis to predict the internal heat exchange of a laser diode, verifying these models with electrical and surface temperature measurements.

Having confidence in our ability to model electrical and thermal effects in a laser diode, we next took a closer look at a laser's internal thermoelectric effects. Recognizing that a conventional laser design places thermoelectric heat sources at interfaces near the temperature-sensitive active region, we proposed a new laser design that offers increased thermoelectric cooling at these interfaces. We showed that this new design could be realized in an existing material system, and then presented simulations confirming a decrease in active region temperature. Finally, we showed how internal thermoelectric cooling could impact a semiconductor laser's characteristic temperature.

5.1   Future Experimental Work

While some verification of bipolar thermoelectric effects has been obtained through zero-bias measurements of a diode (see Section 2.4), forward-bias measurements have not yet been carried out. In order to accomplish this, there are three experiments that remain.

5.1.1   Thermal Voltage Measurement of a Homojunction Diode

The work discussed in Section 2.4 involved the use of Scanning Thermoelectric Microscopy to measure the thermal voltage profile of a heated p-n junction. As shown in Figure 2-3, a sharp spike in the thermal voltage at the junction indicated a large increase in the Seebeck coefficient due to the sudden falloff in concentration of the majority carrier, and a discontinuity appeared due to the sudden change in the majority carrier species.

As a diode is forward biased, its junction is expected to undergo cooling. As its temperature drops, the thermal voltage measured by SThEM is likewise expected

116

to drop; for a heavily-doped InGaAs diode, this drop could be large due to the low thermal conductivity and high mobility of InGaAs (see Figure 2-16). Depending on the geometry of the diode and the proximity of a heat sink, this measurement could definitively indicate the presence of internal thermoelectric cooling.

5.1.2 Thermoreflectance Measurement of a Homojunction Diode

In order to better understand thermal effects at small spatial scales, new measurement techniques must be developed. Because the microthermocouple probes used in this work are 25 μm wide, they are not able to detect the nanoscale temperature variation predicted by internal thermoelectric cooling models.

One technique that shows promise for small-scale thermal measurement is thermoreflectance, in which a laser beam is focused onto the surface of a sample and the reflected power is carefully measured, as shown in Figure 5-1. Because the reflection coefficient R varies with temperature according to $\frac{\Delta R}{R} = C\Delta T$ (where $C \approx 10^{-5}\text{K}^{-1}$), the reflected power can be calibrated and used to calculate the surface temperature. This technique can be used to image temperature on a spatial scale down to approximately 1 μm, depending ultimately on the probe laser wavelength.

A preliminary thermoreflectance setup has been assembled and tested; an initial result is shown in Figure 5-1. The resolution of this setup has been measured using a "knife-edge" technique: the focal spot is passed over a sharp boundary and the (DC) reflected power is measured with a photodetector. The rate at which the photodetector signal drops off is fit to the cumulative integral of a Gaussian, and the full-width half-maximum (FWHM) of the Gaussian fit is taken to be the diameter of the focal spot. The result of this measurement, shown in Figure 5-2, indicates the focal spot to be between 3 and 4 μm.

In order to use thermoreflectance to measure internal thermoelectric cooling, two InGaAs diode samples were proposed with layer structures as illustrated in Figure 5-3. These samples were grown by Shaomin Wu in collaboration with Prof. John Bowers
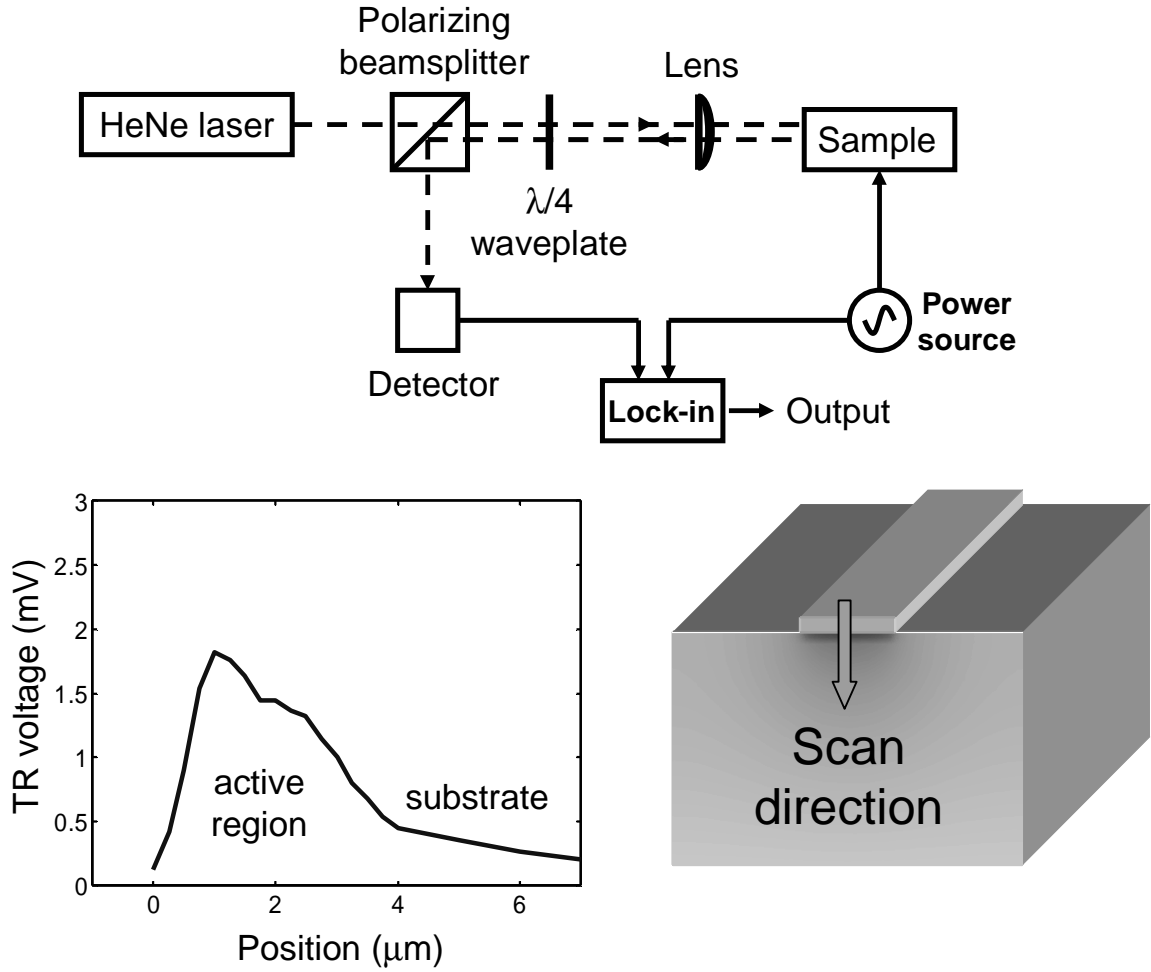
Figure 5-1: Thermoreflectance measurement setup and preliminary measurement on a biased GaSb-based laser.

at the University of California, Santa Barbara. The region lengths were chosen to be 1 μm because this is the approximate recombination length of both electrons and holes in highly-doped InGaAs, the intention being to heat sink the top side in order to remove recombination heat. Transport simulation and finite-element analysis were performed to predict the internal temperature variation of a device with area $100 \times 1000 \mu\text{m}^2$ at a bias current of approximately 100 mA; the results are shown in Figure 5-4. Notice that the temperature is expected to drop by approximately 2 K at the diode junction.

The diodes were processed with a simple lift-off procedure using the contact mask layout shown in Figure 5-5; this pattern is based on optimized contact geometries
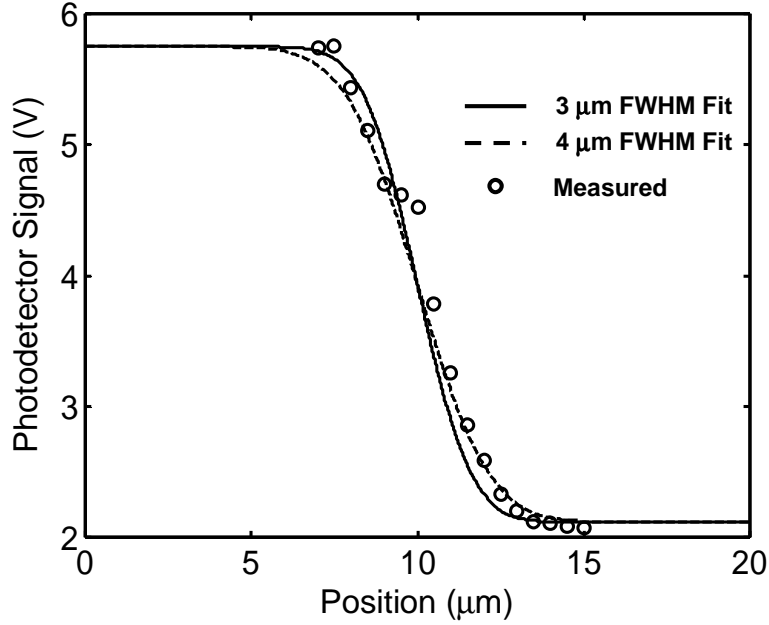
Figure 5-2: "Knife-edge" measurement of the focal spot size.

developed for heterobarrier coolers that balance contact Joule heating with heat conduction away from the surface [21].

Unfortunately, the resolution of the thermoreflectance setup was not able to be lowered below 3-4 μm; this prevented the measurement of the sharp dip in temperature predicted in Figure 5-4. Improvement in the setup optics or decrease in the probe laser wavelength could lead to the resolution enhancement necessary to observe internal thermoelectric cooling. Care must be taken to avoid washing out the internal cooling due to absorption of the HeNe radiation.

Sample #1	Sample #2		
$N_A = 1 \times 10^{20}$	$N_A = 1 \times 10^{20}$	p+ Cap	0.1μm In$_{0.53}$Ga$_{0.47}$As
$N_A = 1 \times 10^{19}$	$N_A = 2 \times 10^{18}$	p	1.0μm In$_{0.53}$Ga$_{0.47}$As
$N_D = 1 \times 10^{19}$	$N_D = 2 \times 10^{18}$	n	1.0μm In$_{0.53}$Ga$_{0.47}$As
$N_D = 3 \times 10^{18}$	$N_D = 3 \times 10^{18}$	Substrate	InP

Figure 5-3: InGaAs diode samples: Layer structure. Doping is given in units of cm^{-3}.
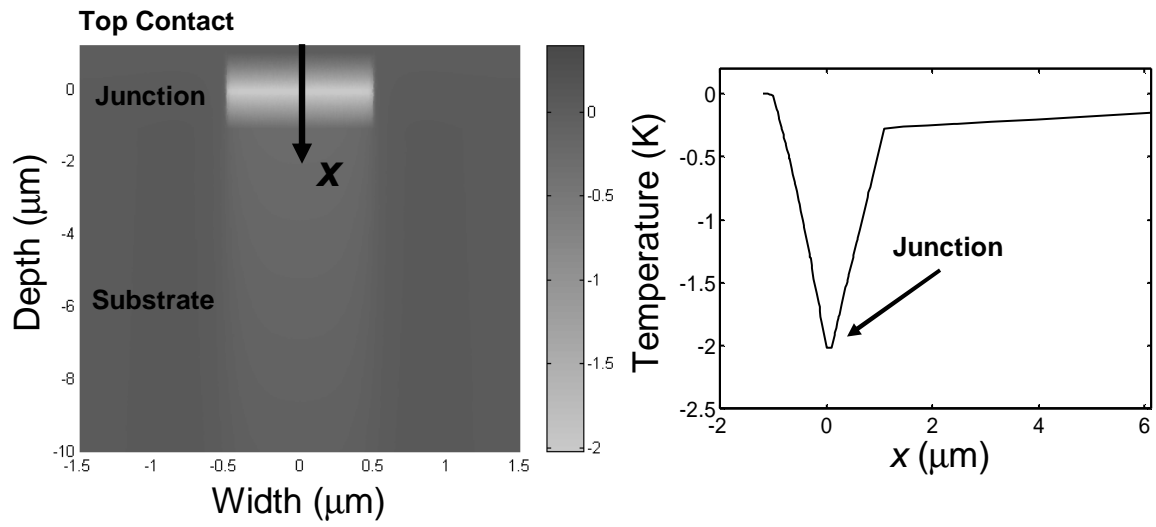
Figure 5-4: InGaAs diode samples: Thermal modeling at a bias of approximately 100 mA.
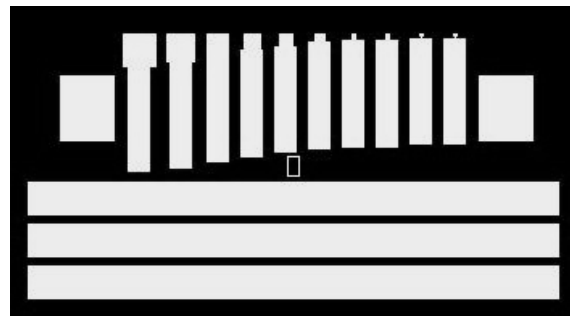
Figure 5-5: InGaAs diode samples: Contact mask
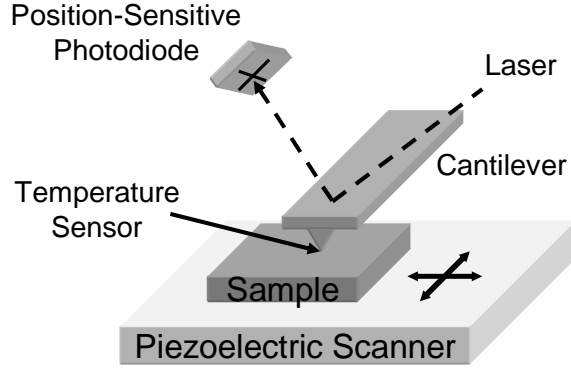
Figure 5-6: Scanning thermal microscopy, a technique based on atomic force microscopy.

5.1.3 Thermoreflectance Measurement of a Heterostructure

A final experiment that remains is to confirm the thermoelectric effects predicted inside heterostructure devices. These effects (as shown in Figures 2-23 and 4-6) form the basis of the improved operation of the ICICLE design.

In order to measure thermoelectric heat exchange at a heterobarrier, two samples were grown exactly as pictured in Figure 4-4 but without any quantum wells due to growth constraints at the time. The growths were performed by Dr. George Turner at MIT Lincoln Laboratory. Unfortunately, the resolution of the thermoreflectance setup limits its use in the study of cooling at the ICICLE cladding/core interfaces.

In order to truly measure thermoelectric cooling at a heterostructure interface, it may be necessary to use a technique such as scanning thermal microscopy (shown in Figure 5-6), which can image on a spatial scale of 10 nm or less [94, 95]. This may also prove useful for studying further mechanisms of internal cooling such as thermionic emission and other nonequilibrium carrier effects [3]. Junction effects such as this one are important for accurately modeling nanoscale transport in such areas as a laser's quantum well. A preliminary result from a Monte Carlo simulation of thermionic emission over a GaAs/AlGaAs heterojunction is shown in Figure 5-7.
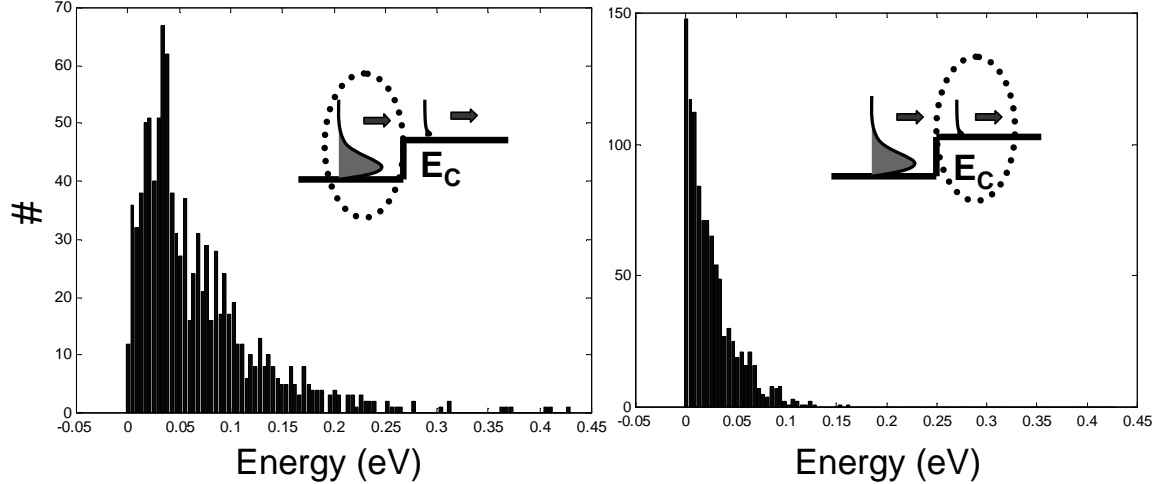
Figure 5-7: Preliminary Monte Carlo simulation of thermionic emission over a GaAs/AlGaAs heterojunction.

5.2 The Future of Internal Cooling

The future of internal thermoelectric cooling is not limited to semiconductor lasers; as shown in Figure 5-8, previous work has shown thermoelectric cooling to be evident in devices such as heterojunction bipolar transistors [6, 67]. In optimizing thermal effects in these devices, it will be important to take into account band offsets and doping densities, as we did for the laser diode.

Better measurement tools will be a key factor in developing internal cooling designs in devices. Scanning thermal microscopy and variants thereof will become increasingly important for the measurement of transport parameters. The thermal characterization of devices may lead to applications such as the mapping of optical signals throughout large photonic integrated circuits using a nondestructive technique such as that proposed in Section 3.2.

As thermoelectric devices become smaller and smaller, it is possible that nanoscale effects will cause future devices to perform at higher efficiencies than previously attainable [16]. Further study of thermoelectric effects in bipolar devices will perhaps enable a class of "active thermoelectric devices" which offer increased nanoscale cooling and faster switching speeds for applications such as thermo-optic switching [96].
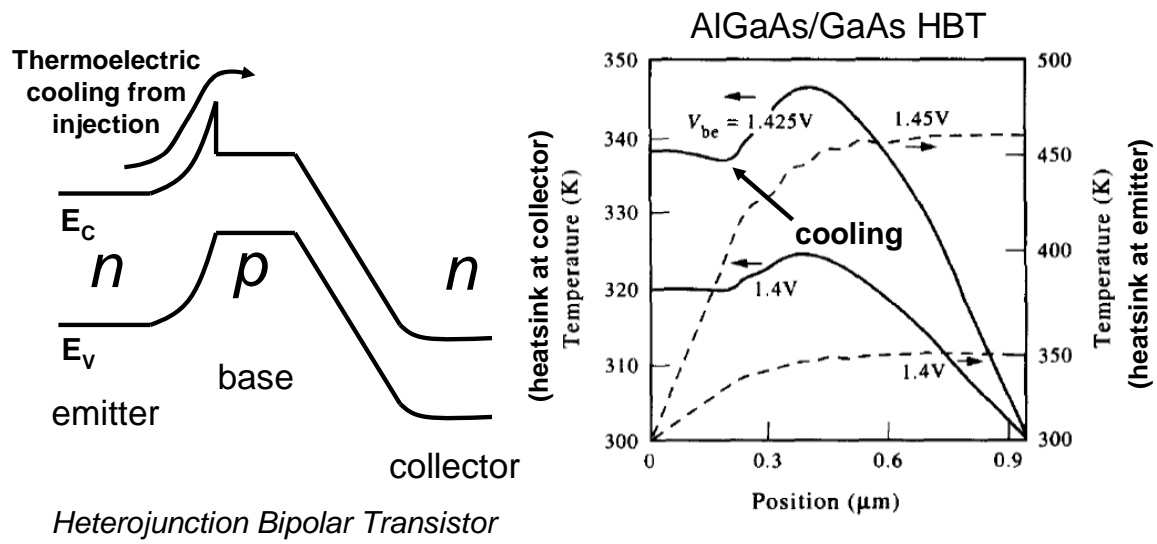
Figure 5-8: Internal thermoelectric cooling in a heterojunction bipolar transistor [6].

Bibliography

[1] E. Bogatin, D. Potter, and L. Peters. *Roadmaps of Packaging Technology*. Integrated Circuit Engineering, Scottsdale, Arizona, 1997.

[2] Z. Zuo, M. North, and K. Wert. "High heat flux heat pipe mechanism for cooling of electronics". *IEEE Trans. Comp. Pack. Tech.*, **24**(2):220, June 2001.

[3] A. Shakouri and J. E. Bowers. "Heterostructure integrated thermionic coolers". *Appl. Phys. Lett.*, **71**(9):1234–6, September 1997.

[4] T. K. Sharma et al. "High-power highly strained InGaAs quantum-well lasers operating at 1.2μm". *IEEE Phot. Tech. Lett.*, **14**(7):887–9, July 2002.

[5] G. W. Turner, H. K. Choi, and M. J. Manfra. "Ultralow-threshold (50 A/cm^2) strained single-quantum-well GaInAsSb/AlGaAsSb lasers emitting at 2.05 μm". *Appl. Phys. Lett.*, **72**:876, 1998.

[6] W. Y. Zhou, Y. B. Liou, and C. Huang. "Steady-state and transient heat responses in AlGaAs/GaAs HBTs". *Solid-State Elect.*, **38**:1118, 1995.

[7] H. J. Yi et al. "Temperature dependence of threshold current density J_{th} and differential efficiency η_d of high-power InGaAsP/GaAs (λ=0.8 μm) lasers". *Appl. Phys. Lett.*, **66**(3):253–55, January 1995.

[8] U. Menzel et al. "Modelling the temperature dependence of threshold current, external differential efficiency and lasing wavelength in QW laser diodes". *Semicond. Sci. Tech.*, **10**(10):1382–92, October 1995.

[9] H. K. Choi and G. W. Turner. "Mid-infrared semiconductor lasers based on antimonide compounds", volume 3 of *Optoelectronic Properties of Semiconductors and Superlattices*. p. 369. Gordon and Breach, Amsterdam, 1997.

[10] P. Tadayon. "Thermal challenges during microprocessor testing". *Intel Tech. J.*, Q3, 2000.

[11] S. Ohr. "Intel technologist cites power as biggest issue". *EE Times*, February 2001.

[12] Thermoelectric cooling module specs. http://www.tellurex.com.

[13] K. Azar. "Cooling technology options". *CoolingZone*, **3**(5), May 2003.

[14] E. Cruse. "An integrated thermal architecture for thermal management of high power electronics". *CoolingZone*, **3**(1), January 2003.

[15] J. A. Skidmore et al. "Silicon monolithic microchannel-cooled laser diode array". *Appl. Phys. Lett.*, **77**(1):10, July 2000.

[16] R. Venkatasubramanian, E. Siivola, T. Colpitts, and B. O'Quinn. "Thin-film thermoelectric devices with high room-temperature figures of merit". *Nature*, **413**:597, October 2001.

[17] X. Fan et al. "High cooling power density SiGe/Si microcoolers". *Elect. Lett.*, **37**(2):126, January 2001.

[18] X. Fan et al. "SiGeC/Si superlattice microcoolers". *Appl. Phys. Lett.*, **78**(11):1580, March 2001.

[19] T. Hackbarth, M. Zeuner, and U. Konig. "The future of SiGe devices beyond HBT applications", volume 8 of *Compound semiconductor*. Franklin, USA, 2002.

[20] C. LaBounty, A. Shakouri, P. Abraham, and J. E. Bowers. "Monolithic integration of thin-film coolers with optoelectronic devices". *Opt. Eng.*, **39**(11):2847, November 2000.

[21] A. Shakouri, C. LaBounty, J. Piprek, P. Abraham, and J. E. Bowers. "Thermionic emission cooling in single barrier heterostructures". *Appl. Phys. Lett.*, **74**(1):88, January 1999.

[22] R. Kaiser and H. Heidrich. "Optoelectronic/photonic integrated circuits on InP between technological feasibility and commercial success". *IEICE Trans. Elect.*, **E85 − C**(4):970, April 2002.

[23] T. Koga et al. "Models for low-dimensional thermoelectricity". *J. Comp.-Aid. Mat. Des.*, **4**(3):175, March 1997.

[24] R. J. Radtke, H. Ehrenreich, and C. H. Grein. "Multilayer thermoelectric refrigeration in $Hg_{1-x}Cd_xTe$ superlattices". *J. Appl. Phys.*, **86**(6):3195, September 1999.

[25] M. Kuzuhara and S. Tanaka. "GaAs-based high-frequency and high-speed devices". *JSAP Int.*, (7):4, January 2003.

[26] C. T. Elliott. "New infrared and other applications of narrow-gap semiconductors". *Proc. SPIE*, **3436**(1-2):763, 1998.

[27] P. R. Berger, N. K. Dutta, K. D. Choquette, G. Hasnain, and N. Chand. "Monolithically Peltier-cooled vertical-cavity surface-emitting lasers". *Appl. Phys. Lett.*, **59**(1):117–9, July 1991.

[28] M. Lundstrom. *Fundamentals of Carrier Transport*. Cambridge University Press, Cambridge, UK, second edition, 2000.

[29] H. J. Goldsmid. *Electronic Refrigeration*. Pion, London, 1986.

[30] D. M. Rowe, editor. *CRC Handbook of Thermoelectrics*. CRC Press, New York, 1995.

[31] W. Nakwaski. "The Peltier coefficient in degenerate and non-degenerate semiconductors". *Electron Technol.*, **14**:81, 1983.

[32] N. W. Ashcroft and N. D. Mermin. *Solid State Physics.* Saunders College Publishing, Philadelphia, 1976.

[33] J. Tauc. *Photo and Thermoelectric Effects in Semiconductors.* Pergamon Press, New York, NY, 1956.

[34] G. D. Mahan and M. Bartkowiak. "Wiedemann-Franz law at boundaries". *Appl. Phys. Lett.*, **74**:953, 1999.

[35] G. C. Dousmanis, C. W. Mueller, H. Nelson, and K. G. Petzinger. "Evidence of refrigerating action by means of photon emission in semiconductor diodes". *Phys. Rev.*, **133**:A316, 1964.

[36] W. Nakwaski. "Optical refrigeration in light-emitting diodes". *Elect. Tech.*, **13**:61, 1982.

[37] S. R. Bowman and C. E. Mungan. "New materials for optical cooling". *Appl. Phys. B*, **71**:807, 2000.

[38] H. Gauck, T. H. Gfroerer, M. J. Renn, E. A. Cornell, and K. A. Bertness. "External radiative quantum efficiency of 96% from a GaAs/GaInP heterostructure". *Appl. Phys. A*, **64**:143, 1997.

[39] L. D. Hicks, T. C. Harman, X. Sun, and M. S. Dresselhaus. "Experimental study of the effect of quantum-well structures on the thermoelectric figure of merit". *Phys. Rev. B*, **53**:R10493, 1996.

[40] A. Shakouri, P. Abraham, and J. E. Bowers. "$III - V$ based heterostructure integrated thermionic coolers". *Appl. Phys. Lett.*, **71**:1234, 1997.

[41] C. Labounty, A. Shakouri, P. Abraham, and J. E. Bowers. "Monolithic integration of thin film coolers with optoelectronic devices". *Opt. Eng.*, **39**:2847, 2000.

[42] Yu. G. Gurevich, O. Yu. Titov, G. N. Logvinov, and O. I. Lyubimov. "Nature of the thermopower in bipolar semiconductors". *Phys. Rev. B*, **51**:6999, 1995.

[43] T. Piotrowski and S. Sikorski. "Photovoltaic effects in an inhomogenous semi-conductor with position-dependent temperature". *Semicond. Sci. Tech.*, **16**:750, 2001.

[44] G. K. Wachutka. "Rigorous thermodynamic treatment of heat generation and conduction in semiconductor device modeling". *IEEE T. Computer-Aided Des.*, **9**:1141, 1990.

[45] L. L. Liou, J. L. Ebel, and C. I. Huang. "Thermal effects on the characteristics of AlGaAs/GaAs heterojunction bipolar transistors using two-dimensional numerical simulation". *IEEE T. Electron Dev.*, **40**:35, 1993.

[46] G. W. Charache et al. "Infrared materials for thermophotovoltaic applications". *J. Elect. Mat.*, **27**:1038, 1998.

[47] O. Yu. Titov et al. "New physical point of view on the peltier effect". In *Proc. of XVI Int. Conf. on Thermoelectrics*, page 661, Dresden, Germany, August 1997.

[48] K. P. Pipe, R. J. Ram, and A. Shakouri. "Minority-carrier thermoelectric devices". In *21st Intl. Conf. on Thermoelectrics*, Long Beach, CA, August 2002.

[49] K. P. Pipe, R. J. Ram, and A. Shakouri. "Bias-dependent Peltier coefficient and internal cooling in bipolar devices". *Phys. Rev. B*, **66**(12):125316, September 2002.

[50] W. Nakwaski. "The Peltier coefficient in degenerate and non-degenerate semi-conductors". *Elect. Tech.*, **14**:81, 1983.

[51] S. M. Sze. *Physics of Semiconductor Devices*. Wiley & Sons, New York, NY, second edition, 1981.

[52] Yu. G. Gurevich and S. I. Shevchenko. "Cooling of electrons in semiconductors by a static electric field". *Sov. Phys. JETP*, **35**:426, 1972.

[53] L. Shi et al. "Nanoscale thermal and thermoelectric mapping of semiconductor devices and interconnects". In *Proc. Int. Conf. Characterization and Metrology for ULSI Tech.*, Austin, TX, March 2003.

[54] H.-K. Lyeo, A. A. Khajetoorians, L. Shi, K. P. Pipe, R. J. Ram, A. Shakouri, and C. K. Shih. "Profiling the thermoelectric power of semiconductor junctions with nanometer resolution." To be published in *Science*.

[55] A. Shakouri et al. "Thermoelectric effects in submicron heterostructure barriers". *Microscale Thermophysical Engineering*, **2**:37, 1998.

[56] D. W. Winston and R. E. Hayes. "Optoelectronic device simulation of Bragg reflectors and their influence on surface-emitting laser characteristics". *IEEE J. Quantum Elect.*, **34**:707, 1998.

[57] J. F. Carlin et al. "High-efficiency top-emitting microcavity LEDs on GaAs and GaAs/Si substrates". *J. Cryst. Growth*, **202**:994, 1999.

[58] H. Z. Fardi, D. W. Winston, R. E. Hayes, and M. C. Hanna. "Numerical modeling of energy balance equations in quantum well $Al_x Ga_{1-x} As$/GaAs *p-i-n* photodiodes". *IEEE Trans. Electron Dev.*, **47**:915, 2000.

[59] J. O. Sofo, G. D. Mahan, and J. Baars. "Transport coefficients and thermoelectric figure of merit of *n*-$Hg_{1-x} Cd_x Te$". *J. Appl. Phys.*, **76**:2249, 1994.

[60] K. P. Pipe, R. J. Ram, and A. Shakouri. "Bias-dependent Peltier coefficient in bipolar devices". In Y. Jaluria, editor, *Proc. ASME Heat Transfer Division,* v.7, pages 219–22, New York, 2001. ASME.

[61] T. Zeng and G. Chen. "Nonequilibrium electron-phonon interaction in thin-film thermionic structures". In *18*[th] *Intl. Conf. on Thermoelectrics*, Baltimore, MD, August 1999.

[62] J. L. Thobel, L. Baudry, A. Cappy, P. Bourel, and R. Fauquembergue. "Electron transport properties of strained $In_x Ga_{1-x} As$". *Appl. Phys. Lett.*, **56**:346, 1990.

[63] Chin-Yi Tsai, Chin-Yao Tsai, Y.-H. Lo, and L. F. Eastman. "Carrier energy relaxation time in quantum-well lasers". *IEEE J. Quant. Elect.*, **31**:2148, 1995.

[64] S. T. Huxtable et al. "Thermal conductivity of indium phosphide based super-lattices". *Microscale Thermophysical Eng.*, **4**:197, 2000.

[65] R. Rodrigues, S. A. Juen, K. F. Lamprecht, and R. A. Höpfel. "Electron-hole scattering in highly doped *p*-GaAs after femtosecond optical excitation". *Semicond. Sci. Technol.*, **9**:456, 1994.

[66] Chin-Yi Tsai et al. "Effects of electron-hole energy transfer on the nonlinear gain coefficients in the small-signal modulation response of semiconductor lasers". *Appl. Phys. Lett.*, **71**:1747, 1997.

[67] E. Pop, S. Sinha, and K. E. Goodson. "Monte Carlo modeling of heat generation in electronic nanostructures". In *Proc. Intl. Mech. Eng. Congress & Expo.*, New Orleans, LA, November 2002. ASME.

[68] G. L. Tan, N. Bewtra, K. Lee, and J. M. Xu. "A two-dimensional non-isothermal finite element simulation of laser diodes". *IEEE J. Quantum Electron.*, **29**:822–35, March 1993.

[69] L. A. Coldren and S. W. Corzine. *Diode Lasers and Photonic Integrated Circuits*. Wiley & Sons, New York, 1995.

[70] H. J. Lee, J. S. Yoon, and C.-J. Kim. "Numerical analysis on the cooling of a laser diode package with a thermoelectric cooler". *Heat Transf., Asian Res.*, **30**:357, 2001.

[71] A. F. Mills. *Heat and Mass Transfer*. Irwin, Boston, 1995.

[72] W. B. Joyce and R. W. Dixon. "Thermal resistance of heterostructure lasers". *J. Appl. Phys.*, **46**:855, 1975.

[73] K. P. Pipe and R. J. Ram. "Experimental determination of heat flow in semiconductor lasers". In *Proc. Conf. on Lasers and Electro-Optics*, Long Beach, CA, May 2002.

[74] S. G. Patterson, E. K. Lau, K. P. Pipe, G. S. Petrich, R. J. Ram, and L. A. Kolodziejski. "Temperature properties of bipolar cascade lasers". In *Proc. Conf. on Lasers and Electro-Optics*, San Francisco, CA, May 2000.

[75] S. G. Patterson, E. K. Lau, K. P. Pipe, and R. J. Ram. "Temperature characteristics of bipolar cascade lasers". *Appl. Phys. Lett.*, **77**:172, 2000.

[76] J. S. Manning. "Thermal impedance of diode lasers: Comparison of experimental methods and a theoretical model". *J. Appl. Phys.*, **52**:3179, 1981.

[77] W. Both and J. Piprek. "Thermal resistance of InGaAs/InP laser diodes". *J. Thermal Anal.*, **36**:1441, 1990.

[78] N. Chong, T. A. S. Srinivas, and H. Ahmed. "Performance of GaAs microbridge thermocouple infrared detectors". *J. Microelectromechanical Sys.*, **6**:136, 1997.

[79] K. P. Pipe and R. J. Ram. "Comprehensive heat exchange model for a semiconductor laser diode". *IEEE Phot. Tech. Lett.*, **15**, April 2003.

[80] Patent pending.

[81] S. Dilhaire et al. "Laser diode light efficiency determination by thermoreflectance microscopy". *Microelectronics J.*, **32**:899, 2001.

[82] J. A. Hudgings, K. P. Pipe, and R. J. Ram. "Wafer scale profiling of photonic integrated circuits". In *Proc. Conf. on Lasers and Electro-Optics*, Baltimore, MD, June 2003.

[83] J. A. Hudgings, K. P. Pipe, and R. J. Ram. "Thermal profiling for optical characterization of waveguide devices". *Appl. Phys. Lett.*, **83**:3882, 2003.

[84] J. M. Borrego et al. "Photon recycling and recombination processes in 0.53 eV *p*-type InGaAsSb". *J. Appl. Phys.*, **89**:3753, 2001.

[85] K. P. Pipe, R. J. Ram, A. K. Goyal, and G. W. Turner. "Electrical and thermal analysis of heat flow in $\lambda = 2.05\mu$m GaInAsSb/AlGaAsSb lasers". In *Proc. Conf. on Lasers and Electro-Optics*, Baltimore, MD, June 2003.

[86] B. Tadayon, C. S. Kyono, M. Fatemi, S. Tadayon, and J. A. Mittereder. "Extremely low specific contact resistivities for p-type GaSb, grown by molecular beam epitaxy". *J. Vac. Sci. Technol. B*, **13**:1, 1995.

[87] R. P. Sarzala and W. Nakwaski. "Finite-element thermal model for buried-heterostructure diode lasers". *Opt. Quant. Electron.*, **26**:87, 1994.

[88] I. Umebu. "A proposal of a method for analysing the leakage characteristics of 1.3μm semiconductor buried heterostructure lasers". *Semicond. Sci. Technol.*, **8**:63, 1993.

[89] R. F. Kazarinov and M. R. Pinto. "Carrier transport in laser heterostructures". *IEEE J. Quantum Electron.*, **30**:49, 1994.

[90] G. A. Baraff. "Semiclassical description of electron transport in semiconductor quantum-well devices". *Phys. Rev. B*, **55**:10745, 1997.

[91] K. P. Pipe, R. J. Ram, and A. Shakouri. "Internal cooling in a semiconductor laser diode". *IEEE Phot. Tech. Lett.*, **14**(4):453–5, April 2002.

[92] K. P. Pipe, R. J. Ram, and A. Shakouri. "The physics of heat transport in semiconductor lasers". In *IEEE Intl. Semiconductor Laser Conf*, Garmisch, Germany, September 2002.

[93] I. Vurgaftman, J. R. Meyer, F. H. Julien, and L. R. Ram-Mohan. "Design and simulation of low-threshold antimonide intersubband lasers". *Appl. Phys. Lett.*, **73**:711, 1998.

[94] K. Luo, R. W. H. Herrick, A. Majumdar, and P. Petroff. "Internal temperature distribution of a vertical-cavity surface-emitting laser measured by scanning

thermal microscopy". In *Proc. Intl. Mech. Eng. Congress & Expo.*, Atlanta, GA, November 1996. ASME.

[95] D. G. Cahill et al. "Nanoscale thermal transport". *J. Appl. Phys.*, **93**:793, 2003.

[96] K. P. Pipe, R. J. Ram, and A. Shakouri. "Thermoelectric effects in bipolar devices: internally cooled semiconductor lasers". In *U.S.-Japan Nanotherm Seminar: Nanoscale Thermal Science and Engineering*, Berkeley, CA, June 2002.